

# Naval Research Laboratory

Washington, DC 20375-5320

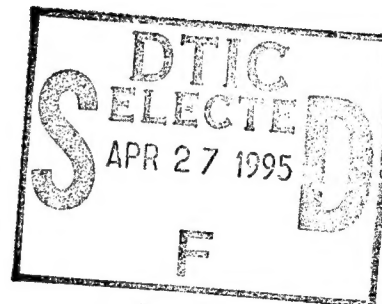


NRL/MR/7220--95-7652

## Millimeter Wave Radiometer Utility Study

PETER W. GAISER  
JAMES P. HOLLINGER  
STEVEN R. HIGHLEY  
GLENN D. SANDLIN

*Remote Sensing Physics Branch  
Remote Sensing Division*



March 27, 1995

\*Original contains color  
plates: All DTIC reproductions  
will be in black and  
white\*

19950426 109

Approved for public release; distribution unlimited.

DTIC LIBRARY CONTROLLED

## REPORT DOCUMENTATION PAGE

Form Approved  
OMB No. 0704-0188

Public reporting burden for this collection of information is estimated to average 1 hour per response, including the time for reviewing instructions, searching existing data sources, gathering and maintaining the data needed, and completing and reviewing the collection of information. Send comments regarding this burden estimate or any other aspect of this collection of information, including suggestions for reducing this burden, to Washington Headquarters Services, Directorate for Information Operations and Reports, 1215 Jefferson Davis Highway, Suite 1204, Arlington, VA 22202-4302, and to the Office of Management and Budget, Paperwork Reduction Project (0704-0188), Washington, DC 20503.

1. AGENCY USE ONLY (Leave Blank)	2. REPORT DATE	3. REPORT TYPE AND DATES COVERED	
	March 27, 1995	Final Report 5/93-10/94	
4. TITLE AND SUBTITLE  Millimeter Wave Radiometer Utility Study			5. FUNDING NUMBERS  PE -63011F PR -RDTE WU -562004
6. AUTHOR(S)  Peter W. Gaiser, James P. Hollinger, Steven R. Highley and Glenn D. Sandlin			
7. PERFORMING ORGANIZATION NAME(S) AND ADDRESS(ES)  Naval Research Laboratory Washington, DC 20375-5320			8. PERFORMING ORGANIZATION REPORT NUMBER  NRL/MR/7220-95-7652
9. SPONSORING/MONITORING AGENCY NAME(S) AND ADDRESS(ES)  SAFSP P.O. Box 46335 Washington, D.C. 20050-6395			10. SPONSORING/MONITORING AGENCY REPORT NUMBER
11. SUPPLEMENTARY NOTES  c			
12a. DISTRIBUTION/AVAILABILITY STATEMENT  Approved for public release; distribution unlimited.			12b. DISTRIBUTION CODE
13. ABSTRACT (Maximum 200 words)  Many military and environmental applications require wide area surveillance on a timely and global basis. Passive microwave and millimeter wave imaging has the advantage over visual and infrared systems of being a near all-weather surveillance system with the ability to see through clouds and most adverse weather conditions with equal day and night sensitivity. The major disadvantage of microwave and millimeter wave radiometric systems is that the relatively long wavelengths require aperture several orders of magnitude larger than at infrared to obtain comparable spatial resolution. However, even "low" resolution microwave and millimeter wave radiometers can contribute significantly to intelligence gathering and environmental remote sensing. This document presents a study of the capabilities of microwave and millimeter wave imaging from space with systems which provide resolutions of 100-400 m at observation frequencies of 1.4-140 GHz. Possible radiometer architectures and their space development are examined the surveillance and environmental remote sensing benefits of multifrequency high resolution microwave and millimeter wave radiometry are discussed in depth.			
14. SUBJECT TERMS  Radiometry Microwave Millimeter waves			15. NUMBER OF PAGES  110
			16. PRICE CODE
17. SECURITY CLASSIFICATION OF REPORT  UNCLASSIFIED	18. SECURITY CLASSIFICATION OF THIS PAGE  UNCLASSIFIED	19. SECURITY CLASSIFICATION OF ABSTRACT  UNCLASSIFIED	20. LIMITATION OF ABSTRACT  UL

## CONTENTS

<b>1.0</b>	<b>INTRODUCTION</b>	1-1
<b>2.0</b>	<b>MILLIMETER WAVE RADIOMETRY</b>	2-1
2.1	<u>Brightness Temperature</u>	2-1
2.2	<u>Antenna Temperature</u>	2-1
2.3	<u>Receiver Noise Temperature</u>	2-2
2.4	<u>Minimum Detectable Signal</u>	2-2
2.5	<u>Target Contrast</u>	2-3
<b>3.0</b>	<b>INSTRUMENT TRADEOFFS</b>	3-1
<b>4.0</b>	<b>REMOTE SENSING OF THE ENVIRONMENT</b>	4-1
4.1	<u>Terrain</u>	4-1
4.1.1	Soil Moisture	4-1
4.1.2	Surface and Soil Classification	4-3
4.1.3	Wetlands	4-4
4.1.4	Vegetation	4-4
4.1.5	Snow Cover	4-5
4.2	<u>Oceans</u>	4-7
4.2.1	Sea Surface Salinity and Temperature	4-7
4.2.2	Sea Surface Winds	4-8
4.3	<u>Sea Ice</u>	4-8
4.3.1	Ice Type	4-8
4.3.2	Ice Zone Imagery	4-10
4.4	<u>Atmosphere</u>	4-10
4.4.1	Water Vapor, Clouds, and Rain	4-10
4.4.2	Aerosols and Particulates	4-16
4.5	<u>Operation Desert Storm</u>	4-17
<b>5.0</b>	<b>TARGET/BACKGROUND CHARACTERISTICS</b>	5-1
5.1	<u>Millimeter Wave Image Characteristics</u>	5-1
5.2	<u>Clutter</u>	5-1
5.2.1	Surface Clutter	5-1
5.2.2	Atmospheric Temporal Variations	5-2
5.3	<u>Military Targets</u>	5-3
5.3.1	Aircraft, Tanks and Vehicles	5-3
5.3.2	Ships and Ship Wakes	5-5
5.3.3	Infrastructure	5-5
5.3.4	Battlefield Damage Assessment	5-6
<b>6.0</b>	<b>SUMMARY</b>	6-1
<b>7.0</b>	<b>REFERENCES</b>	7-1

# MILLIMETER WAVE RADIOMETRIC UTILITY STUDY

## 1.0 INTRODUCTION

Wide area surveillance on a timely and global basis is critical for many military and environmental applications. Passive millimeter wave imaging has the advantage over visual and infrared systems of being a near all-weather surveillance system with the ability to see through clouds and most adverse weather conditions with equal day-time and night-time sensitivity. The major drawback of millimeter wave radiometric systems is that the relatively long wavelengths require very large apertures, several orders of magnitude larger than at infrared, to obtain similar high resolution. However even "low" resolution millimeter-wave systems may contribute significantly to intelligence gathering.

This document presents a study of the utility of passive millimeter-wave imaging from space with systems which provide surface resolutions of 100 to 400 m with observational frequencies ranging from 1.4 to 140 GHz and represents an extension of the previous millimeter wave study published in February, 1992. The environmental benefits of multifrequency high resolution millimeter wave radiometry are discussed in depth.

Accession For	
NTIS	CRA&I <input checked="" type="checkbox"/>
DTIC	TAB <input type="checkbox"/>
Unannounced <input type="checkbox"/>	
Justification	
By _____	
Distribution / _____	
Availability Codes	
Dist	Avail and / or Special
A-1	

---

Manuscript approved December 14, 1994.

## 2.0 MILLIMETER WAVE RADIOMETRY

### 2.1 Brightness Temperature

The power received by an Earth viewing radiometer consists of man-made radiations from point sources and the self or blackbody type radiation from targets and the background environment. The millimeter wave signal is composed of not only the radiation emitted by targets and the Earth's surface but also the downwelling radiation emitted by the atmosphere and then reflected by the surface as well as the upward emission and attenuation of the atmosphere between the surface and the radiometer. The intensity of radiation, in watts/m<sup>2</sup>/Hz/steradian, from a blackbody at a physical temperature T is given by Planck's Law as

$$I = (hv/\lambda^2) / (\exp(hv/KT) - 1) \quad (2.1)$$

where h and K are Planck's and Boltzmann's constants respectively, v the frequency, and  $\lambda$  the wavelength. At millimeter wave frequencies where  $KT \gg hv$  the Rayleigh-Jeans approximation to the Planck blackbody radiation law applies and

$$I \approx KT/\lambda^2 \quad (2.2)$$

Therefore the power radiated by a perfectly radiating surface per unit bandwidth is proportional to the physical temperature, T, of the material. If the surface is not a perfect radiator but has an emissivity, e, less than one, the power radiated is proportional to eT. Even if the source is man made, and radiates by some non-thermal process, the power it radiates may be specified by a temperature; that temperature being the physical temperature a blackbody radiator must have to radiate the same power as the non-thermal source over the same bandwidth. Thus the power radiated from any target and the environmental background may be specified by a brightness temperature. This equivalent brightness temperature,  $T_B$ , can easily be millions of degrees for non-thermal sources.

### 2.2 Antenna Temperature

It is convenient to also specify the power received by the antenna and delivered to the receiver input by a temperature. This is possible because of Nyquist's theorem which states that the power available at the terminals of a resistor per unit bandwidth is proportional to the physical temperature of the resistor. Thus an antenna temperature,  $T_A$ , may be defined which is the temperature of an impedance, identical to the antenna impedance, which when connected in place of the antenna delivers the same power to the receiver as does the antenna. A millimeter wave radiometer measures the absolute level of the total power received by its antenna at a particular polarization over its reception bandwidth. In general, high gain antennas receive power primarily over a relatively narrow beam or solid angle; however some power is usually received from all directions. The power received in these side-lobes and back-lobes, though small, is

normally not desired and a correction is applied to remove it. The antenna temperature is the average of the brightness temperature over all directions, weighted by the antenna gain,  $G$ .

$$T_A(r, t) = \int T_B(r, t) G(r-r') d\Omega / 4\pi \quad (2.3)$$

This power is then amplified by the receiver and appears at the receiver output terminals.

### 2.3 Receiver Noise Temperature

In any realizable receiver, random noise is generated by the receiver in the amplification of the desired signal and unavoidably appears with it at the output terminals. This situation may be equally well represented by the addition of an unwanted noise power to the input signal at the input terminals of an ideal noiseless receiver which is then amplified along with the desired signal. This noise power may also be specified by a temperature,  $T_N$ . This is the temperature to which the input impedance of the receiver must be raised in order that, when amplified by the ideal noiseless receiver, the noise power, per unit bandwidth, at the output terminals is identical to the noise generated by the real receiver. The receiver noise power,  $T_N$ , is essentially "white" noise with a flat power spectrum extending far beyond the spectrum of  $T_A$ . It is therefore necessary to filter or remove the receiver noise contribution at equivalent spatial frequencies where there is no signal from the antenna. The signal measured at the output of the receiver is

$$T_M(t) = \int [T_A(r, t') + T_N(t')] H(t-t') dt' \quad (2.4)$$

where  $H$  is the impulse response of the receiver low-pass filter. The dwell or integration time  $\tau$  on the scene is determined by the cutoff frequency of the low-pass filter  $\Delta f_c$ . For an ideal low-pass filter  $\tau = 1/(2\Delta f_c)$ .

### 2.4 Minimum Detectable Signal

The minimum detectable signal,  $\Delta T_N$ , is given by

$$\Delta T_N = K_{sys} T_{sys} [\Delta f \tau]^{-1/2} \quad (2.5)$$

where  $T_{sys}$  includes both the receiver noise,  $T_N$ , and the signal from the antenna,  $T_A$ ,  $K_{sys}$  is a sensitivity constant of order unity and depends on the type of receiver and  $\Delta f$  is the pre-detection bandwidth of the receiver.

Therefore it is possible to describe the signal from the target and background in terms of a brightness temperature, the signal received by the antenna as an antenna temperature, and the quality of the receiver as a noise temperature. Note that  $T_B$  is an inherent property of the scene being viewed while both  $T_A$  and  $T_N$  may be selected to some degree by the design of the antenna and receiver.

## 2.5 Target Contrast

The effective antenna beam solid angle  $\Omega_e$  is defined as the solid angle through which all the power from a transmitting antenna would flow if the power were constant over this angle and equal to the peak value and is given by

$$\Omega_e = \int_{4\pi} [G(r)/G_o] d\Omega = 4\pi/G_o \quad (2.6)$$

where  $G(r)$  is the antenna gain in direction  $r$  and  $G_o$  is the peak gain. The main beam solid angle,  $\Omega_B$ , is defined similarly but with the restriction that the power is now just that from the main lobe up to the first nulls; not the entire power pattern. The ratio  $\Omega_B/\Omega_e$  is the main beam efficiency and is typically  $> 0.9$  for filled apertures. The solid angle subtended by a target,  $\Omega_t$ , is determined by limiting the integral of Equation (2.6) to those directions from which power is received from the target.

The target contrast,  $\Delta T_A$ , is defined as the difference between the antenna temperature when a target is present in the antenna beam and when it is not. Following Equation (2.3) the target contrast is given by

$$\Delta T_A = T_{At} - T_{Ab} = \int_{4\pi} T_{Bt} G d\Omega / 4\pi - \int_{4\pi} T_{Bb} G d\Omega / 4\pi \quad (2.7)$$

where  $T_{Bt}$  and  $T_{Bb}$  are the scene brightness temperatures when the target is present and when it is not respectively. Equation (2.7) may be rewritten using the definitions of Equation (2.6) as

$$\Delta T_A = [\Omega_t/\Omega_e] \int_t (T_{Bt} - T_{Bb}) G d\Omega / \int_t G d\Omega. \quad (2.8)$$

Thus the target contrast is the normalized integral, over the solid angle subtended by the target, of the brightness temperature difference between the target and background weighted by the antenna gain and reduced by the ratio of the target solid angle to the effective beam solid angle. Note that  $\Omega_t/\Omega_e$  is approximately equal to  $A_t/2A_{BW}$ . Where  $A_t$  is the area of the target and  $A_{BW}$

is the area of the half-power beam-width on the Earth's surface. Therefore for targets smaller than the half-power beam-width

$$\Delta T_A \approx [A_t/2A_{BW}] [T_{Bt} - T_{Bb}] . \quad (2.9)$$

For targets large compared to the half-power beam-width,  $\Omega_t$  is approximately equal to  $\Omega_e$  and  $\Delta T_A = [T_{Bt} - T_{Bb}]$ .

As described above the millimeter wave radiometric signal is composed of not only the radiation emitted by the target and background but also the downwelling radiation emitted by the atmosphere reflected by the surface as well as the upward emission and attenuation of the atmosphere between the surface and the radiometer. The brightness temperature contributing to  $\Delta T_A$  as seen by a radiometer looking at the Earth from space may be written as

$$T_{Bb} = e_b T_o (1-\alpha) + (1-e_b) \alpha T_o (1-\alpha) + \alpha T_o . \quad (2.10)$$

Here  $\alpha$  is the fractional atmospheric loss and  $e_b$  is the emissivity of the background;  $(1-e_b)$  is then the reflectivity of the background. The physical temperatures of the atmosphere and background are assumed to be equal and given by  $T_o$ . In this case the atmospheric radiation is specified by  $\alpha T_o$ . The first term in Equation (2.10) represents the radiation emitted by the earth,  $e_b T_o$ , attenuated by the atmosphere,  $(1-\alpha)$ . The second term arises from the downwelling atmospheric radiation,  $\alpha T_o$ , reflected from the Earth's surface,  $(1-e_b)$ , and attenuated by the atmosphere,  $(1-\alpha)$ . The last term represents the upwelling atmospheric radiation. Equation (2.10) may be rewritten as

$$T_{Bb} = e_b T_o (1-\alpha)^2 + \alpha T_o (2-\alpha) . \quad (2.11)$$

Similarly the radiation received from the target is given by

$$T_{Bt} = e_t \delta T (1-\alpha) + e_t T_o (1-\alpha)^2 + \alpha T_o (2-\alpha) \quad (2.12)$$

where  $\delta T$  is the difference in the physical temperature, if any, between the target and the background and  $e_t$  is the emissivity of the target. The contrast is then from Equations (2.9), (2.11), and (2.12)

$$\Delta T_A = \left( \frac{A_t}{2A_{BW}} \right) [e_t \delta T (1-\alpha) + (e_t - e_b) T_o (1-\alpha)^2]. \quad (2.13)$$

Note that:

The larger the target, the greater the signal, until the antenna beam is filled.

The greater the difference in emissivities, the greater the signal.

The larger the atmospheric losses, the smaller the signal.

With the right combination of  $\delta T$ ,  $e_t - e_b$ , and  $\alpha$ , the target can disappear.

Signals can be positive or negative.

The signal-to-noise, S/N, of the target is given by the ratio of Equations (2.13) and (2.5)

$$S/N = \frac{\left( \frac{A_t}{2A_{BW}} \right) [e_t \delta T (1-\alpha) + (e_t - e_b) T_o (1-\alpha)^2]}{[K_{sys} T_{sys} (\Delta f \tau)^{-1/2}]} \quad (2.14)$$

The target is defined by  $A_t$ ,  $e_t$ , and  $\delta T$ ; its area, emissivity, and physical temperature difference from the background. The weather is specified by the atmospheric loss,  $\alpha$ , and the background by its emissivity,  $e_b$ . The radiometric system is defined by  $K_{sys}$ ,  $T_{sys}$ ,  $\Delta f$ , and  $A_{BW}$ . The orbit is specified by the dwell time  $\tau$  and  $A_{BW}$ . It should be noted that while the physical temperature difference between the target and background,  $\delta T$ , is the primary contributor to scene contrast at infrared it is generally negligible compared to the emissivity difference between the target and background,  $(e_t - e_b)$ , at millimeter wave frequencies. In most cases the term  $e_t \delta T (1-\alpha)$  may be set to zero in Equation (2.14). With clear skies and low humidity,  $\alpha$  is near 0. With rain or heavy clouds  $\alpha$  will increase to near 1. The emissivity,  $e_t$ , will vary from near 0 for a metal surface to 1 for absorbing material. The emissivity,  $e_b$ , for the sea surface is about 0.6 at 90 GHz and varies between about 0.7 and 0.9 for land depending largely on the moisture content of the soil. Background and target characteristics are discussed in detail in Sections 4 and 5.

### 3.0 INSTRUMENT TRADEOFFS

This section presents a brief discussion of the major hardware issues associated with achieving high spatial resolution microwave radiometry from space. In particular, the feasibility of obtaining a 200 meter footprint at frequencies of 1.4, 6, 10, 19, 22, 37, 90, and 140 GHz is presented along with comparisons of what resolutions result with 4, 10, and 17 meter reflectors. In addition candidate satellite orbits, revisit times, and resolution tradeoffs are discussed.

The spatial resolution of satellite imagery is one of the major driving factors in the instrument design. The size of the resolution element on the ground is commonly defined by the 1/2 power points (beamwidth) of the antenna radiation gain function. The beamwidth, BW, in radians, may be approximated by  $BW = a * \lambda/D$ , where  $\lambda$  is the wavelength, D is the aperture diameter, and  $a$  is a constant depending on aperture current distribution and physical make up of the antenna. For a circular aperture,  $a$  can vary from 1 for a uniform distribution, to 1.5 for steeply tapered distribution. Selection of the taper governs the aperture efficiency, beam efficiency, and the level of the side lobes. High beam efficiency and low side lobe levels are important in radiometry. Selecting a steep taper such as Gaussian or  $\cos^2$  can reduce side lobes to less than -30 dB but with a loss of aperture efficiency which requires the aperture to be 25% larger to obtain the same spatial resolution. Table 3.1 gives the spatial resolution for the frequencies of interest with different reflector diameters and tapers associated with a nadir viewing instrument orbiting at a 400 km altitude. The level of the first side lobe is also given for each taper. Apertures of 4, 10, and 17 meters are considered here since they represent present state of the art, near term availability, and longer term development. The apertures are presented with aperture tapers of:

- a.  $\cos^2$  tapered to 0 at the edges,
- b.  $\cos$  tapered to 0 at the edge,
- c.  $1-r^2$  tapered to 1/3 peak at the edge, and
- d. uniform distribution.

The notations in Table 3.1 identifies, for example, entry 4a as a 4 meter aperture with a  $\cos^2$  taper.

Another important factor to be considered in the design of an imaging system is distortion. Using a simplified two-dimensional optical model with the simple reflector configuration in Figure 3.1, the transverse spherical aberration, TAS, blurs the image due to a change in focal point as rays move away from the center of the reflector. Spherical aberration is symmetrical about the z axis and independent of angle. Off-axis aberrations of coma, astigmatism, and distortion increase blurring as the incidence angle increases. Figure 3.2 depicts the angular aberrations which are defined by Equation (3.1) [Schroeder, 1987].

$$AA = 3a_1 \frac{y^2\theta}{R^2} + 2a_2 \frac{y\theta^2}{R} + a_3 \theta^3 . \quad (3.1)$$

A more complex optics equation is used in the detailed antenna design and performance analyses (e.g., the addition of the third dimension and diffraction analysis) but Equation (3.1) will serve as a starting point. For large ratios of antenna diameter to wavelength, optics provides a good approximation. The first term in Equation (3.1) is coma, the second astigmatism, and the last offset. Coma causes a comet shaped blur with the tail pointing towards the axis. Astigmatism is a constant blur. Offset does not affect image quality but changes its position. The summed effect of these aberrations causes the distortion to increase as you move away from the axis. In applications where constant image resolution is important, aberrations must be kept small or constant over the field of view by defocusing the center beams. Using a large radius of curvature,  $R$ , reduces the distortion. This is equivalent to a larger  $F$  number, which is the ratio of focal length to aperture diameter,  $f/D$ . Aberrations can also be reduced by using multiple mirrors as in the Cassegrain telescope. Properly designed, a Cassegrain system will have no spherical aberration, and coma can be reduced to near zero. Figures 3.3a - 3.3f compare the aberrations of a single parabolic reflector system and an aplanatic Cassegrain system verses  $F$  number. Several observations may be made from these figures with respect to image quality [Cogdell and Davis, 1973; Hannan, 1961; Love, 1978]:

- (1) In all cases a two-reflector system is desirable over a single reflector system.
- (2) Coma is not dependent on  $F$ .
- (3) Near the center, coma is the major distortion.
- (4) Astigmatism increases as the frequency decreases and as the aperture decreases.
- (5) Higher  $F$  numbers have lower astigmatism.
- (6) High  $F$  numbers are less important at high frequencies where coma dominates.

The discussion presented above has been for real aperture systems with focal plane arrays. An alternate system uses a synthetic aperture array. Distortion mechanisms are different in a synthesized array. The synthesized array consist of several antenna elements. The outputs of these antennas are multiplied in pairs to form a complex spatial frequency domain set of data. This data is transformed to generate a spatial image. Beam characteristics such as side lobes and beamwidth are dependent on the inversion algorithm as well as the physical make up of the array. Side lobe levels are typically greater than those of a real aperture and beams widen as they move from the center lobes [LeVine, 1990].

Synthetic beams have an advantage over real beams in the crossover points for the beams. Real beams will be separated by nearly a beamwidth, crossing near the first null. Synthesized beams can be adjusted to cross near the 3 dB point, which can be important in imaging applications.

A third parameter important in microwave radiometry is the minimum thermal resolution the instrument can distinguish. For a total power real beam configuration, the rms noise level is defined as [Kraus, 1966]

$$\Delta T = \frac{T_{REC} + T_A}{\sqrt{B\tau}} , \quad (3.2)$$

where  $T_{REC}$  is the receiver noise temperature,  $T_A$  is the scene temperature,  $B$  is the predetection bandwidth, and  $\tau$  is the postdetection integration time. The synthetic aperture noise level is

$$\Delta T = \frac{T_{REC} + T_A}{\sqrt{2B\tau}} \cdot \frac{1}{\sqrt{NM}} \cdot \frac{A_{syn}}{A_e} , \quad (3.3)$$

where  $NM$  is the number of independent pairs of elements,  $A_e$  is the area of an element, and  $A_{syn}$  is the area of the total array.

Table 3.2 presents the noise figures for a real beam system. Table 3.3 is the noise figures for ESTAR (Electronically Steered Thinned Array Radiometer) type synthetic arrays. Bandwidths are 10% for both types of arrays. Integration times are taken to be the time to move 1/2 a beamwidth, and, hence vary with frequency, altitude, and aperture size. Receiver noise figures are improving rapidly. MIMICS technology is available at higher frequencies such as W band. As  $T_{REC}$  approaches  $T_A$ , a point is reached where the improvement in system noise level by lowering receiver noise figures is of little value.

A real aperture spaced based imaging system can be made as a scanning system, a push broom, or a large array. A scanner mechanically moves one or a few beams across the field of view and has low radiometer sensitivity due to the short time spent on each pixel. A push broom scanner relies on a linear array to generate the desired swath. The sensitivity is increased by the multiple receivers and no mechanical movement is required. The large array uses receivers to acquire data in two dimensions without relying on platform movement. This requires a method to point and track the array but will give the highest sensitivity. Expense and complexity increases as the number of receivers increase.

The swath width is directly proportional to the beamwidth, the number of beams, and the altitude. In a real aperture system it is extremely difficult to place the elements such that their beam patterns intersect at the 3 dB points. In general beams will be separated by 1.8 to 2 beam widths, leaving a hole between pixels. By placing a second row of receivers offset from the first by 1/2 the beam to beam spacing, a full sample of the scene can be acquired but with a slight time delay. To obtain a Nyquist sampled scene, 4 rows would be needed to properly sample the scene, as shown in Figure 3.4. By placing multiple sets of receivers,  $4 \times n$  rows, the scene would get multiple samples in each pass. This could be used to reduce noise or used in a differencing process to detect moving targets. Table 3.4 presents the swath width and search rate for various systems in a 400 km circular orbit. The number of beams required is determined by the off axis distortion. With two offset rows the number of pixels would be twice this number

overlapping near the -2 dB point. Coma, not being dependent on frequency or  $F$ , dominates the distortion at the higher frequencies and fixes the array width at 50 pixels.

Figures 3.5, 3.6, and 3.7 are typical designs of a spaced based microwave imaging system. The basic system has an aperture with an  $F$  number of 5 for low off axis distortion and an  $N$  by 4 array of elements ( $N$  being the width of the array out to the point where aberrations are equal to 1.5 beamwidth). Figure 3.5 is an offset parabolic system with approximate dimensions for a 10 meter reflector and a 4 meter reflector. The distance from the reflector to the receivers makes it impractical for large reflectors. By folding the optical path as in a cassegrain telescope we get an offset with a large  $F$  number but with all the large parts near the spacecraft body, as shown in the three designs of Figure 3.6, which shows the rough sizes for a 4, 10, and 17 meter aperture. Only the smaller secondary reflector needs to be extended.

Figure 3.7 is a proposal by JPL [Tanner, 1992] for an ESTAR four-frequency thinned array. It has 1.4, 6.8, 18, and 37 GHz elements with resolutions of 10 km for the low frequencies and 5 km for the high frequencies. Increased resolution requires proportional increase in dimensions (9.1 m to 91 m, resolution goes from 10 km to 1 km) and  $\log_2 N$  increase in the number of elements (14 to 19 elements for 9.1 m to 91 m). Thus, as the number of elements increase, the circuit complexity increases as  $2^N$ .

Two other important parameters are revisit time, the time required for a sensor to take a second image of a specified scene, and search rate, which is the amount of area covered in a given time. Both are greatly influenced by the orbit and the swath width. High search rates require large swath widths and a larger number of elements for high resolution. Highly elliptical orbits can give high search rates at lower resolution for the high altitude and high resolution and low rates during the low altitude. These attributes are highly mission dependent. Table 3.4 shows the swath width for a 50 element array along with search rate and revisit times for a 400 km circular orbit.

To produce 100 meter resolution requires an aperture around  $5000\lambda$ . At frequencies below 5 GHz this leads to very large structures, such as 1000 m at 1.4 GHz. This is probably unrealistic for real apertures, while thinned arrays offers obvious advantages. Even so, 100 meter arrays with 1 km resolution will be technically challenging. As the frequency increases, reflector systems become more practical. Parabolic antenna systems offer many useful features such as wide bandwidth (useful for multiple frequency), multiple polarizations, and real beam imaging. In contrast, thinned arrays require large amounts of electronics, and an inversion algorithm to produce imagery.

Thinned arrays offer the biggest advantages for the lower frequencies where very large apertures are needed and reflectors are impractical. The cross-over to real apertures is not clear. Up to 5 GHz thinned apertures do well and from 20 GHz up real apertures offer advantages. The middle ground depends on technology and application. Real aperture systems should use folded optics for best off-axis performance advantages with  $F$  numbers as large as practical. An  $F5$  system with an array of 4 x 50 elements gives 200 pixels in the swath with Nyquist sampling.

Larger swath widths will require either a larger F system or poorer off axis performance. The specific application will govern the compromise between performance and cost.

TABLE 3.1												
Ground Resolution vs Frequency for 4, 10, and 17 m Antennas												
freq	Beam width km											
	4a	4b	4c	4d	10a	10b	10c	10d	17a	17b	17c	17d
1.4	31.50	27.21	24.64	21.64	12.60	10.89	9.86	8.66	7.41	6.40	5.80	5.09
6	7.35	6.35	5.75	5.05	2.94	2.54	2.3	2.02	1.73	1.49	1.35	1.19
10	4.41	3.81	3.45	3.03	1.76	1.52	1.38	1.21	1.04	0.90	0.81	0.71
19	2.32	2.01	1.82	1.59	0.93	0.80	0.73	0.64	0.55	0.47	0.43	0.38
22	2.00	1.73	1.57	1.38	0.80	0.69	0.63	0.55	0.47	0.41	0.37	0.32
37	1.19	1.03	0.93	0.82	0.48	0.41	0.37	0.33	0.28	0.24	0.22	0.19
90	0.49	0.42	0.38	0.34	0.20	0.17	0.15	0.13	0.12	0.10	0.09	0.08
140	0.32	0.27	0.25	0.22	0.13	0.11	0.10	0.09	0.07	0.06	0.06	0.05
	Taper		Side lobe									
a	$\cos^2$ to 0		-31 dB						altitude 400 km			
b	$\cos$ to 0		-25 dB									
c	$1-r^2$ to 1/3		-23 dB									
d	uniform		-18 dB									

TABLE 3.2				
Noise Levels for Real Beam Systems				
Frequency	Noise Levels K			
	4	Diameter 10	17	Amp NF
1.4	0.0283	0.0376	0.0491	1.2
6	0.0254	0.0402	0.0524	1.5
10	0.0283	0.0447	0.0583	2.0
19	0.0315	0.0499	0.0650	2.5
22	0.0315	0.0499	0.0650	2.5
37	0.0439	0.0694	0.0904	4
90	0.0548	0.0866	0.1130	5
140	0.0686	0.1084	0.1414	6
Altitude	400 km			

TABLE 3.3  
Noise Level for Synthesized System

Noise Level, K			
Frequency	4	10	17
1.4	0.0517	0.2043	0.4528
6	0.2373	0.9382	2.0794
10	0.4438	1.7544	3.8886
19	0.9462	3.7400	8.3899
22	1.0956	4.3306	9.5988
37	2.6026	10.287	22.803
90	7.9699	31.503	69.829
140	15.608	61.695	136.75

16- 1/2 wavelength elements  
400 km altitude

TABLE 3.4  
Array Width, Swath Width, and Search Rate

Freq	4m			10m			17m		
	Array Width Beams	Swath Width km	Search rate km <sup>2</sup> /sec	Array Width Beams	Swath Width km	Search rate km <sup>2</sup> /sec	Array Width Beams	Swath Width km	Search rate km <sup>2</sup> /sec
	km	km <sup>2</sup> /sec	km <sup>2</sup> /sec	km	km <sup>2</sup> /sec	km <sup>2</sup> /sec	km	km <sup>2</sup> /sec	km <sup>2</sup> /sec
1.4	12	588	4242	18	353	2545	30	346	2495
6	24	274	1979	38	174	1254	48	129	932
10	30	206	1485	48	132	950	50	81	582
19	42	152	1094	50	72	521	50	42	306
22	46	143	1035	50	62	450	50	37	265
37	50	93	669	50	37	267	50	22	157
90	50	38	275	50	15	110	50	9	65
140	50	24	177	50	10	71	50	6	42

Altitude 400 km  
Array width where BS = 1.5 \* center BW

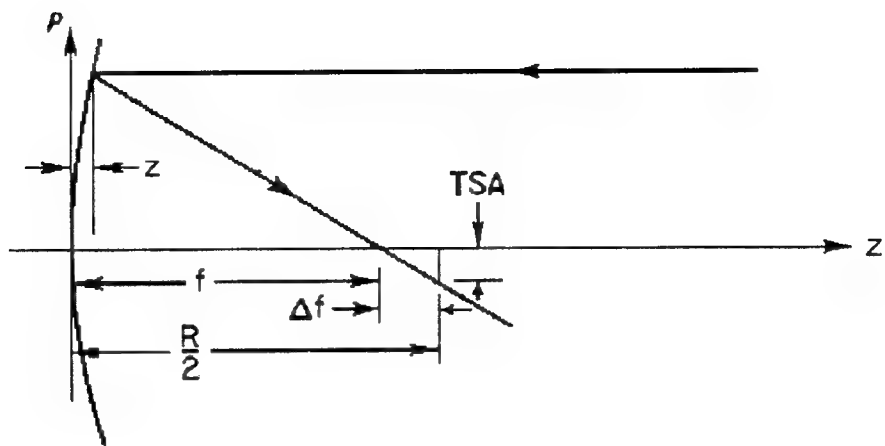
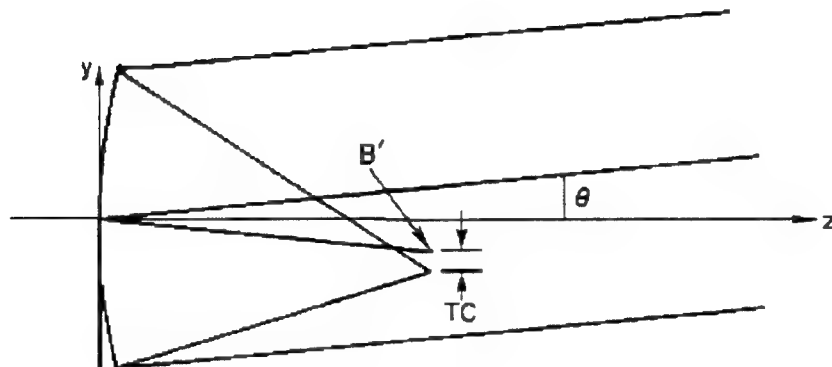
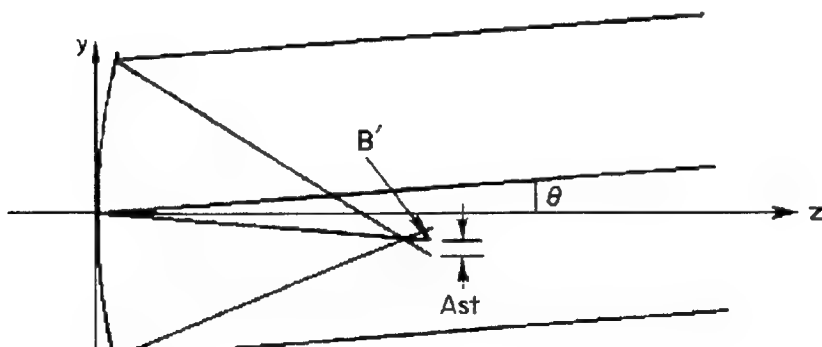


Figure 3.1 Spherical aberration



(a)



(b)

Figure 3.2 Off axis aberrations.  
(a) coma (b) astigmatism

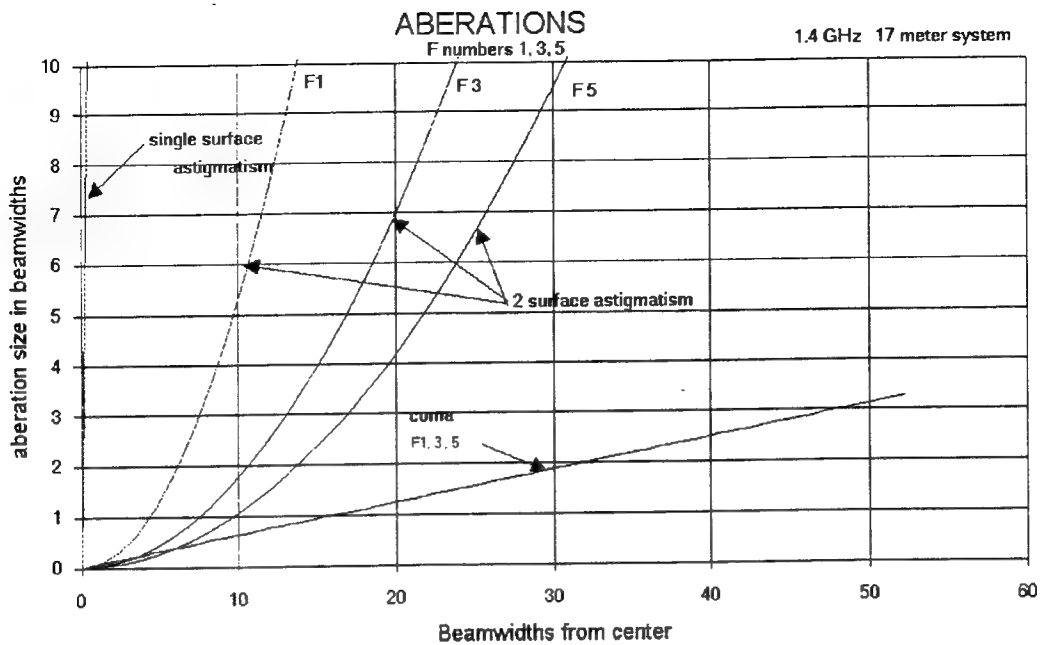


**Figure 3.3a** Aberrations 1.4 GHz 17 meter

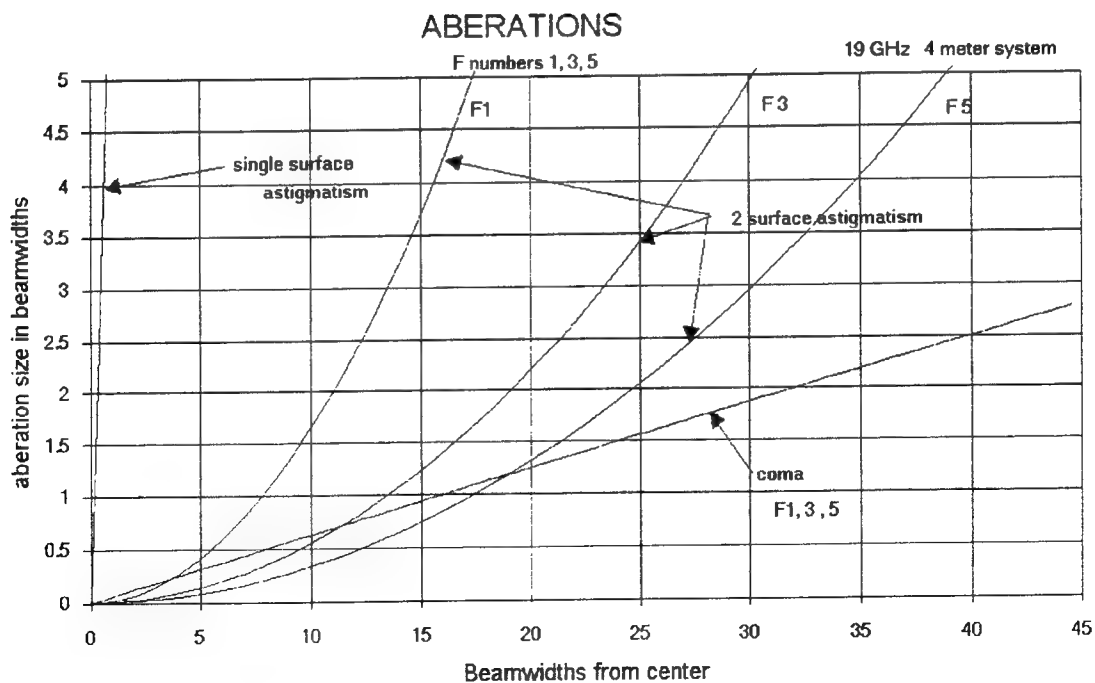


**Figure 3.3b** Aberrations 19 GHz 4 meter

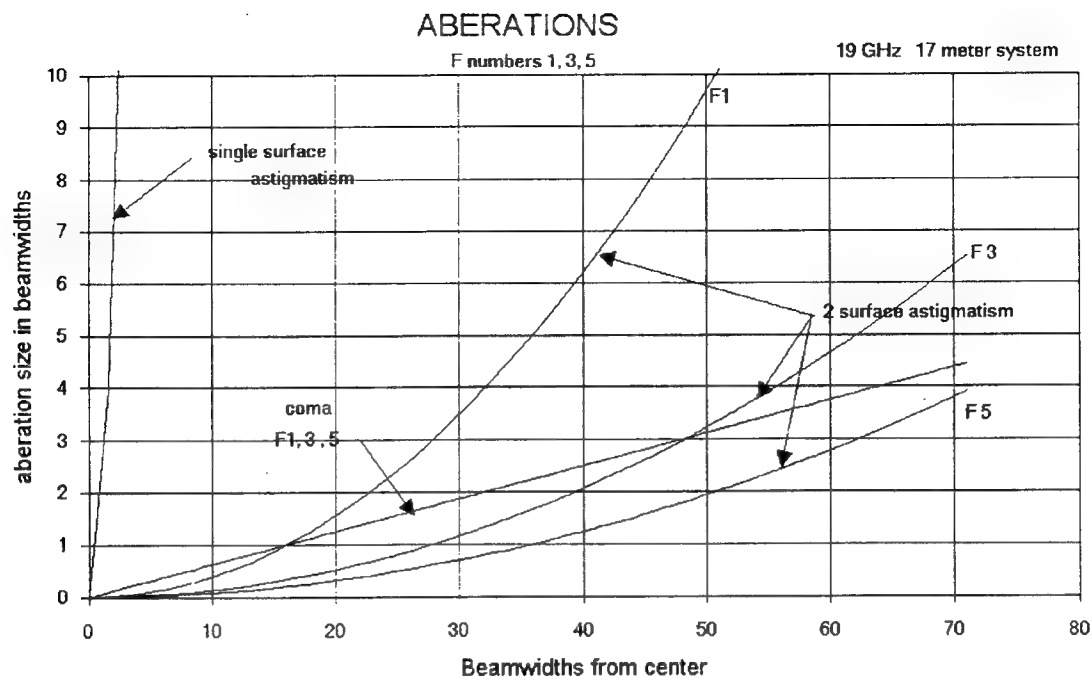


**Figure 3.3c** Aberrations 19 GHz 17 meter

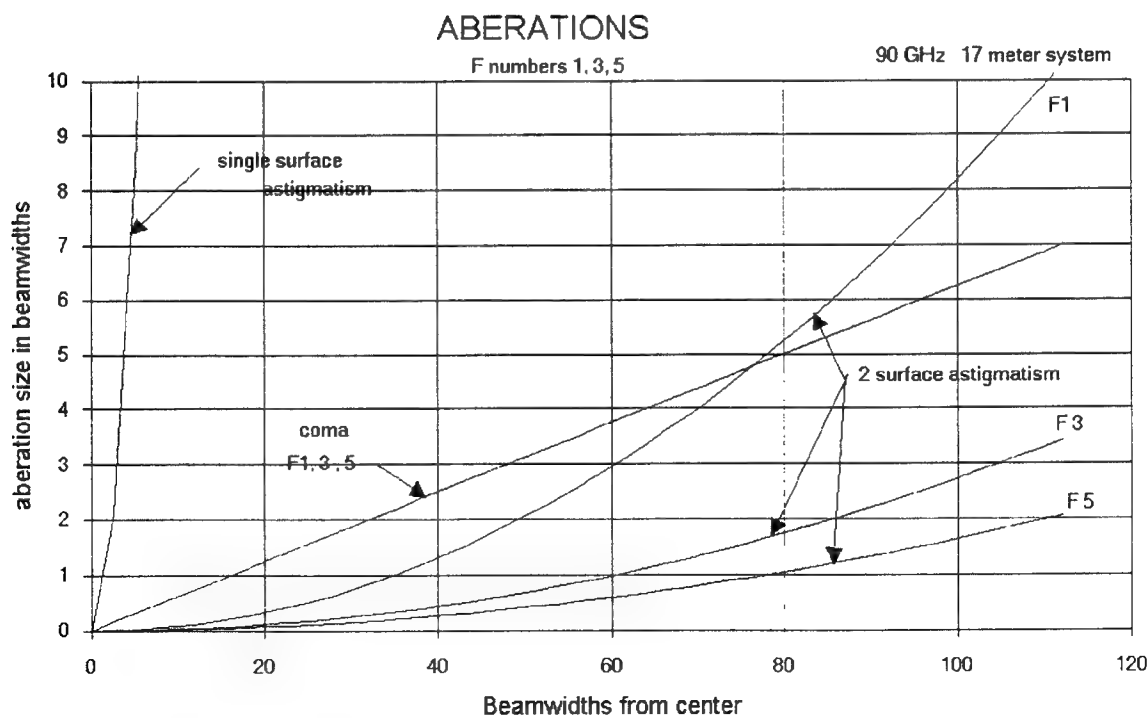


**Figure 3.3d** Aberrations 90 GHz 17 meter

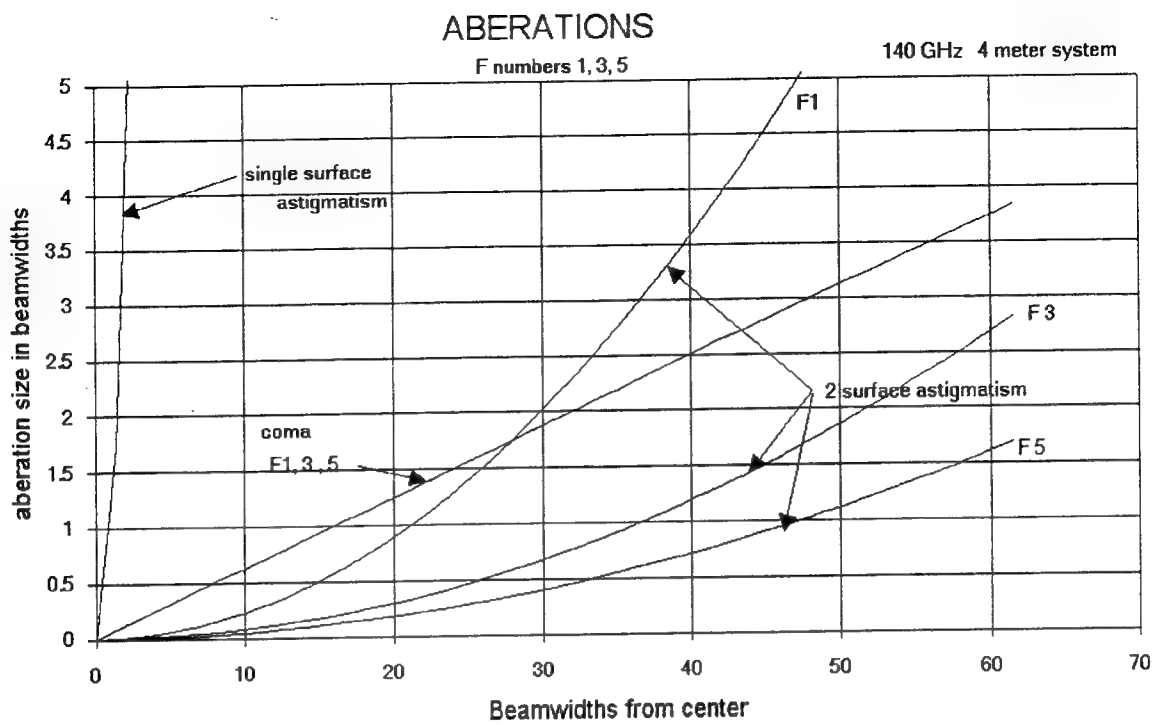


Figure 3.3e Aberrations 140 GHz 4 meter

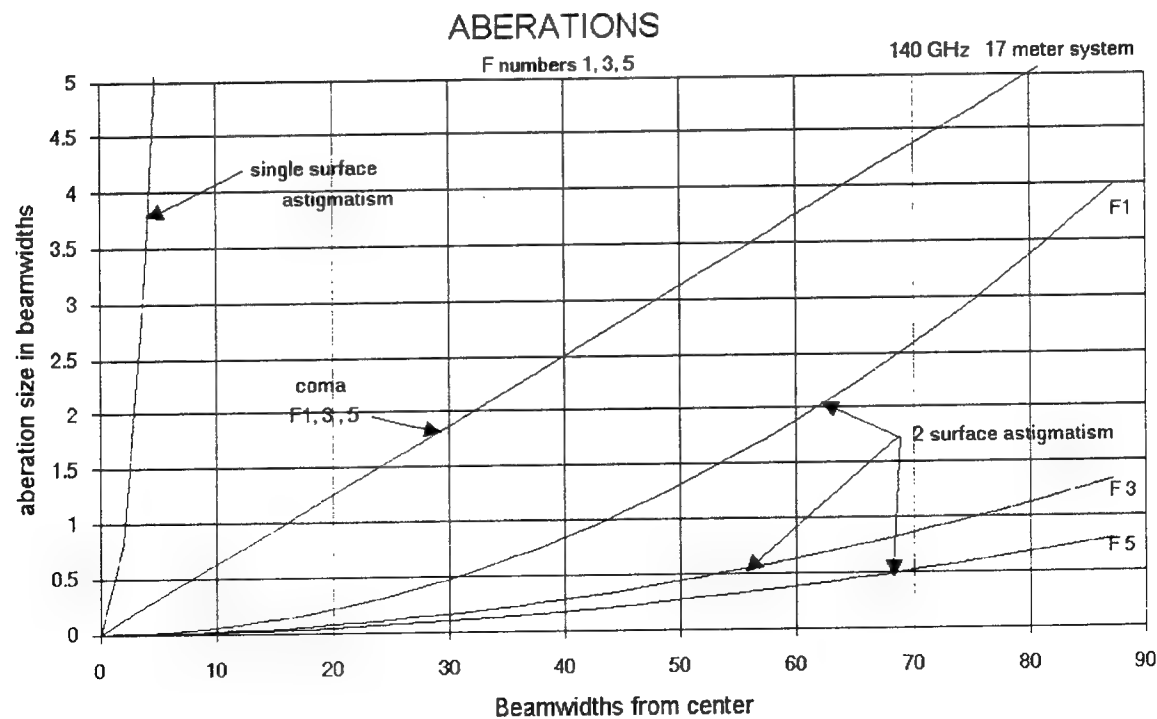
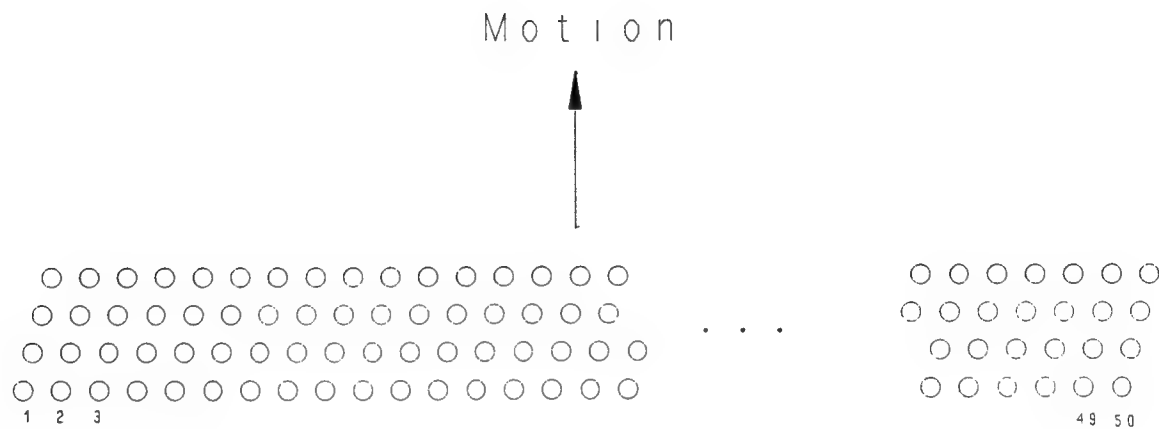
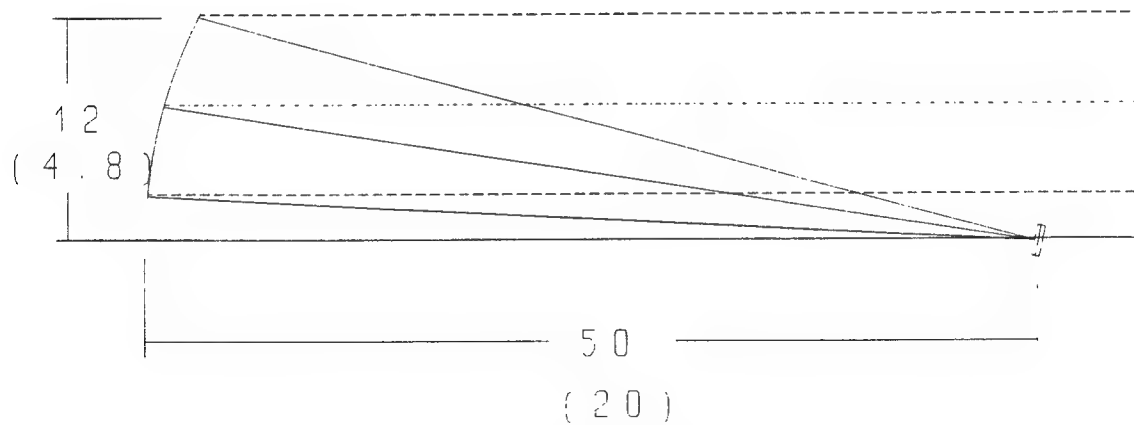


Figure 3.3f Aberrations 140 GHz 17 meter



**Figure 3.4** System Footprint



**Figure 3.5** F5 Parabolic Reflector

4 meter system

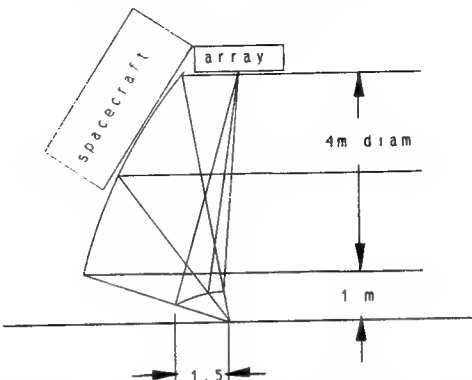


Figure 3.6a 4 Meter Folded Cassegrain

10 meter system

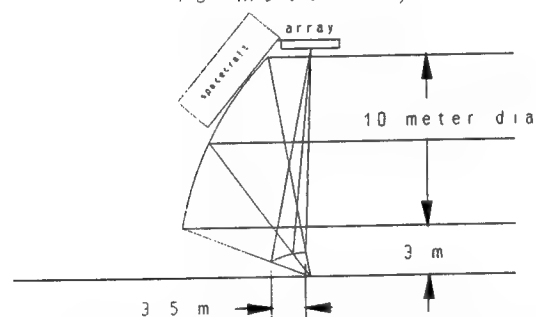


Figure 3.6b 10 Meter Folded Cassegrain

17 meter system

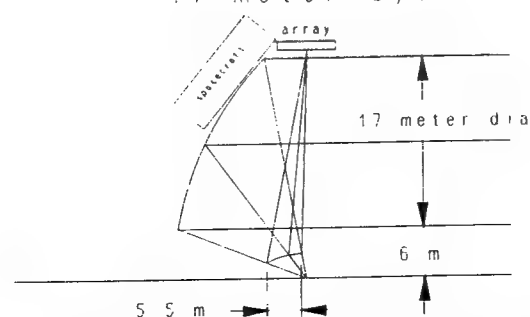


Figure 3.6c 17 Meter Folded Cassegrain

## 4.0 REMOTE SENSING OF THE ENVIRONMENT

Natural microwave radiation contains information about the geometric and bulk-dielectric properties of the surface and the atmospheric volume observed. The intensity of the upwelling microwave radiation depends upon the frequency, the polarization, the incidence angle of the observation, the emissivity of the scene, and the transmission through and radiation from the atmosphere. In turn, the emissivity of the scene is closely related to the physical properties of the surface such as salinity and sea temperature for the ocean, and soil moisture and vegetation for land. Microwave radiometers respond to a wide variety of atmospheric and terrestrial phenomena, enabling measurement of such geophysical parameters as sea surface temperature and winds, soil moisture, snow cover extent, atmospheric water vapor profiles, and cloud liquid water content. In addition to inferring physical properties of scene constituents, a microwave radiometer can also produce high resolution images showing geographical features, weather systems, and man-made structures. This section discusses passive microwave remote sensing of terrain features such as soil moisture, vegetation, surface types, and snow cover. Sea surface parameters such as temperature, salinity, winds, and ice are also covered. Lastly, satellite measurements of the atmosphere including water vapor, temperature, clouds, rain, and aerosols are discussed.

### 4.1 Terrain

#### 4.1.1 Soil Moisture

Water is one of the most important substances in the Earth's system. It is not only an essential ingredient to all forms of life, but water also plays a key role in the geophysical processes of the Earth, such as climatology and geology. Water's importance in a variety of science disciplines has brought hydrology to the forefront as an area that must be studied to understand better the Earth as a system. The transfer of energy and moisture between the atmosphere and the Earth is coupled to hydrological conditions such as soil moisture concentration and surface temperature. Satellite-borne sensors cannot directly measure these energy fluxes, but surface conditions that drive these fluxes can be measured and integrated into models to estimate the earth-atmosphere energy and moisture fluxes [Murphy, 1987]. Some of the surface conditions of interest are soil moisture, vegetation cover, surface temperature, and snowpack, all measurable from space. Soil moisture plays a vital role in the Earth's hydrologic cycle by storing water and changing evaporation and transpiration rates of water into the atmosphere. Furthermore, the water in the top layer of the soil changes the soil's thermal conductivity and heat capacity.

Soil moisture data also serves as a boundary condition in climate models and has applications in land management, agriculture, and flood forecasting. The microwave emission from bare soil varies with the soil moisture because of the high contrast between the emissivity of dry soil and water. The emissivity of dry soil is nearly independent of frequency and ranges from 0.9 to 0.95. As water is added to the soil, the emissivity decreases with increasing water content and wavelength. Typically, very wet soil has emissivities in the range of about 0.5 at

L-band to 0.7 near 100 GHz. The depth of the soil layer that contributes to the brightness temperature is important in determining the feasibility of various observation wavelengths. Deeper sampling depths offer more information about the soil profile, and increase the "memory", or length of the history, of the surface layer. For moist soils, the sampling depth is on the order of a tenth of a wavelength, or about 3 cm at 1 GHz and .3 mm at 100 GHz.

The remote sensing and hydrology communities have used airborne L-band radiometers extensively to measure soil moisture [Schmugge, 1983], [Griffis, 1993]. Wavelengths at this frequency, about 21 cm, penetrate ground vegetation and provide a moisture sampling depth of 2 - 5 cm. The L-band Pushbroom Microwave Radiometer, developed by NASA, estimated volumetric soil moisture to within 2% through burned and unburned prairie [Wang et al., 1990]. The presence of vegetation has limited attempts to measure soil moisture at higher frequencies, but observations at C-band and above can be used to remove the effects of vegetation on L-band measurements. Neale et al. [1990] used SSM/I data to classify various land types and vegetation covers. Dual polarization data at 19, 37, and 85 GHz and 22 GHz vertical data enabled Neale et al. to distinguish desert, semi-arid, arable land, and dense vegetation, as depicted in Figure 4.1.

Observations with the 85 GHz channel of the SSM/I have shown that it is possible to identify high contrast features of terrain, such as wet-land-dry-land boundaries of rivers and lakes. Such observations can be made even when the sensor's beam size at the surface is greater than 5 - 10 times the size of the feature, depending on the amount of moisture. It should be possible, therefore, at resolutions of 100 - 400 m to see the wet condition of features as small as roadways, streams, bogs, topographical drainage, and pollution patterns. For example, because the spatial frequencies of significant mountain and natural drainage topography range from 100 m to 1 km, high resolution radiometer imagery could produce complete topographical maps of soil moisture in areas without dense vegetation for hydrological and military purposes.

Examining a set of SSM/I images of the southeastern United States and the Gulf of Mexico demonstrates the dramatic effects of soil moisture and wet surfaces on the microwave signature of the Earth. Figures 4.2 and 4.3 show the 85 GHz horizontal and 37 GHz horizontal images, respectively. The 85 GHz colorbar extends from 150 K to 290 K; the 37 GHz color bar covers 110 K to 290 K. A cover of thick nimbostratus and cumulus clouds moves across the region, accompanied by light rain. A band of dense clouds and heavy precipitation extends over the Gulf and across the middle of Florida. Microwave imagery of the land areas reveals areas of cooler brightness temperatures with the most pronounced contrast in the Mississippi valley.

The decrease in brightness largely results from increased soil moisture and areas of standing water. Thoroughly moistened soil has an emissivity of 0.7 or less at 85 GHz and even less at 37 GHz and below. Light to moderate rains can reduce brightness temperatures by 50 K or more. An increase in soil moisture also increases the polarization difference, from about 50 K dry bare soil to near 80 K for very wet bare soil so that dual polarization measurements can distinguish wet soil signatures from other, less polarized effects. The northwest region of the Gulf of Mexico has clear skies so the image is of the ocean surface in both cases. There is more cloud cover over the rest of the Gulf. The clouds slightly attenuate the 37 GHz radiation, so that the image experiences brightening. More brightening occurs where the clouds are thicker and where there is precipitation. In the 85 GHz image, the clouds block more of the underlying

radiation and emit more radiation directly. The exception is in areas of intense rain where scattering reduces the brightness temperature significantly. It is also interesting to note that the band of rain-producing clouds over Florida completely obscure the land at 85 GHz, while only partially affecting the 37 GHz radiation. The emission from this cloud system decreases with decreasing frequency. In the 85 GHz image, the dark area in the Mississippi valley could be interpreted as thick cloud cover and rain. On the other hand, the 37 GHz image responds weakly to the dark area over Florida and strongly to the Mississippi valley radiation. A comparison of these two images suggests that the effect in the Mississippi region results from increased ground water, while clouds produce the effect over Florida.

#### 4.1.2 Surface and Soil Classification

Radiometric imaging can distinguish broad categories of surface types. Figure 4.1 shows distinct surface classes over the globe as observed by the SSM/I 85 GHz channel with 12.5 km resolution. On a more localized scale, the brightness temperatures observed for a range of soil types and soil/vegetation composites are illustrated in Figure 4.4 for the Western coast of Africa. Differing types of soil, including texture and amount of soil moisture, and vegetation cause the brightness temperatures to vary. The brightest (whitest) regions toward the North are the great sand dunes, such as Azefal Dunes and Akchar. The grey-white colors represent the rocky, sandy soil and mountainous regions of the Sahara Desert. The brown-white region immediately south-east of Nouakchott corresponds to mixed dry and arable land in the transition region between desert and forest. The brown-green along the Southern coast identifies the Ivory Coast, a composite of arable land and forest. The darkest green identifies the lush forested region of the Niger Delta. The white patterns over the sea and land to the south are clouds and humid air. The small, turquoise and yellow regions within the white clouds are cumulonimbus convection.

Surface roughness also affects the microwave response of soil and vegetation. For soil, random surface roughness increases the emissivity and decreases the polarization difference [Wang et al., 1983]. Periodic roughness features such as a freshly plowed tract change the effective incidence angle for small resolutions. Dual polarization measurements at L-band have been used to identify plowed farmland [Gaiser, 1993]. At higher frequencies, above 37 GHz, the increase in emissivity is smaller, but still discernible. Therefore, a freshly plowed tract or an unpaved roadway roughened by passage of heavy military vehicles, for example, should appear slightly brighter than smoother ground in high resolution microwave imagery. Another example is the measurement of volcanic lava flow morphology and topography. Recent investigations of lava flows [Gaddis et al., 1989] have shown that spatial variations in the surface textures on lava flows can be identified from Space Shuttle radar images, and demonstrate the potential for remote sensing at millimeter wavelengths to map the distribution of different kinds of lava over an entire volcano. The potential exists, at 100 - 400 m resolution, to measure flow position and volume during eruptions, even under cloud cover, for prediction or other purposes. Orbiting platforms could be used to detect the rate of change of volcanic landforms such as domes, cones, and calderas via frequent imaging of the volcano by a high-resolution microwave system.

#### 4.1.3 Wetlands

Wetlands are yet another area of hydrological and environmental concern. Both coastal and inland wetlands can change rapidly. To cite two examples, the Florida Everglades and the Mississippi Delta have undergone significant changes over the past few decades. This affects the natural habitat and breeding grounds of countless species of animals and plants. Furthermore, it is important for the military to know the extent of coastal wetlands for littoral warfare operations. Microwave radiometry has the capability to map wetlands and distinguish them from water and wet soil. Figure 4.5 show marshes on the lower Delmarva Peninsula mapped by the L-band ESTAR-A, which operates on a NASA P-3 [LeVine et al., 1990]. Images such as this allow monitoring of changes in the wetland extent. The higher dielectric constant and increased polarization of water enabled Neale et al. to flag regions with flood conditions or other significant amounts of standing water [Neale et al., 1990]. Continuous monitoring of regions over time will permit the distinction of temporary flood conditions from permanent wetlands or lakes.

#### 4.1.4 Vegetation

The appearance of vegetation in microwave imagery, as in Figure 4.4, is a combination of modified radiation from the underlying soil and emissions from the vegetative canopy itself. Both of these processes depend on the optical thickness of the vegetation or biomass present. Plants consists of aggregates of cell-sized liquid water and fibrous structures that absorb and scatter radiation from the soil below. Also, plants are very good emitters, having emissivities of 0.80 - 0.95. The soil beneath significant amounts of vegetation usually is moist, so that (for nearly equal thermometric temperatures) the higher emissivity of vegetation produces higher brightness temperatures. Vegetation, therefore, appears warmer than the surrounding moist ground by an amount that depends upon the type of vegetation. Furthermore, the degree of polarization for radiation from dense vegetation is less than that of bare soil [Ulaby et al., 1983]. Because the plant's absorption and scattering attenuate the soil's emission, radiation from the soil/vegetation composite has a lower polarization difference, which approaches zero for a lush rainforest. Thus, the microwave sensors can estimate the amount of vegetative cover. In addition, Brunfeldt and Ulaby [1984] showed that metal/vegetation composites have emissivities significantly less than those of soil/vegetation composites. Orbiting high resolution microwave sensors would be capable, for example, of distinguishing non-vegetative military camouflage from true vegetative canopies. Also, man-made clearings could be distinguished from river tributaries and deforestation could be monitored.

Plant diseases and drought create vegetative stress and have significant negative effects on its emissions. For example, as vegetative moisture decreases, the emission, absorption, and scattering of the plants also decrease, and the effects on radiation from the soil are reduced. The emissivities of stressed vegetation usually drop to about 0.87 or less. As the biomass dies, the radiometric effect is similar to increased soil roughness; thus, soil/vegetation composites with unhealthy plants have a higher degree of polarization. Low frequency microwave radiometer data could provide quantitative information about the effects of a drought. A high resolution microwave imager would be capable of monitoring the vegetative stress of diseased forests or

crop-lands on a scale of a few hundred meters, during the incipient stage before irreversibility to good health occurs. Damage assessments would be possible for these areas and also for regions of significant wind damage.

#### 4.1.5 Snow Cover

The microwave response to snow is complex and quite different from that of ice and water because snow consists of a mixture of varying amounts of air, ice, and water over a background of soil or vegetation. Above 20 GHz, dry snow not only reduces the polarization difference of the radiation of the underlying soil, but scatters the radiation from below because the snow particles and air pockets are comparable in size to a wavelength. The scattering asymptotically approaches a maximum value as the depth increases, so the brightness temperature decreases. Snow is much colder radiometrically than soil and becomes colder as the depth increases and this effect increases with microwave frequency. Figure 4.6 shows an SSM/I image of snow at 85 GHz on a clear day, with the color bar ranging from 150-300 K. Normal snow-free local variations in 85 H brightness temperatures in the United States rarely exceed 15 K for a given amount of soil moisture. Following this mid-winter snow storm in the Great Lakes region in 1988, the surface variations, red to green, increased up to 50 K in the midwest. The green belt south of Lake Michigan represents several inches of snowfall.

Wet snow behaves dramatically differently from dry snow. Water in the snowpack increases the composite's extinction of radiation from the soil by absorption and reduces the scattering induced extinction. As the wetness increases, snow approaches the non-scattering characteristics of a blackbody radiator. Therefore, wet snow is radiometrically brighter than dry snow and has a higher polarization difference because the water in the snowpack creates a greater discontinuity at the snow-air boundary.

As a snowpack melts and refreezes repeatedly, and becomes more densely packed, it scatters radiation from the ground more efficiently. The age of the snowpack, therefore, will be associated with distinctly different ranges of brightness temperatures as shown in Figure 4.7. The average spectra for brightness temperatures,  $T_B$ , have been observed [Schanda et al., 1983] at horizontal, H, and vertical polarizations, V, for (a) winter-snow conditions, (b) a wet firm layer at least several centimeters thick on the surface of the snow cover, and (c) a thick crust, at least several centimeters, of refrozen firm. The snow depths for all three conditions have been normalized to a 48-cm water equivalent. Snow water equivalent quantifies the amount of water in a snowpack and is the height in centimeters of liquid water in a column of snow with a horizontal cross-section of one  $\text{cm}^2$  [Ulaby et al., 1986]. For dry snow, both the extinction coefficient and the albedo increase with frequency so that at a given snow depth, or water equivalence,  $T_B$  decreases with frequency. The two sets of spectra obviously differ in two respects, however: (1) the polarization difference,  $T_B(V) - T_B(H)$ , is much larger for winter snow than for spring snow, and (2), the brightness temperature of dry spring snow decreases faster with increasing frequency than the brightness temperature of winter snow. This behavior results from differences in the shapes and sizes of the ice crystals characteristic of the two conditions. New snow crystals are granular and aspherical in structure, which causes a strong polarization

dependence in winter snow; however, crystals become more spherical after several cycles of melting and refreezing, a characteristic of spring snow. The melting and refreezing process also produces larger crystals, because the snow crystals combine with one another. This, in turn, leads to more scattering, or a larger albedo, and consequently, the response of spring snow depends strongly on frequency. At 90 GHz, the dynamic range of brightness temperatures for these different snow types is about 100 K, whereas 10 GHz vertical data vary less than 20 K for the three snow types.

Remote sensing of snowpack attempts to determine three geophysical parameters: the extent of the snow cover; the water equivalent of the snowpack; and the onset of melting. Snow extent is probably the easiest of these parameters to quantify. Channels at 37 GHz and 19 GHz can usually define the snow boundary with land because of the sharp contrast between land and dry snow at these frequencies and the ability to penetrate the atmosphere at these frequencies. However, care must be taken not to confuse melting snow with wet soil. Multiple observations during different conditions, including at night after refreezing, help delineate the snow-land boundary. In addition, dual polarization measurements can separate land features, which are less polarized, from dry snowpack features.

The snow water equivalent is the most crucial parameter in snow hydrology because it indicates the amount of water being added to the hydrological system. However, determining snow water equivalent requires information about the snowpack depth, the snow type, the snow wetness, the density of the snowpack, and the ground below the snowpack. Therefore, it is difficult to accurately estimate snow water equivalent. In addition, snowpack properties are a strong function of the geographic location and season so that a global algorithm would be virtually impossible. The large number of snow properties that influence the snow water equivalent make this area extremely challenging. An example of the problem is given in Figure 4.8, which illustrates that for snow of a given grain size, microwave emission decreases with water equivalence, but an increase in grain size also causes the emission to decrease. The most successful estimations of snow water equivalence so far came from multifrequency and dual polarization measurements of shallow, dry snow fields [Murphy, 1987].

The onset of melting dramatically changes the microwave emission from the snow. The absorption of the snow increases and internal scattering decreases causing a rise in the brightness temperature. This effect is especially evident at frequencies above 10 GHz. For example, the first 1-2% of volumetric snow wetness can cause the brightness temperature to increase 50 K at 37 GHz [Ulaby and Stiles, 1980], [Hofer and Matzler, 1980]. In addition, the high degree of polarity evident in dry snow decreases as snow melts and water becomes more prevalent. As the snow continues to melt and the wetness exceeds 5%, the emissivity begins to drop for higher microwave frequencies. The appearance of melting snow is difficult to distinguish radiometrically from extremely wet soil. Previously, the only reliable way to identify the two cases has been a temporal approach to the snow-melt history of the area. High resolution radiometry, however, may provide the additional aid of the imagery of the local topography and the morphology of the snow-melt run-off.

## 4.2 Oceans

The emissivity of a target depends on its dielectric properties. Because water is a polar molecule, it has a large dielectric constant at microwave frequencies, which implies a large reflectivity and low emissivity for liquid water surfaces such as the ocean. Most natural solid surfaces have emissivities on the order of 0.85-0.95 whereas water emissivities range from 0.35 at 1 GHz to about 0.7 at 90 GHz. Across the spectrum, the emissivity of the ocean depends on wind speed, sea surface temperature (SST), sea surface salinity (SSS), and frequency. Figure 4.9 shows the spectra of normalized radiometric sensitivity to the three aforementioned parameters plus atmospheric liquid water and water vapor. The low emissivity and relative homogeneity of the open ocean also make it a good background for viewing the intervening atmosphere.

### 4.2.1 Sea Surface Salinity and Temperature

Salinity plays an important role in ocean circulation, air-sea interaction, and the evaporation-precipitation balance, all of which are critical to the climate [Swift and McIntosh, 1983]. The radiometric sensitivity to salinity decreases as frequency increases [Klein and Swift, 1977], so that the effects of salinity are negligible above 4-5 GHz. Salinity has not been mapped from space because of the aperture size needed at these low microwave frequencies. However, scientists have conducted several experiments involving airborne radiometer retrievals of salinity. Thomann [1976] used an L-band (1.4 GHz) radiometer and an infrared radiometer and reported salinity measurements with an accuracy of two ppt (parts per thousand) at the mouth of the Mississippi River where typical salinity concentrations range from five to 30 ppt. Blume et al. [Blume and Kendall, 1982], [Blume et al., 1978] mapped the salinity in the lower Chesapeake Bay using 1.4 and 2.65 GHz radiometer measurements. Comparisons with sea truth revealed agreements within one ppt. More recently, the ESTAR-A L-band radiometer detected salinity changes in the open oceans, where salinity ranges from 32 to 36 ppt [Lagerloef et al., 1992]. All these measurement systems used 1.4 GHz data because of its high sensitivity to salinity, and an auxiliary channel to account for the sea surface temperature effects.

Sea surface temperature also provides valuable information regarding ocean currents, eddy behavior, and air-sea interface dynamics. The curve in Figure 4.9 shows that the sensitivity to SST peaks near 5 GHz. Measurements in this band have the additional advantage of almost no sensitivity to salinity changes and limited sensitivity to wind speed. Spatial resolution of 5 km or less near 6 GHz would enable precise measurements of eddy currents and shear waves [Murphy, 1987]. The radiometric sensitivity to SST can be positive or negative with the zero-crossing depending on the frequency, polarization, and the incidence angle [Ulaby et al., 1986]. At nadir, the sensitivity curve crosses zero near 37 GHz for sea water. For 50 degree incidence at 37 GHz, the sensitivity is positive for vertical polarization and negative for horizontal polarization. Because the sensitivity peaks near 5 GHz, this region is the most popular for SST measurements. For example, the Nimbus-7 SMMR sea surface temperature retrievals relied primarily on the 6.6 GHz vertical channel and had an accuracy of 1.8 °C [Milman and Wilheit, 1983].

#### 4.2.2 Sea Surface Winds

Sea surface winds greatly affect the microwave emissivity. As the sea surface becomes rougher, the emission increases and the degree of polarization decreases [Wentz, 1992]. Three primary mechanisms cause this effect. Surface winds create areas of foam on the sea. Foam, a mixture of air and water, acts as a partial matching element between the sea and the air, thus reducing the reflectivity. Consequently, sea foam has a higher emissivity than the water itself and increases the brightness temperature of the ocean surface. For winds above 15 m/s, foam may account for as much as half of the wind speed microwave signature [Smith, 1988]. The fractional foam coverage quantifies the effect of the foam. Secondly, the wind generates surface waves that are long compared with the radiation wavelength. These waves change the local incidence angle and mix the horizontally and vertically polarized waves. The RMS slope of the large waves quantifies this effect. Lastly, the capillary surface waves, which are small compared to the radiation waves, diffract the microwave radiation. The RMS height of these small-scale waves describes this phenomenon.

Several satellite-borne radiometer systems have successfully measured the sea surface wind speed. The Nimbus-7 SMMR system relied heavily on the 10.7 GHz horizontal channel and secondarily on both 18.7 GHz channels. The SMMR wind speed retrievals had a standard deviation on 3.0 m/s [Wilheit et al., 1984]. The SSM/I ocean wind speed retrievals used vertically polarized data at 19, 22, and 37 GHz, and horizontal data at 37 GHz. Figure 4.10 shows that in rain free areas, SSM/I measurements estimated the wind speed to within 2.0 m/s [Goodberlet et al., 1989]. Recent work by Wentz has demonstrated the possibility of determining the wind direction from SSM/I data [Wentz, 1992].

### 4.3 Sea Ice

#### 4.3.1 Ice Type

Radiometric measurements observe four unambiguous categories of sea ice: newly formed (young) ice with thickness up to 30 cm; first year ice (FY), which has yet to go through the annual process in which the upper layers melt and refreeze, with thickness between 30 cm and 1.2 m; second year ice (SY) with thickness 1.2 m - 2.5 m; and multi-year ice (MY), with thickness greater than 2.5 m, which has undergone at least one melt cycle; sometimes young ice will be grouped with FY ice, SY ice with MY ice. The inherent distribution of emissivities of all ice types is sufficiently well separated to allow each ice type to be distinguished by its microwave signal. However, the effects of the surface temperature and winds, and the atmosphere must also be considered to make reliable estimates of sea ice parameters.

Newly formed ice, or young ice, has a salinity level of about 15 ppt and is usually less than 30 cm thick. With very thin ice, the underlying water contributes to the radiometric emission. Attempts to infer sea ice thickness have shown that the emissivity of sea ice oscillates coherently with the ice thickness, frequency, and dielectric properties of the sea ice. To directly determine the ice thickness, we must operate at frequencies much lower than 1 GHz [Ulaby et

al., 1986]. In general, for microwave observations above 10 GHz, the ice can be considered opaque and the effects of the underlying water can be ignored for thicknesses greater than 20 cm.

The higher salinity of FY ice makes it optically opaque, and, therefore, its microwave signature is almost frequency independent as implied by the data in Figure 4.11 [Troy et al., 1981]. In contrast, the emissivity of MY ice decreases rapidly with frequency to a minimum near 90 GHz [Hollinger et al., 1984]. The virtually desalinated outer portion of MY ice makes it optically thin because the radiation emanates from a thicker layer of old ice. Volume scattering within the ice caused by air pockets formed during summer melt and brine drainage suppresses a significant fraction of the radiation from old ice. The emissivity of MY ice, about 0.9 at 19 GHz and 0.8 at 90 GHz, is lower, therefore, than that of FY ice.

The large difference in emissivity between FY ice and MY ice at higher frequencies leads to more information content, because of greater contrast, in the imagery of an ice field. The situation in a melting or broken ice field is more complex. Figure 4.12 is a radiometric image of mixed fields of Arctic sea ice observed at 90 GHz from aircraft, showing the contrast between FY ice (blue) and MY ice (red). An analysis of this kind of imagery has yielded the population distribution versus temperature of ice types and open water in the Beaufort Sea in July 1983, as shown in Figure 4.13. Each curve is derived from an individual ice floe and from a single continuous area. The standard deviation for open water, a homogeneous microwave scene, approximately equals the instrumental noise of 1.4 K at 90 GHz. Thus, instrumental noise contributes a significant portion of the spread in the microwave signal for a single ice type. This broadening because of instrumental noise may be removed to obtain the standard deviation in the ice  $T_B$ . The inherent distributions of emissivities for all ice types thus are well separated.

MY ice may appear radiometrically colder than the sea. Because the sensitivity to volumetric scattering is inversely related to the wavelength of the radiation, the brightness distribution of MY ice varies more widely at 90 or 140 GHz than at lower frequencies. Figure 4.13 shows that the distribution overlaps that of open water. When the emissivities of MY ice and open water are the same, the higher degree of polarization of water makes it possible to distinguish ice from water. The volume scattering of the ice decreases the polarization difference compared to that for water.

The measurement of sea ice parameters becomes more complex when the radiometer footprint contains a combination of FY ice, MY ice, and open water. A radiometer channel measures a weighted average brightness temperature dependent on the relative contribution of the different constituents. For example, a combination of FY ice and sea water may have the same brightness temperature as a scene composed entirely of MY ice. Multi-frequency measurements and dual polarization observations can resolve this ambiguity because sea water is more highly polarized than sea ice. In addition, at frequencies below 40 GHz, the emissivity of FY ice is nearly independent of frequency, the emissivity of MY ice decreases with frequency, and the sea water emissivity increases with frequency [Wilheit et al., 1972]. These spectral differences can be used to find the concentration of water, FY ice, and MY ice within a resolution cell. Cavalieri

et al. [1984] determined the sea-ice boundary and ice type concentration with data from the NIMBUS-7 Scanning Multichannel Microwave Radiometer (SMMR) .

Snow frequently covers MY ice and older FY ice. The presence of snow on the ice increases the emissivity because the snow provides a smoother dielectric transition between ice and air, and therefore a better impedance match. Snow also insulates the ice from the lower temperatures of the air. Figure 4.14 shows the emissivities of FY ice with and without snow cover. The emissivity of FY ice changes at 90 GHz from about 0.92 to about 0.96 when snow is added. Figure 4.14 also suggests that the emissivity of snow covered FY ice is only slightly more frequency dependent than bare FY ice.

#### 4.3.2 Ice Zone Imagery

High resolution radiometry, at frequencies of 37 GHz and higher, can detect small icebergs, floes, and fractures, as well as ages and concentration, in most weather, on a scale less than currently measured with IR sensors. Clouds cover Arctic and Antarctic regions much of the time, so that all-weather capability is particularly important. At 100 - 400 m resolution, an orbiting microwave sensor could provide information necessary to guide a ship through ice fractures at night or beneath heavy cloud cover. The sensor could also predict ice breakage by sensing the boundaries between fresh ice and shelf ice--sites of frequent ice breaks. In another case, large icebergs, such as Antarctica's B-9 of 1987, tend to break from fractures in shelf ice because of interference from covered islands or flows of under-ice water current. Thin connecting ice, which precedes these fractures, could probably be identified because of anomalous variations of emissivity in MY ice, consistent with the pattern of fractures.

### 4.4 Atmosphere

#### 4.4.1 Water Vapor, Clouds, and Rain

The atmosphere is neither perfectly transparent nor opaque to microwave upwelling surface radiation. Instead, the extinction of the atmosphere varies locally between the two extremes, depending on the atmospheric conditions and the frequency. As a result, microwave and millimeter-wave radiometry can measure many weather and climatic features. The primary atmospheric constituents that affect the radiative transfer of the microwaves are liquid water in cloud droplets and rain, ice particles, aerosols, and molecular gases such as oxygen and water vapor. The concentration of these constituents along the line of sight decides the absorptive, scattering, and emissive profiles of the atmospheric source function. Figure 4.15 shows the spectral response of the atmosphere to water vapor and oxygen, based on the models of Waters [1976] and Rosenkranz [1975]. The applications to meteorology and climatology are obvious, but satellite altimetry and astronomy also use information about the atmosphere to correct for its effects on microwave propagation.

Microwaves are absorbed primarily by oxygen and water vapor, and to a much lesser extent by ozone and other gases [Ulaby et al., 1986]. The extinction caused by water vapor and

oxygen results from molecular absorption. An isolated water vapor molecule exhibits absorption resonances at 22.235 GHz and at 183.31 GHz that correspond to transitions between rotational quantum energy states [Chahine, 1983]. Oxygen has many absorption lines near 60 GHz and an isolated resonance at 118.75 GHz. Both water vapor and oxygen experience pressure broadening in the lower atmosphere where the abundance of molecules causes the absorption lines to spread; the individual lines of the 60 GHz oxygen complex blend in the lower atmosphere.

Satellite microwave remote sensing of the Earth's surface dictates using frequencies in the absorption "windows" between the resonances. However, satellite measurements near the absorption lines provide direct information about the atmosphere, enabling observations of the surface to be corrected for atmospheric effects. The distribution of oxygen in the troposphere is well known and depends on the temperature. Therefore, multifrequency measurements in the 60 GHz oxygen complex can be used to estimate the tropospheric temperature profile. Similarly, radiometric observations at the water vapor lines offer a method for predicting the distribution of water vapor in the atmosphere. Figure 4.15 shows that the strength of the 183 GHz water vapor line is approximately 100 times that of the 22 GHz line. The greater strength of the 183 GHz line offers the advantage of obscuring the background of the Earth's surface which would be visible at 22 GHz. When operating at 22 GHz, successful water vapor retrievals depend on reliable estimates of the background brightness temperatures, often limiting the water vapor retrievals to cases with ocean background.

Atmospheric liquid water varies spatially and temporally and is important for atmospheric studies. The opacity of clouds increases with cloud liquid water content and frequency because absorption and scattering increase with frequency. When the water particles are small compared with a wavelength, absorptive losses dominate scattering losses. This Rayleigh criterion remains valid to about 50 GHz for non-rainbearing clouds [Ulaby et al., 1986]. Below 10 GHz, clouds are very transparent to microwaves. Figure 4.16 shows the absorption and extinction coefficients of a cloud as a function of frequency. Notice that the scattering coefficient, the difference between extinction and absorption, is negligible below 50-60 GHz. The difference between absorption and scattering plays an important role in radiometry, because the emission, or brightness, from a scattering body differs from that of an absorptive body, even if the two have the same total attenuation. The brightness temperature of a scattering body results from reflections of energy incident upon the body; an absorptive body re-emits energy that it has absorbed. Therefore, if a cloud is viewed at 10 GHz and 90 GHz, the 10 GHz radiometer receives more radiation from the Earth below the cloud than the 90 GHz receiver. On the other hand, the 90 GHz channel receives more signal either emitted or scattered by the cloud.

Atmospheric water vapor and cloud liquid water are usually quantified in terms of profiles or total integrated values. Profiles of water vapor require several independent channels near a resonance. Scientists using microwave measurements near the 22 GHz water vapor resonance and in the adjacent window have successfully estimated the total integrated water vapor and liquid water in the atmosphere. The SSM/I sensor used channels at 19, 22, and 37 GHz to determine integrated water vapor and liquid water [Alishouse et al., 1990]. Scientists also

measured integrated water vapor and liquid with SMMR data. More recently, SSM/T-2 produced water vapor profiles at six levels with accuracies between 10% to 25% depending upon the type of atmosphere with the worst results occurring for very cloudy conditions [Falcone et al., 1993]. The SSM/T-2 sensor has three channels near the 183 GHz resonance line and channels at the 90 GHz and 150 GHz transmission windows.

The capability of passive microwave radiometers to measure rainfall depends largely on the contrast between rain regions and non-rain regions. The ocean offers an excellent background for observing rainfall emissions because ocean brightness temperatures are cold and stable. Land, on the other hand, has a much higher emissivity, which varies greatly depending on soil moisture, vegetation cover, snow cover, and other parameters. The effectiveness of the absorption/emission and scattering properties of hydrometeors depends strongly on frequency. Low frequencies are described in terms of their absorptive tendencies while high frequencies are best described by their scattering effects. Generally, the spectrum is divided into the emission regime ( $<19$  GHz) and the scattering regime ( $>35$  GHz) [Simpson, 1988]. Therefore, the most reliable methods of rainrate retrievals rely on multiple frequency measurements making use of known scattering-to-emission ratios.

The extinction coefficient of rain depends largely on the rainfall rate and frequency. For frequencies below 10 GHz and rainfall of a few millimeters per hour, the extinction is almost entirely absorptive and the scattering albedo is essentially zero. The scattering coefficient cannot be ignored above 10 GHz. Figure 4.17 shows the spectral variation of the scattering coefficient for three different rain rates. Not only does the scattering albedo increase with rain rate, it also increases with frequency up to a saturation level. In Figure 4.17, the albedo saturates at 60 GHz for the rain rate of 100 mm/hr, while the 0.25 mm/hr curve approaches saturation at 120 GHz. The former rate corresponds to an intense storm, while the latter typifies a light drizzle.

Several radiative transfer models exist to interpret microwave radiometric measurements at various frequencies under diverse conditions [Weinman and Guetter, 1977], [Wilheit et al., 1982], [Olson, 1987]. In addition to rain rate and frequency, the microwave brightness temperature also depends on the raindrop size distribution (DSD), ice above the rain, rain layer thickness, water vapor, ocean surface winds, and sea surface temperature. Therefore, algorithms to infer rainfall rates must include multifrequency data to account for other factors. Assumptions can sometimes be made about certain parameters based on existing conditions. In addition to multifrequency systems, dual polarization measurements provide information about the atmosphere because terrestrial emissivities tend to be highly polarized whereas atmospheric radiation is not. Thus, measured polarization differences distinguish the brightness temperature signature of the atmosphere from that of the Earth. Figure 4.18 demonstrates the effects of clouds, rain, clear air, and polarization by comparing two SSM/I images of a weather system over the south Atlantic. The first image, Figure 4.18(a), depicts the response of the SSM/I 85.5 GHz vertically polarized channel. Non-precipitating clouds appear the brightest; rain regions and clear air views of the ocean are both radiometrically colder. The precipitation regions appear isolated in Figure 4.18(b), which has undergone a polarization correction to distinguish the highly polarized ocean from the rain [Simpson, 1988].

For high frequency imagery, clouds can be divided into two broad categories by altitude and composition. The first category contains the high altitude cirrus clouds made of small ice crystals. These clouds are optically very thin at 90 GHz and below, thus making them virtually invisible. This property can be a significant advantage when observing storm systems, which often have a cirrus shield that prevents the use of IR and visible data for analyzing the underlying structure of the system. A microwave imager does not see the shield, so that the location of cumulonimbus and other thick clouds, rain cells, hail, graupel, dust, and convergent winds can be determined. The other species of ice or ice aggregates, such as hail and graupel, found in lower-to-mid-altitude clouds, the second category, appear somewhat like rain at the SSM/I frequencies, but scatter even more radiation.

Figures 4.19, 4.20, and 4.21 compare visual, 85 GHz, and 37 GHz microwave imagery, respectively, of Typhoon Sperry. Figure 4.19 shows the mature typhoon in visible light at local sunset time near the Philippines on 29 June 1987. Dense overlying cirrus clouds, at 50,000 feet, obscure the core of the storm, as well as thunderclouds outside the gale envelope, and the island of Mindanao (lower left), all of which are apparent in the microwave images of Figures 4.20 and 4.21. To the east (right) in the visual image, darkness obscures much of the lower atmosphere. The SSM/I senses the scene below 50,000 feet and produces detailed 85H and 37H microwave images of the eye and eyewall of the typhoon, Mindanao (white) in the southwest, and the band of thunderclouds streaming from the direction of Mindanao toward the southeastern flank of the typhoon. The color bars on the images cover the ranges 155 - 285 K and 150 - 280 K for the 85H and 37H images, respectively. The SSM/I images show the lower level clouds and windstreaming in the darkness to the east. In the upper right and left corners of the images in Figures 4.20 and 4.21, frontal lines separate the humid cyclonic air from the drier, high pressure regions through which the typhoon is passing. In the 85H image, the more brightly colored parts of the thunderclouds are deeply convective regions containing rain and hail. At 85 GHz, precipitation of this intensity induces scattering, thus making the area radiometrically cool. The darker outside regions indicate precipitation that is likely to be mostly rain. While the precipitation in the typhoon causes scattering at 85 GHz, absorption dominates in the 37 GHz causing brightness temperatures to increase with precipitation intensity. In the lower left corner of the images, a precipitation cell passes over Mindanao. The storm is visible in the 85H image, but the 37H response sees the land and not the storm cell. Differences in the responses such as these permit the identification of atmospheric, terrestrial, and ocean effects.

The second category of clouds includes cumulus, stratus, and their variational types, all composed primarily of water droplets. The total extinction by absorption and scattering of upwelling radiation from the land/ocean surface caused by these droplets increases with the thickness and water content of the cloud. The zenith attenuation at 90 GHz ranges from approximately 0.1dB for stratus clouds to approximately 1.5 dB for cumulus and greater than 5 dB for cumulus congestus clouds. Figure 4.22 demonstrates that the clouds of greatest optical thickness, such as cumulus congestus, are opaque to almost all radiation from the surface, whereas, for example, stratus clouds pass much of the radiation. The color bar covers 150 - 300 K, and the image has been enhanced for cloud signatures. The cloud-free tropical ocean is radiometrically colder than land (white) and provides a slowly-varying blue background. Land

has been saturated white so that the more significant clouds over land could be seen as a blue mottling against the brighter background and not be confused with land features. A cover of stratus and strato-cumulus clouds, identified as turquoise and purple over the ocean, is moving across the Baja Peninsula. Approximately 90% of the upwelling 85.5 GHz radiation from the surface is transmitted through these clouds, which almost completely blocks visual radiation. To the south, white cumulus clouds circulate around a tropical low preceding Hurricane Hilary (in 1987); the darker colors in the core identify deeply convective cumulonimbus clouds, the only clouds in the image that significantly attenuate microwave radiation.

The opacity of clouds increases with cloud liquid water content and microwave frequency, because absorption and scattering increase with frequency. Yet, under most circumstances, microwave imagers still penetrate the cloud cover. Consider the high frequency case of 85 GHz. Preliminary SSM/I observations of surface signals at 85.5 GHz suggest that clouds with cloud liquid water content greater than approximately  $0.4 - 0.5 \text{ kg/m}^2$  severely attenuate signals from below. Figure 4.23 depicts the distribution of clouds that are opaque to microwave, infrared, and visual radiation as a function of latitude for a week in October 1988. The 85H data used to produce Figure 4.24 were gridded and averaged over four degree sections in the same manner as the previously graphed visual and infrared data for comparison. The color bar for Fig. 4.24 ranges from 0 to  $1 \text{ kg/m}^2$  in units of 0.1. The purple regions correspond primarily with transmissive cumulus and cumulostratus clouds. The maximum values in the coverage plotted between latitudes 8 and 20 degrees were associated with the deeply convective regions of the Intertropical Convergence Zone (ITCZ). The coverage of clouds opaque to microwaves was less than 10% for these latitudes and nearly zero at higher latitudes where the atmosphere was nearly transparent all the time except for occasional thunderstorm activity. Because cloud attenuation decreases at lower frequencies, even fewer clouds block microwaves at 37 or 19 GHz. In contrast, clouds obscured the surface in visual images approximately 50% of the time at equatorial latitudes and covered progressively more surface more of the time toward higher latitudes. Also in contrast to the visual case, those clouds nearly opaque to microwaves were deeply convective storms and highly transient locally. Moreover, the microwave capability of sharply imaging these deeply convective clouds at higher resolutions provides opportunities to analyze important climatic processes associated with global circulation.

The global circulation system and hydrological cycle, and certain large-scale weather patterns, such as tropical storms and the El Nino-Southern Oscillation (ENSO), depend on small-scale convective processes in the atmosphere. These small-scale energy processes, on scales of a few hundred meters to a few kilometers, are not well resolved with current visual, infrared, and passive microwave remote sensors, such as AVHRR, OLS, GOES, and SSM/I. Water vapor, cloud liquid water, and rain typically tend toward maxima in the equatorial regions where solar heating is greatest. For example, two-thirds of global precipitation (global average 1 m) falls in the tropics and subtropics. The condensation of water vapor to cloud liquid water and rain releases heat inside the atmosphere, that forces global-scale motions in the troposphere. The nature of this heat release coupled with the resulting motions concentrates the tropical rainfall into a latitudinally thin region called the Intertropical Convergence Zone. At any given time within the ITCZ, rain may fall from roughly 30 individual cloud clusters, as in Figure 4.24,

each several hundred kilometers across [Simpson and Riehl, 1981]. Within these cloud clusters, the vertical energy transports and about 60 percent of the rainfall are further concentrated into approximately 2,000 towering cumulonimbus clouds called "hot towers," which carry high energy air up to the upper troposphere. This function is essential in driving the world-wide meridional circulation called the Hadley cell [Riehl and Simpson, 1979], [Jorgensen, 1984]. Field studies have shown that these towers contain updrafts ranging from about 5 to more than 30 m/s and can generate rainrates well above 100 mm/hr over areas 4 km by 4 km or smaller [Houze, 1982]. The remainder of the rain falls much more gradually, less than 10 mm/hr, from the large " anvils," or stratiform extrusions, from the hot towers. The number, size, and preferred location of these cloud clusters vary considerably, on time scales ranging from days to years or longer, so that the atmospheric heat engine has a variable output [Bjerknes, 1969], [Horel and Wallace, 1981], [Webster, 1981, 1982], [Lau and Chan, 1985, 1986, 1987], [Lorenc, 1984], [Weickman et al., 1985]. A large body of observational and modeling evidence implies that year-to-year variability of the latent heat released by the cloud clusters is a leading cause for short term global climate variations such as the El Nino-Southern Oscillation [Rasmussen, 1985]. Also, in certain favored locations, about one in 10 cloud clusters may deepen into a tropical cyclone [Simpson and Riehl, 1981], such as the one in Figure 4.20. The exact mechanisms of cyclogenesis for the tropical, and for the smaller arctic, cyclones are not known but are believed to be involved with the smaller-scale, 300 m or less, energy processes associated with these convective columns and their environment.

The discussion of clouds so far has pertained to their properties of radiative extinction. In addition to affecting the radiation from below, clouds are fairly good emitters. Like extinction, the emissivity of a cloud depends on its thickness and water content. The scattering of microwaves by water droplets, within thin non-precipitating clouds less than about 2 km vertical thickness, tends to brighten the cloud above background. Figure 4.25 shows model calculations at 94 GHz that demonstrate this effect [Tsang et al., 1977]. As the vertical thickness of the cloud increases beyond about 2 km however, the attenuation by absorption begins to dominate, and the cloud begins to darken relative to background. Non-precipitating clouds, therefore, can have a range of emissivities less than or equal to 0.9. As the cloud begins to precipitate, the attenuation of microwave transmission increases dramatically from approximately 1.0 dB at 0.5 mm/hr to, for example 6 dB at 10 mm/hr and 10 dB at 20 mm/hr. As hail, graupel, and other opaque scattering material combine with the precipitating cloud in storm systems, the attenuation can decrease the emissivity of the cloud to 0.2 or less, depending on the type of atmospheric feature. The microwave signal, therefore, indicates the thickness or type of cloud; the pattern of emissivities of the cloud, and of local water vapor structure and windstreaming, all observed in the same image, indicates the type of atmospheric feature. For example, fronts are delineated by a line of high contrast in emissivity, usually enhanced by a wave of increased water vapor content, as in Figure 4.2. Squall lines are fronts accompanied by increased windspeed and frequently followed immediately by deep convective clouds, as seen over Florida in Figure 4.2. Squall lines, tornadoes, and tropical storms are sites of damaging convergent winds. Note the convergence of the windstreams in the upper right of Figure 4.20. These features are complex on scales smaller than the resolution of the SSM/I; radiometers with higher resolution can precisely locate and track such features. Upper atmospheric disturbances, such as atmospheric

jets involved with cyclogenesis may be identified, as well as local turbulence with dimensions approaching 100 meters, as found near airports. Oceanic turbulence could be studied over large areas with 40 - 160 times the resolution presently available. In addition to studies of free convective motions, high resolution passive microwave data could improve analysis of forced convective motions, such as orographic lifting, frontal lifting, gravity-wave, displacements, and vertical motion induced by horizontal convergence of wind fields.

#### 4.4.2 Aerosols and Particulates

Convective overturning to create clouds is not restricted to natural causes. Man-made features generate non-uniform local heating, such as induced thermals over parking lots or plowed fields, along highway systems, or in a city's heat-island circulations. Analysis of these effects requires observations on scales of hundreds of meters. Industrial smokestacks, including those of ships, create clouds of pollutant aerosols and atmospheric wakes on scales of 100 m to about 10 km. Figure 4.26 shows a visual example of the atmospheric wakes, at 1 km resolution, with anomalous cloud lines produced by ships. The capability to detect and track atmospheric wakes on smaller scales has obvious importance in both naval surveillance and in studies of the effects of man-made aerosols on atmospheric integrity and climate. The baseline-system resolution of 100 - 400 m from 19 to 90 GHz closely matches the narrow dimension of the ship's atmospheric wakes which grow from less than 1 km at formation to more than 10 km before they dissipate. Thus, the baseline system should be able to detect contrasts greater than a few Kelvin.

The precise physics of anomalous cloud lines is not clear, and the frequency of occurrence remains unknown. Increased understanding of this phenomenon requires smaller scale observations. Current observations suggest that anomalous cloud lines occur when vessels move under a relatively calm atmosphere enabling microscopic particles from the ship's exhaust stacks to rise into the middle atmosphere. The particles become nuclei around which water vapor condenses. Although the condensation occurs regardless of winds, calm air preserves the trail long enough to give the impression of an ocean with numerous ships. The particles absorb sunlight and add to atmospheric heating, while the droplets that form around the particles reflect sunlight back into space. The result may significantly affect the long term global energy balance.

Volcanoes produce atmospheric particles that affect the climate. Figures 4.27 and 4.28 present a GMS visual image of the eruption of Volcano Pinatubo during a typhoon and the corresponding SSM/I 85H microwave image, respectively. The two images show different patterns of the eruptive plume at different levels of the atmosphere. The deep blue pattern at the center of cross-hairs in Figure 4.28 identifies the larger ejecta within the dust plume seen in Figure 4.27. Multi-sensory imagery will enable models to be tested for the presence of volcanic matter and its contribution to various atmospheric levels. In addition, the microwave imagery penetrates the upper levels of smaller-sized volcanic ash, as well as clouds, which are opaque to visible and IR radiation. Backscattering by larger, hail-sized particles probably causes the attenuation of microwave radiation at lower levels in the volcano.

Naturally occurring dust storms also generate atmospheric particulates, as shown in the OLS visual image in Figure 4.29. In this case, the particle size ranges from 50 to 100 microns, about the same as hydrometeors in light rain. The 85.5 GHz image in Figure 4.30 indicates that the dust begins scattering measurably at this frequency, but not enough to significantly degrade the microwave view through the dust. Technology-based studies have shown that dust capable of severely attenuating near-IR and optical links does not significantly attenuate microwaves near 90 GHz [Bauer et al., 1977]. The microwave image of the dusty atmosphere near the West African coast in Figure 4.30 is colored turquoise; land has been saturated white. This SSM/I overpass follows the one for Figure 4.4 by about 12 hours.

A third example of atmospheric particulates is the oil fires in the Persian Gulf War. Figure 4.31 shows a visual image of the scene when atmospheric contamination by smoke made the atmosphere nearly opaque at optical and IR wavelengths. The corresponding 85.5 GHz image of the same scene, shown in Figure 4.32, indicates that microwave radiation at or below 90 GHz can penetrate dense smoke of this kind.

#### 4.5 Operation Desert Storm

The Pentagon received daily SSM/I briefings from NPOC and AFGWC during Operation Desert Storm, and DMSP SSM/I and OLS imagery were dispatched regularly to the Middle East operations area. Figure 4.33 illustrates one contribution that SSM/I microwave imagery provided in the Operation Desert Storm. The first three images in the mosaic, generated by the AFGWC, show the kind of imagery that was used in operations planning, and the fourth image is an example of what could have happened if SSM/I imagery were not used. A final report by the SSM/I SPO indicated that the use of SSM/I and OLS imagery shortened the final phase of the war by about 10%. The upper left image in Figure 4.33 is infrared data from the OLS sensor on the DMSP-F8. This image shows the kind and extent of cloud cover over the area. The lower left image is SSM/I 85.5 GHz data from the F-8 satellite and indicates intensely convective regions where rain and possibly high wind could be expected. The upper right image is a combination of channels of the SSM/I suitable for depicting the signal of conditions for thunderstorm activity and the areas of heavy ground water, or mud, resulting from heavy rains.

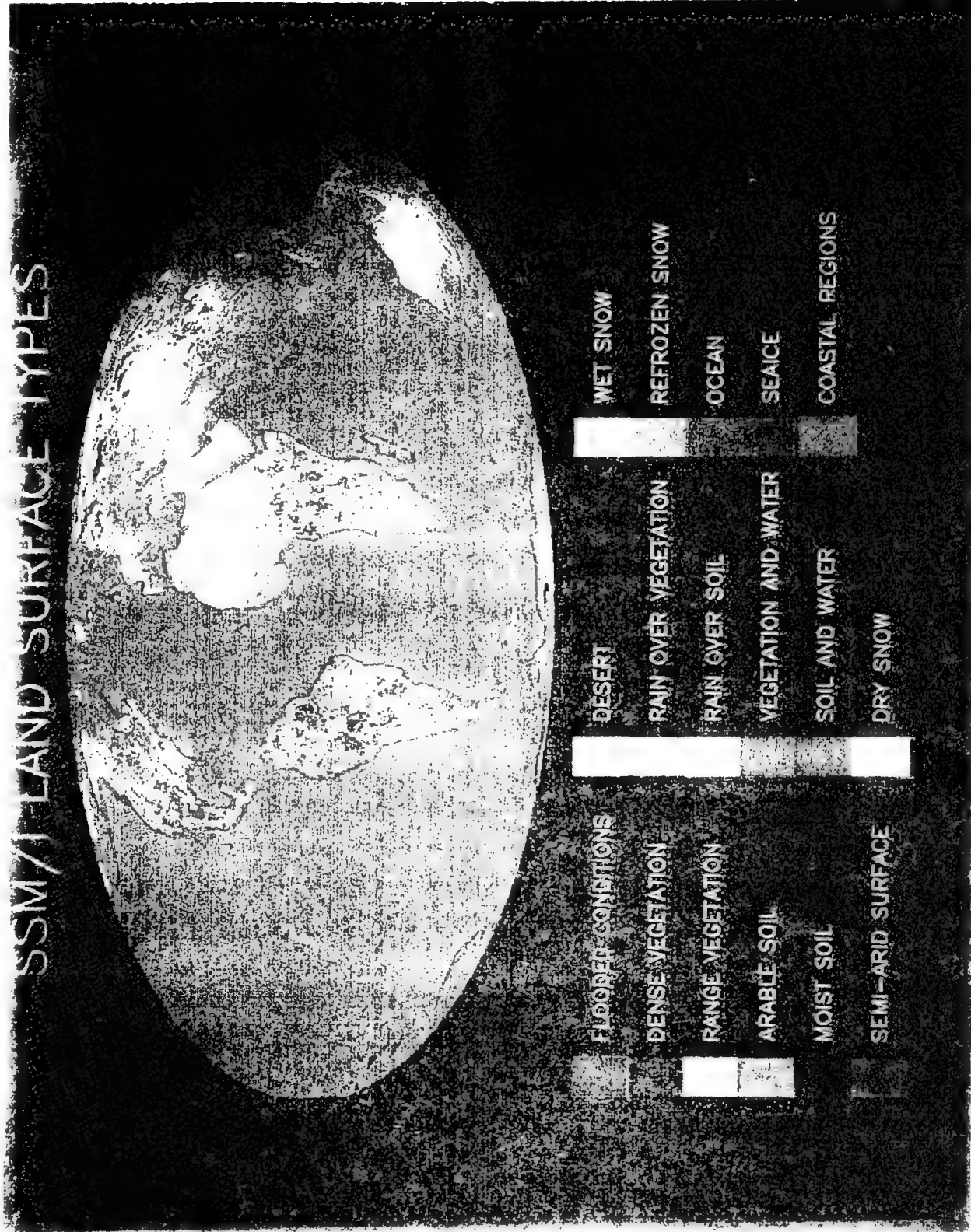


Figure 4.1 SSM/I image of land surface types with 12.5 km resolution.



Figure 4.2 SSM/I 85H image of the southeastern United States showing high soil moisture in the Mississippi Valley and precipitation band over Florida and the Gulf of Mexico.

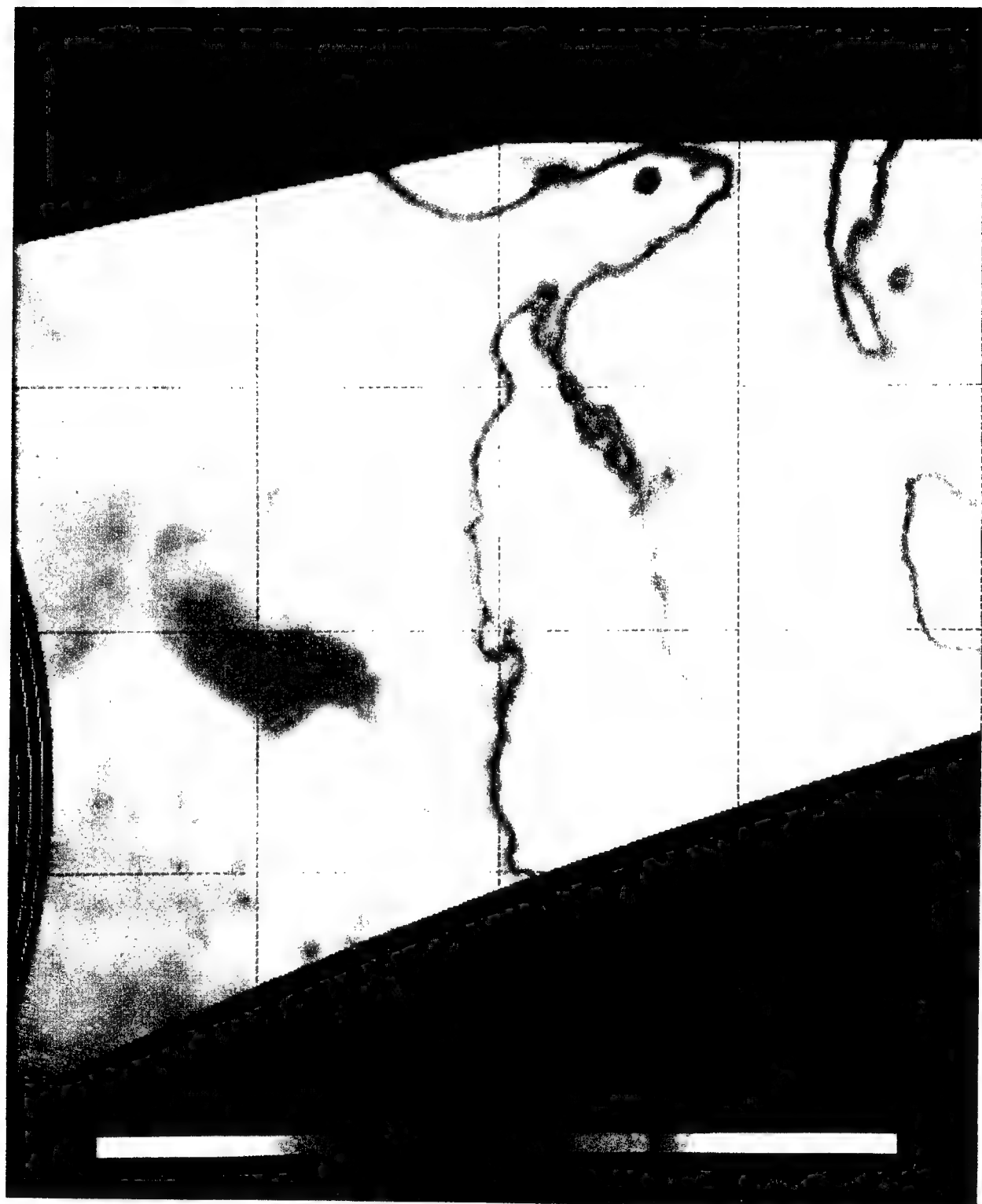


Figure 4.3 SSM/I 37H image of the southeastern United States showing high soil moisture in the Mississippi Valley and precipitation band over Florida and the Gulf of Mexico.



Figure 4.4 SSM/I 85H image of soil and vegetation types over northwest Africa.

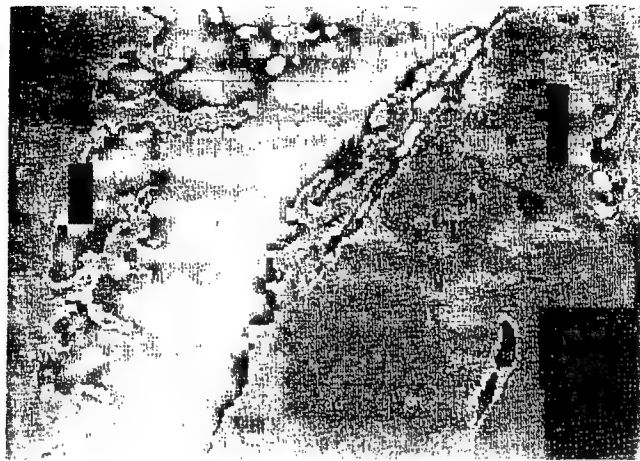


Figure 4.5 ESTAR image of the Delmarva peninsula in Virginia showing marshy areas in green. Resolution is on the order of 350 m [LeVine et al., 1990].



Figure 4.6 SSM/I 85H image of snow in the midwestern United States.

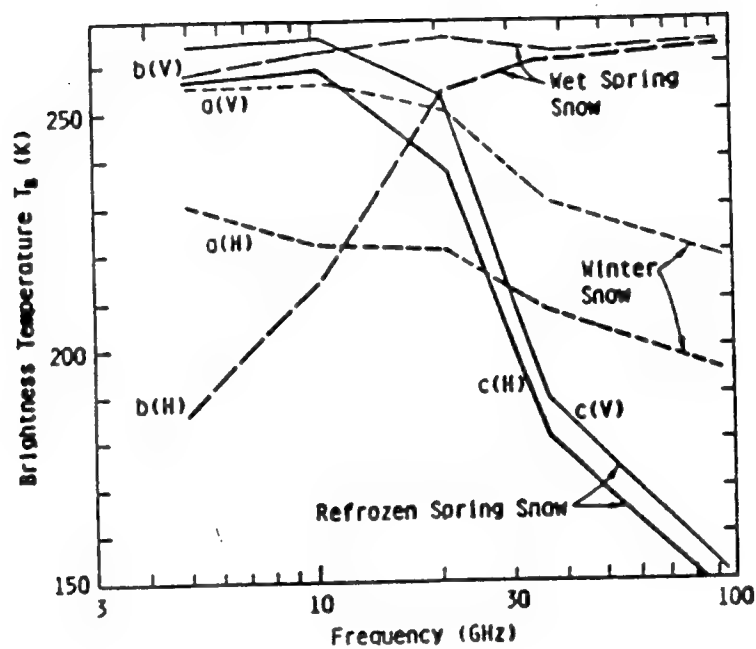


Figure 4.7 Average spectral brightness temperatures of three different snow types observed with vertical and horizontal polarization. The incidence angle is 50 degrees and the snow depths have been normalized to 48 cm water equivalent [Schanda et al., 1983].

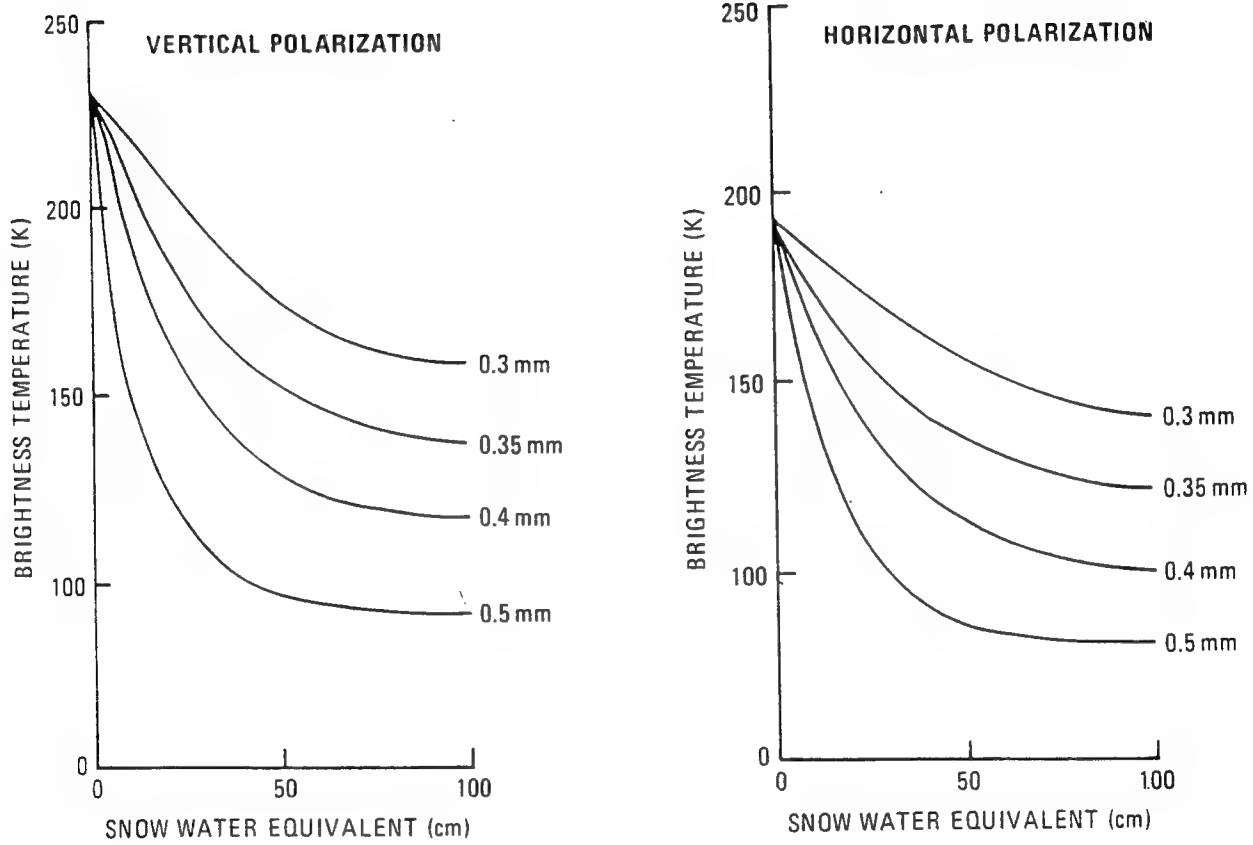


Figure 4.8 Theoretical 37 GHz brightness temperature versus snow water equivalent of dry snow over frozen soil at 50 degree incidence [Murphy, 1987].

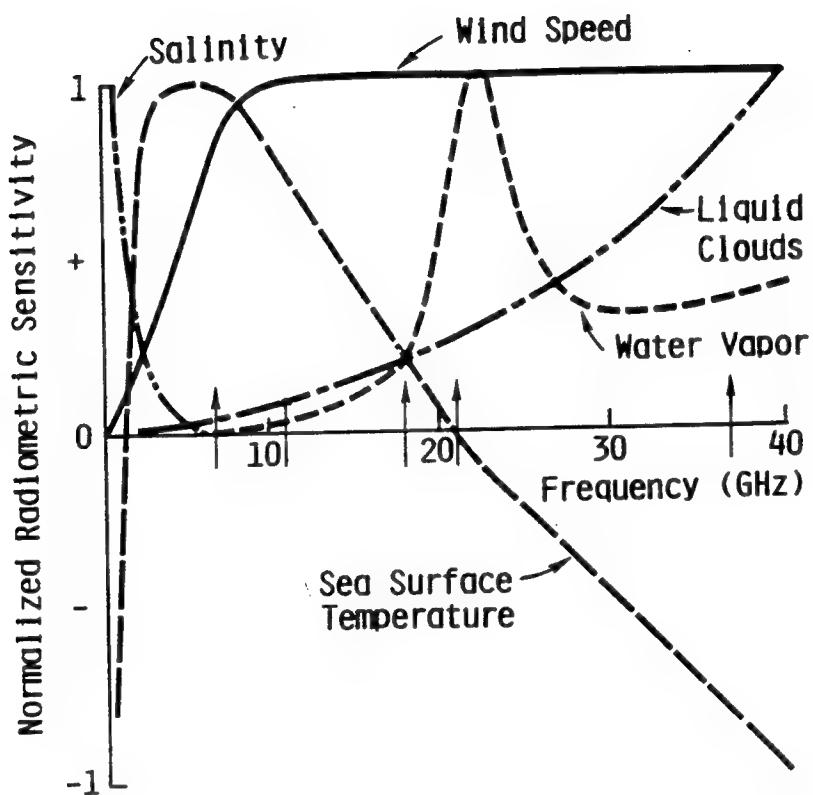


Figure 4.9 Spectra of normalized radiometric sensitivity for various geophysical parameters [Wilheit et al., 1980].

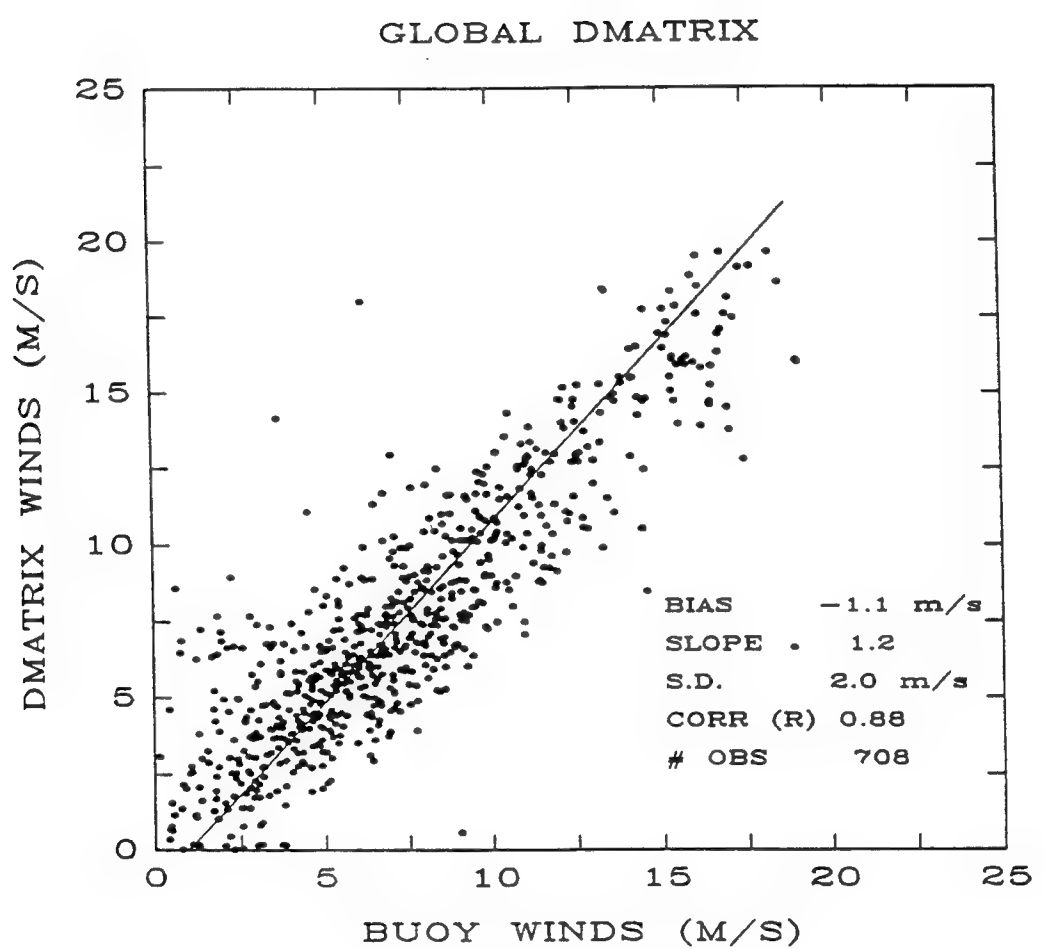


Figure 4.10 Comparison of the SSM/I global wind speeds with buoy winds.

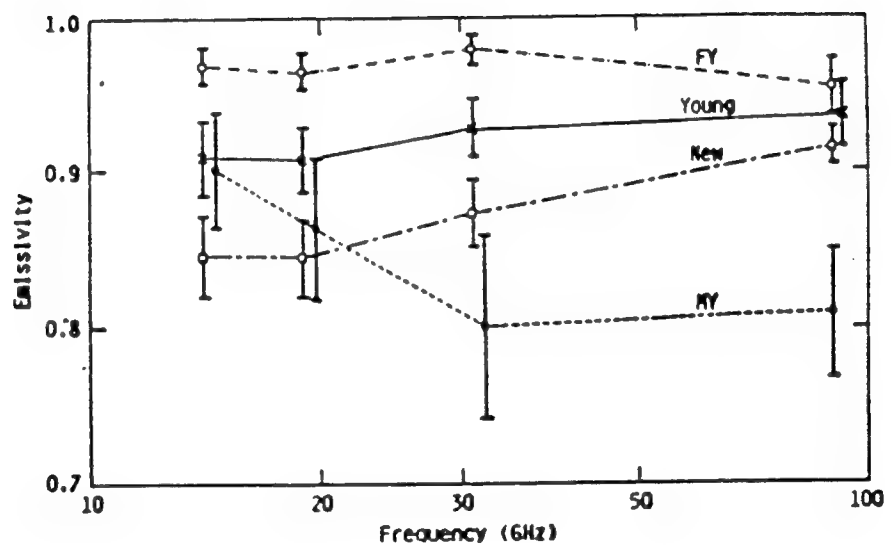


Figure 4.11 Nadir emissivity of four ice types [Troy et al., 1981].

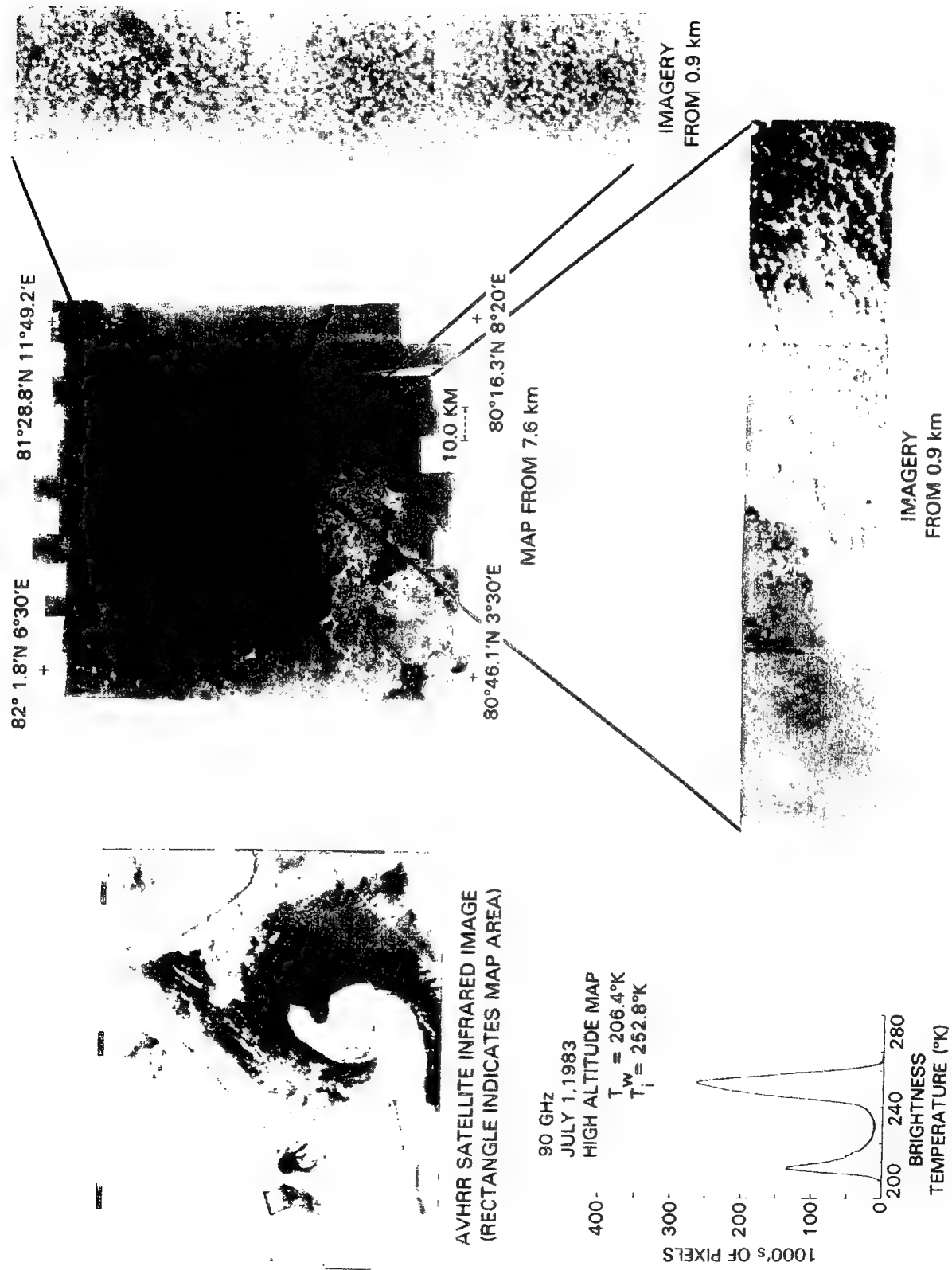


Figure 4.12 90 GHz image of Arctic sea ice.

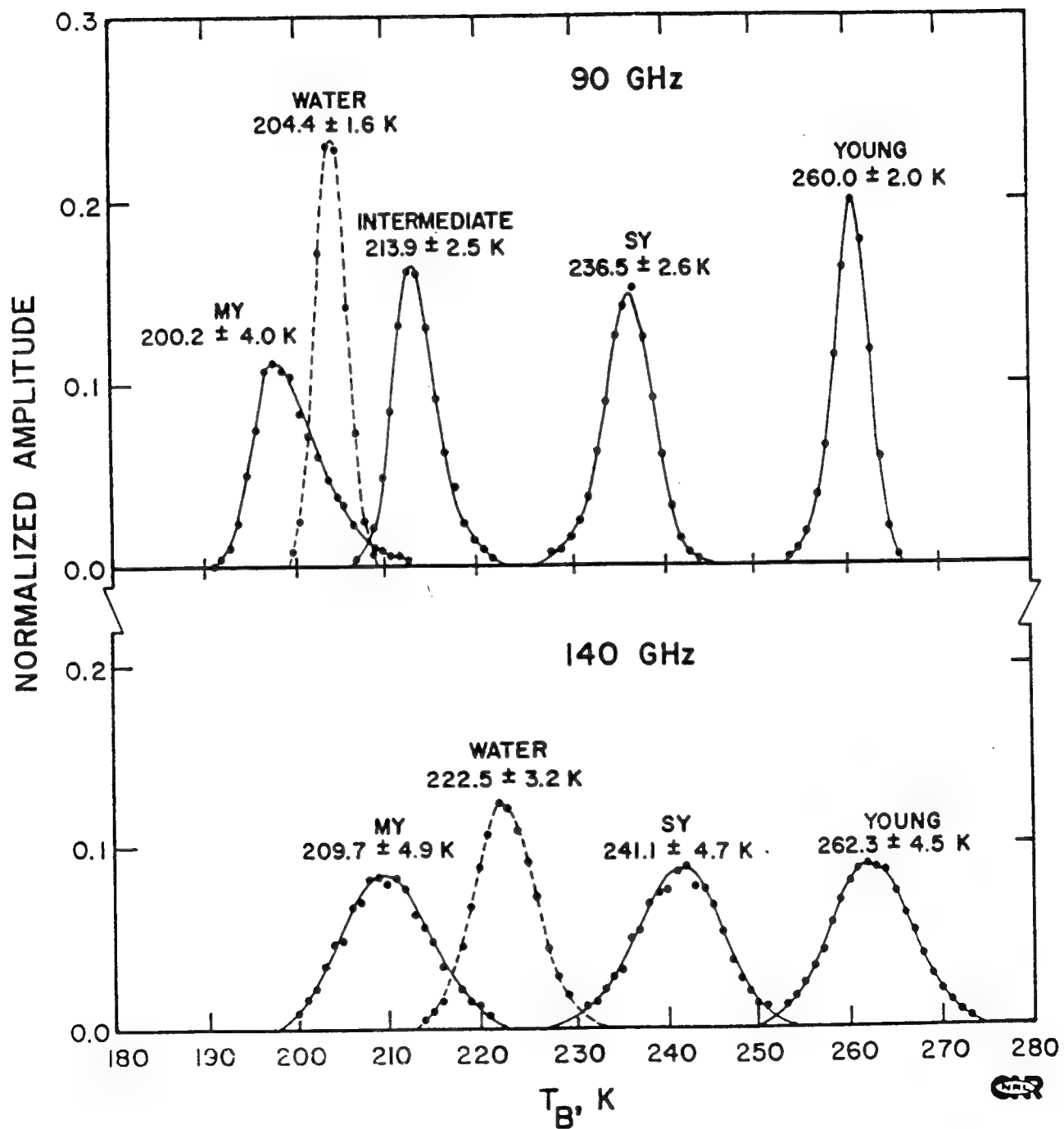


Figure 4.13 Sea ice brightness temperature distribution at 90 GHz and 140 GHz.

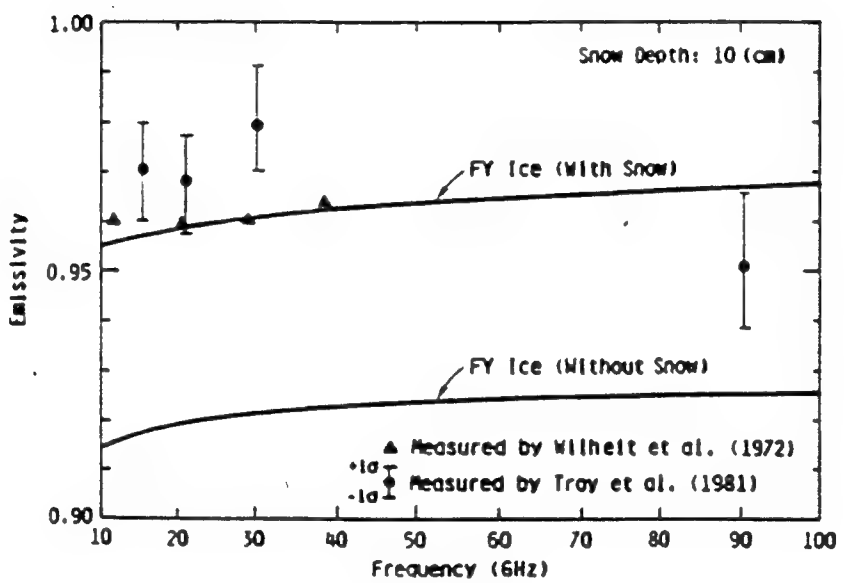


Figure 4.14 Variation of emissivity of first year sea ice with and without snow cover [Ulaby et al., 1986].

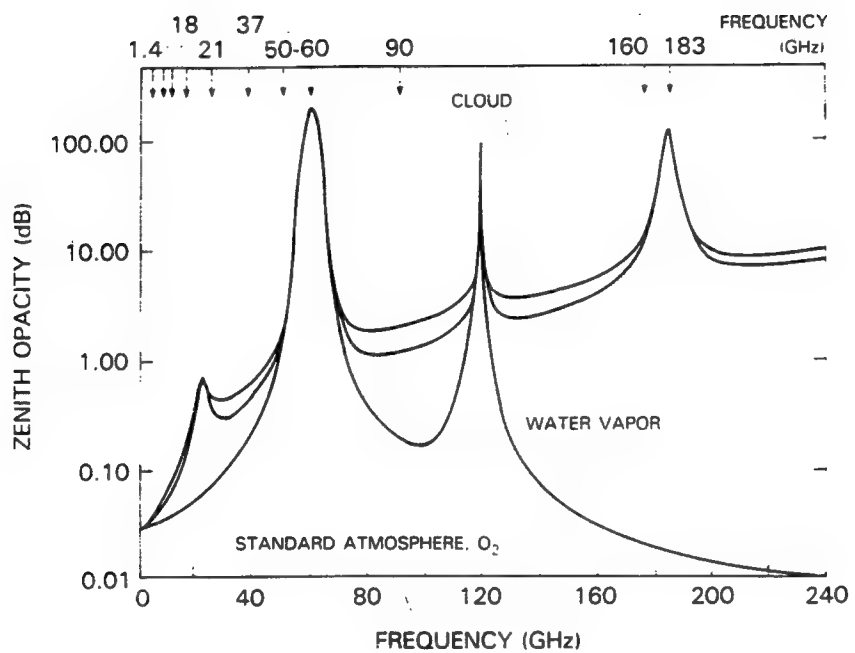


Figure 4.15 Atmospheric microwave absorption as a function of frequency for three atmospheres.

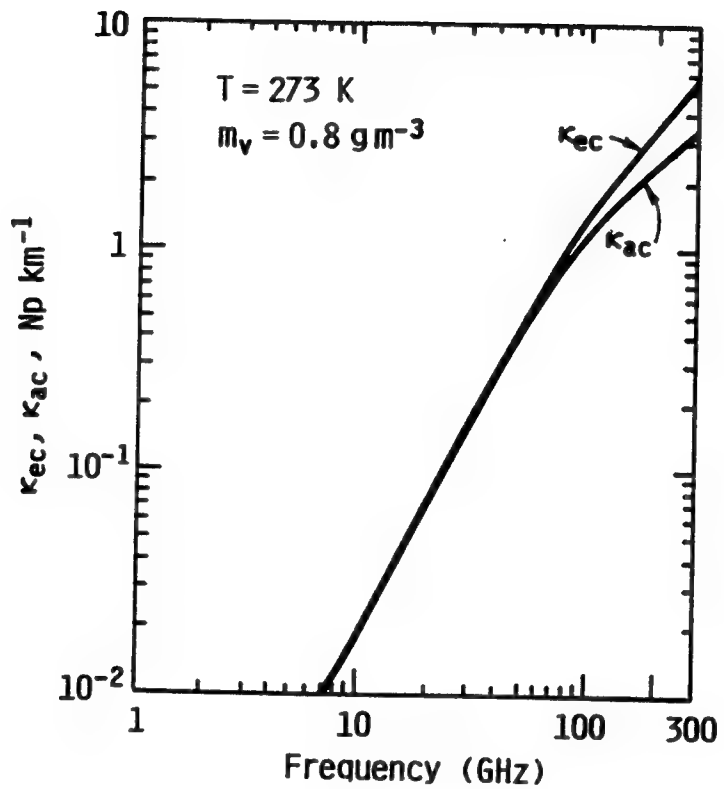


Figure 4.16 Calculated Mie absorption and extinction coefficients of a cloud;  $m_v$  is the cloud water content [Tsang et al., 1977].

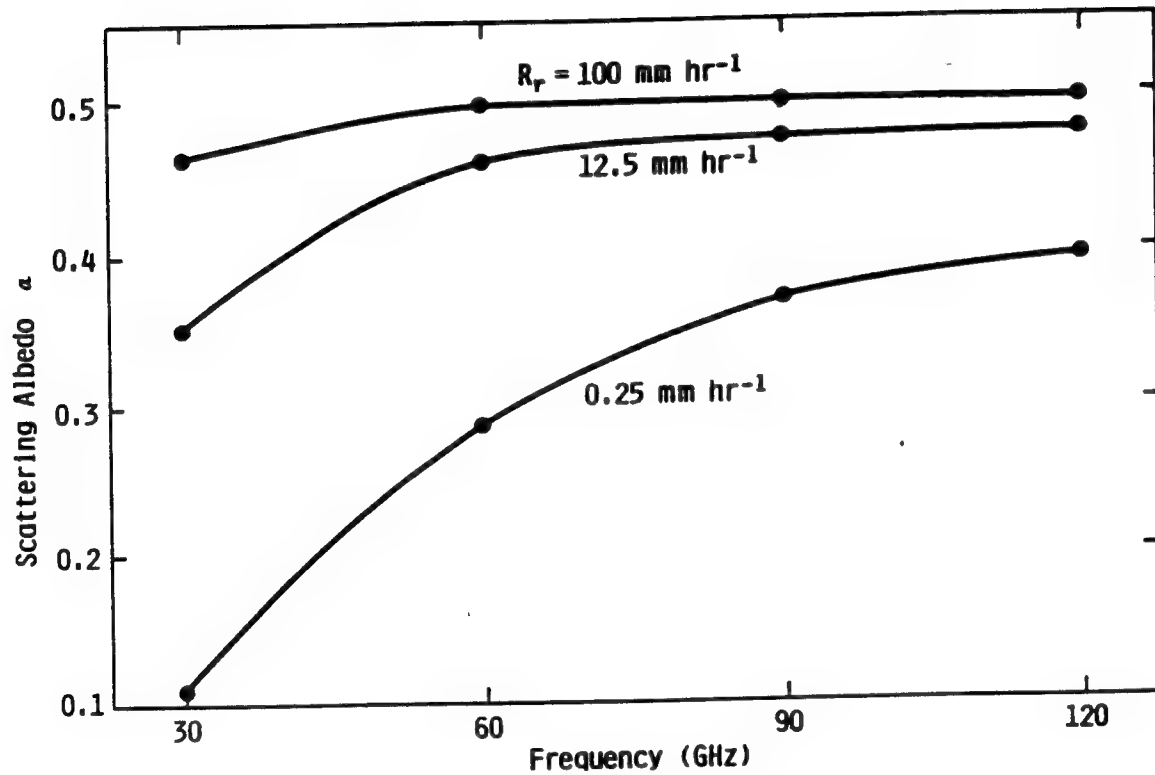


Figure 4.17 Variation of the Mie scattering albedo (ratio of scattering to total extinction) for three rain rates [Ulaby et al., 1986].

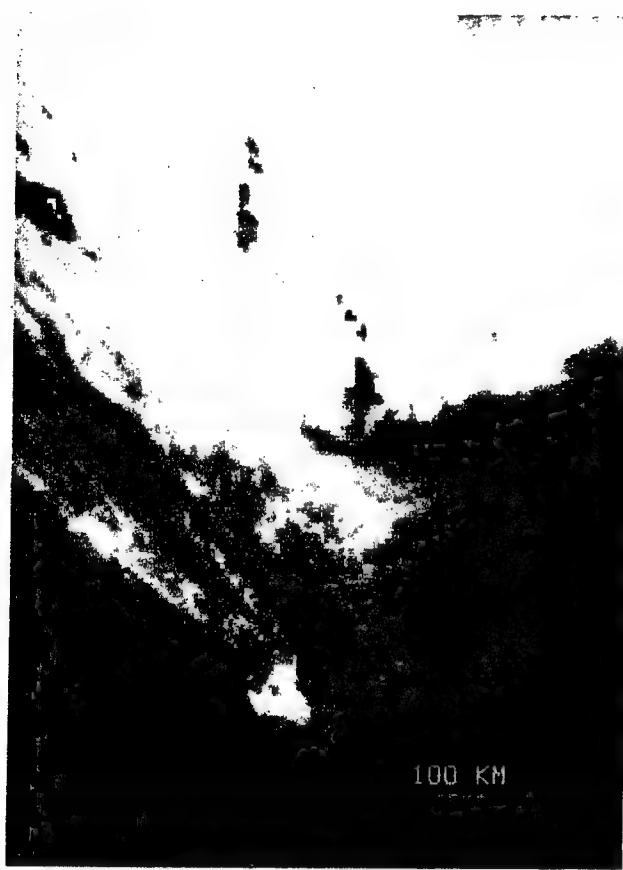


Figure 4.18 (a) SSM/I vertically polarized brightness temperature of a weather disturbance over the Atlantic ocean. Brightness temperatures range from 180 K to 270 K. (b) Polarization corrected image of the same scene in which dark regions represent probable precipitation [Simpson, 1988].



Figure 4.19 OLS visual image of Typhoon Sperry.

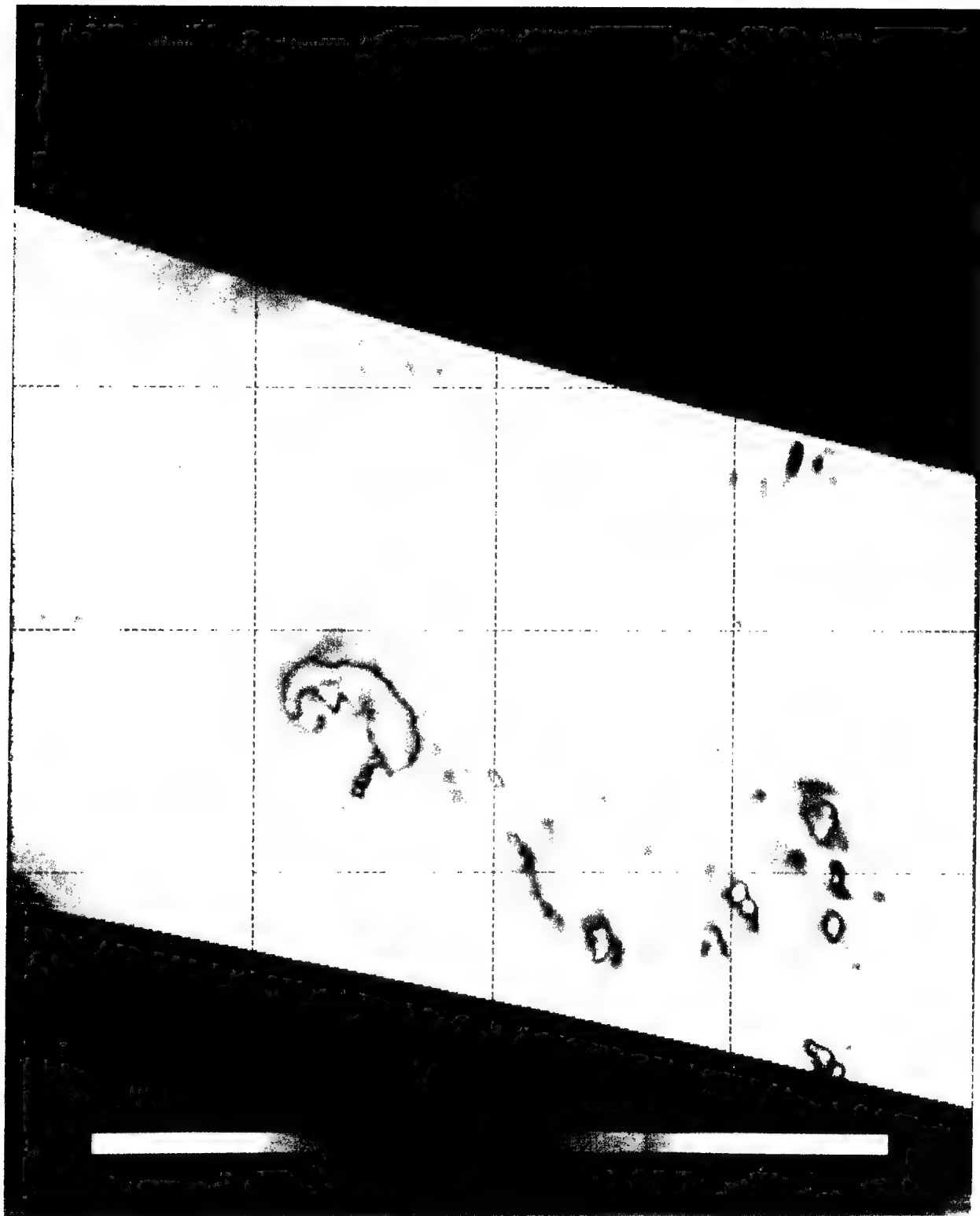


Figure 4.20 SSM/I 85H image of Typhoon Sperry. The vertical dimension ranges from 5°N to 25°N latitude.

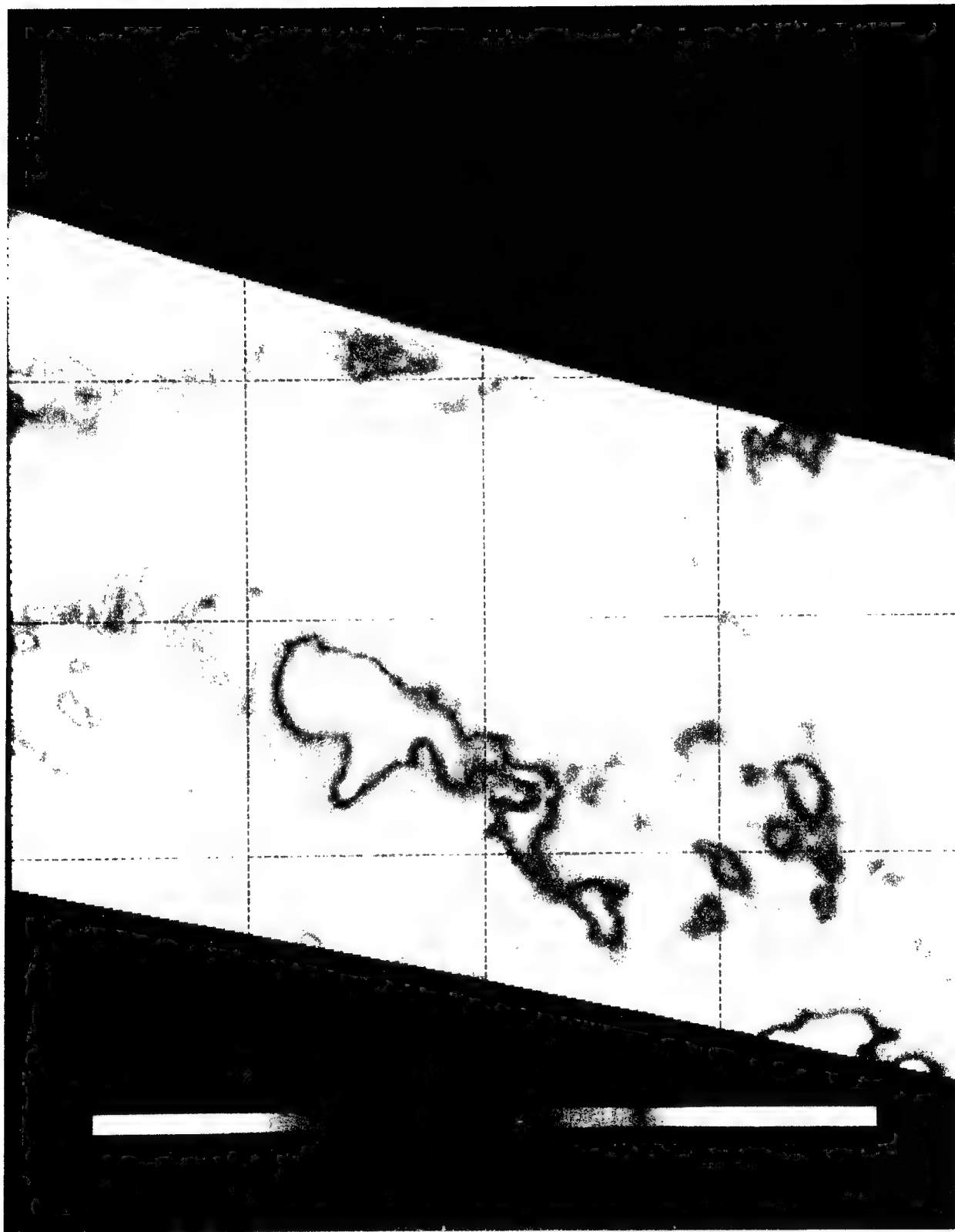


Figure 4.21 SSM/I 37H image of Typhoon Sperry.



Figure 4.22 SSM/I image of clouds over the eastern Pacific Ocean.

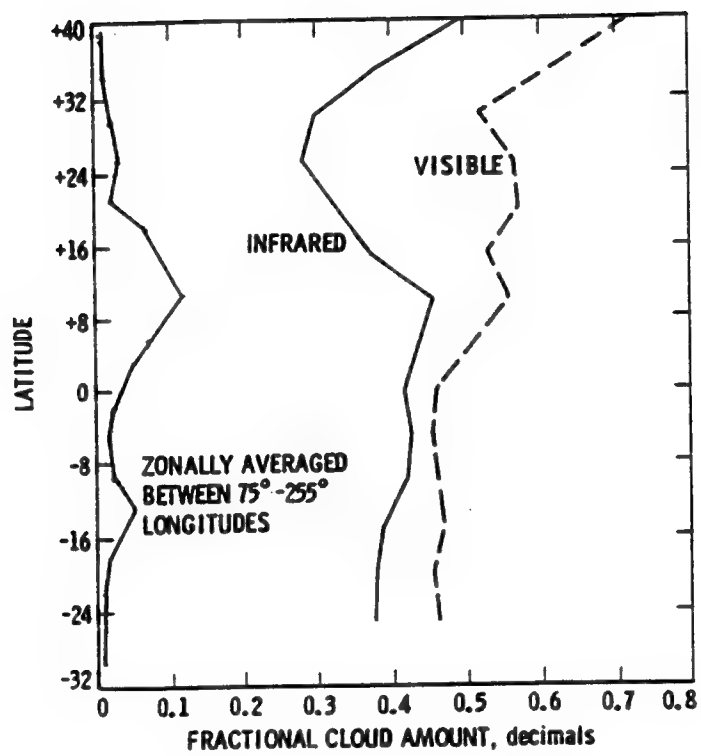


Figure 4.23 Latitudinal coverage of clouds observed with SSM/I.



Figure 4.24 Global SSM/I image of cloud liquid water.

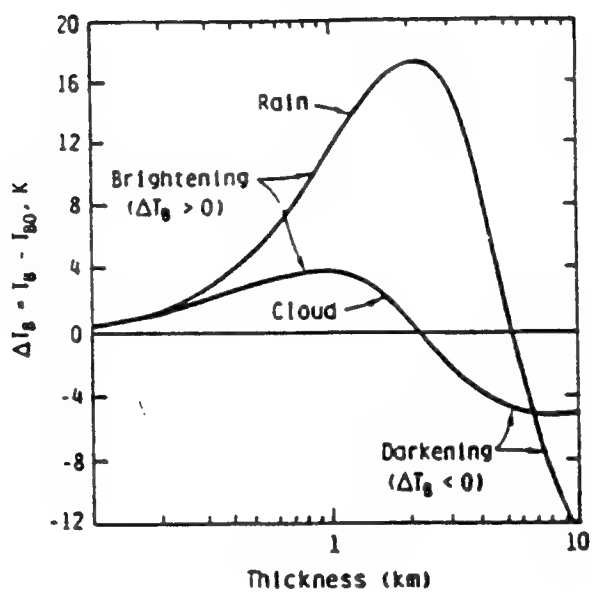


Figure 4.25 Effects of clouds and rain on brightness temperature as a function of layer thickness.



GTL 3 254:17:21 05062 1 018 NO HWS 045E 083E97

Figure 4.26 AVHRR visual image of atmospheric ship wakes.

1991-05-15 0734Z



Figure 4.27 GMS visual image of Mount Pinatubo volcano.



Figure 4.28 SSM/I 85H image of Mount Pinatubo volcano.

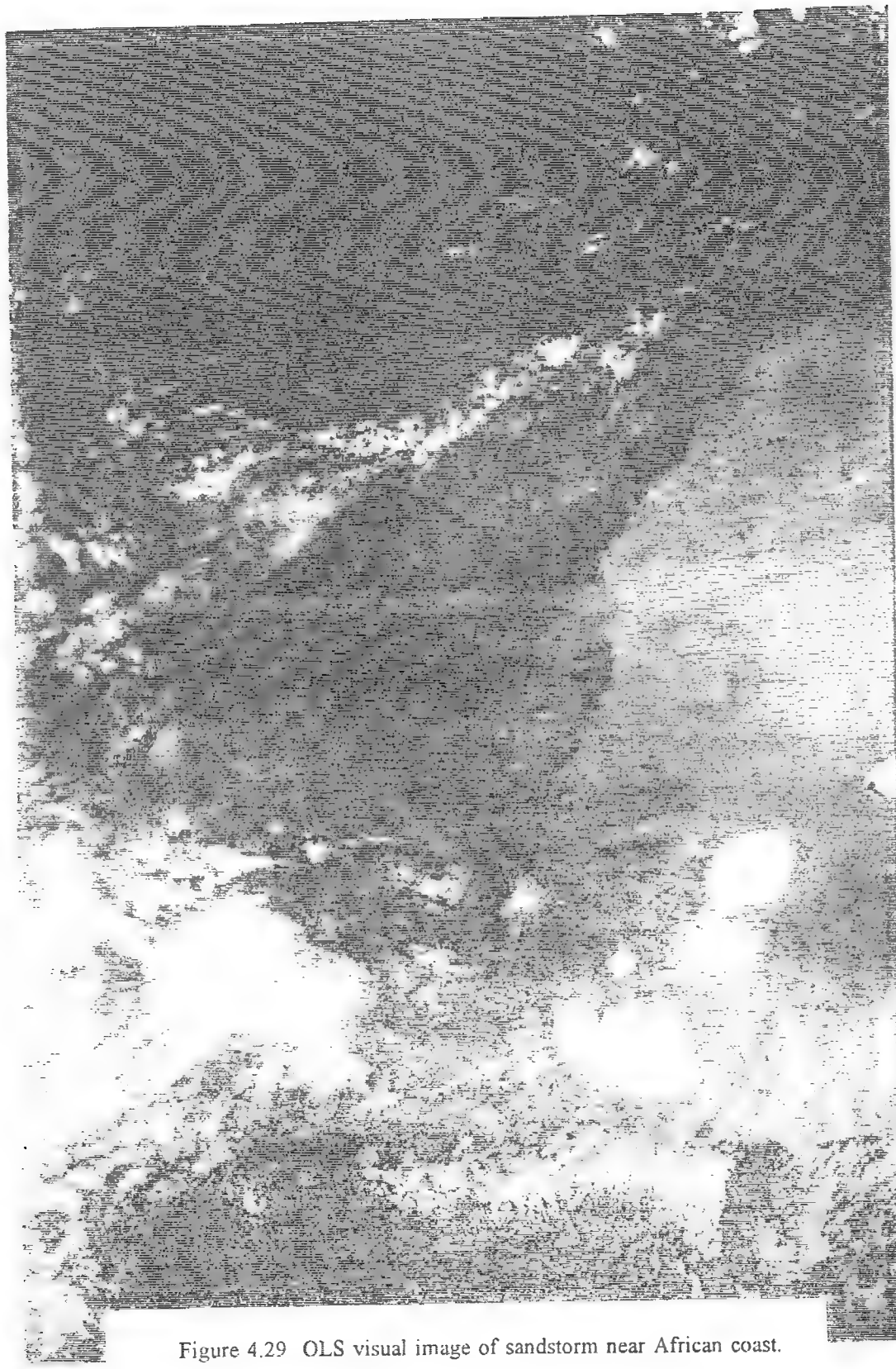


Figure 4.29 OLS visual image of sandstorm near African coast.



Figure 4.30 SSM/I 85H image of sandstorm near African coast.

F 1 1991:076 10:51:25 127E2 11A 70N-95E 145

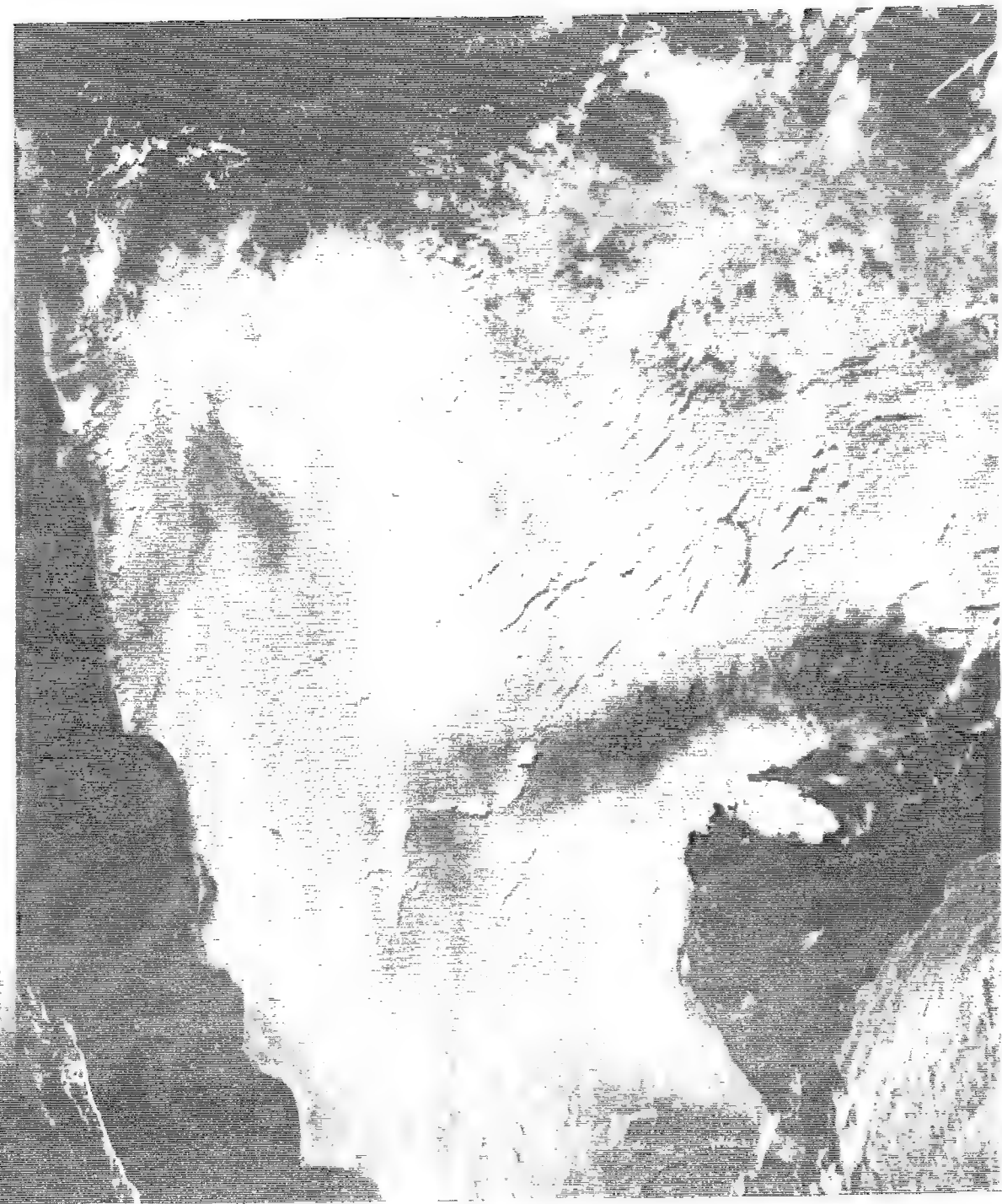


Figure 4.31 AVHRR visual image of smoke over Kuwait from oil well fires.



Figure 4.32 SSM/I 85H image of Kuwait coincident with image in Figure 4.32.

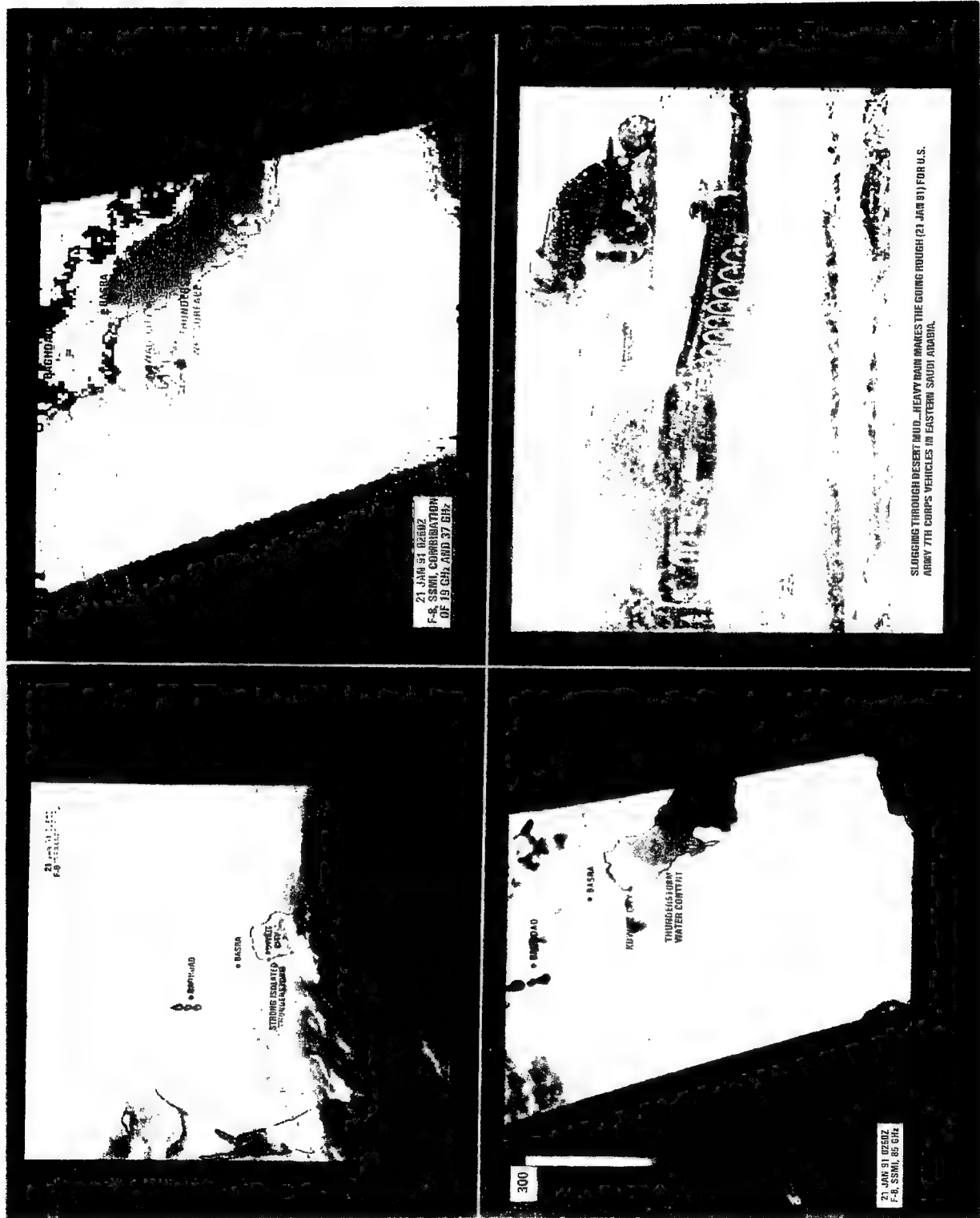


Figure 4.33 DMSP images from Operation Desert Storm.

## 5.0 TARGET/BACKGROUND CHARACTERISTICS

### 5.1 Millimeter Wave Image Characteristics

Figures 5.1 through 5.3 provide examples of scene brightness temperature contrast from passive millimeter wave data. All three images were obtained from a 90 GHz airborne radiometer using a single scanned beam. The surface resolution is about 15 m and, with one exception, the false color code for all of the images begins with blue (coldest) progressing through green, yellow, and orange, to red (warmest). In Figure 5.2, the exception, the coldest temperatures, such as those resulting from oil tanks and the docked ships, correspond to pink. In general, metal surfaces at millimeter wavelengths appear radiometrically coldest, with water at intermediate brightness temperatures and turbulent white water and terrain warmest. Note that this is the apparent millimeter wavelength radiative temperature and not the physical temperature of the material. Accompanying each image is coincident photography. The image in Figure 5.1 of Portsmouth, Virginia, shows highways, buildings, and open areas in the city. The brightness temperatures,  $T_B$ , range from 186 to 288 K. Notice the cloverleaf intersection to the left of center in the image. The dots on the road leading up out of the interchange are trucks. The image of the docks at Norfolk, Virginia, in Figure 5.2, shows docked ships, oil storage tanks, buildings, parked cars, and grassy areas on the docks. Here the brightness temperatures range from 168 to 279 K. The two aircraft carriers at the extreme right are distinguishable in the image by their shape. Also note that the island superstructure of the aircraft carriers is recognizable. The images of Virginia farmland in Figure 5.3 show identical areas for both spring (April 1980,  $T_B$  = 180-295 K) and winter (January 1981,  $T_B$  = 189-277 K). For this set of images, purple represents brightness temperatures between those represented by blue and green. Ice on the lake at the left of the winter image appears purple, while in spring, swampy areas there correspond to purple. Furthermore, emissions from the farm fields are similar to the surrounding forest in the spring (both are reds and yellows). However, during the winter, the open farm fields appear colder (green) than the surrounding areas (red). In general, the 90 GHz images closely resemble the detail and form of the visual image, thus making the millimeter wave imagery easy to interpret, even by relatively untrained observers.

### 5.2 Clutter

#### 5.2.1 Surface Clutter

Variations in the reflectivity, emissivity, scattering, and absorption of the surface and atmosphere constitute a clutter background against which targets must be identified. Figures 5.1, 5.2, and 5.3 demonstrate clearly the wide range of size, shape, and contrast of land features. Figures 5.4, 5.5, and 5.6 present examples of background clutter spectra for farmland, sea ice, and docks. Note the similarity of the shape of the spectra and that the power is greatest at the lower spatial frequencies. A target with dimensions of 100 meters or smaller has spectral power primarily at spatial frequencies of 10 Hz/Km or higher where the background clutter is relatively small. This provides a means to suppress the clutter by matching the spatial frequency response

of the receiving system to that of the target and rejecting the lower spatial frequencies of the background clutter.

The ocean presents a more uniform background than land but clutter is generated primarily by breaking waves and atmospheric variations such as clouds, rain cells, and water vapor density variations. In order to detect targets near or at the limits set by the receiver sensitivity, the background clutter must be suppressed. To do this the characteristics of the receiver must be matched to some property which is unique to the target and is not present or is present to a lesser degree in the background. This property may be the size and shape of the target, the amplitude, polarization or frequency spectrum of its radiation, or the time variation of any of these. If the target is moving relative to the background, the clutter may be suppressed by using an array of beams. This technique relies upon the repeated differencing of the signals from successive beams as they sweep over the scene. Those features which change very slowly compared to the time delay between beams, such as spatial clutter, will be removed whereas a target which has moved relative to the background in the time between successive measurements will present a signal. Using this technique, clutter rejection of as much as 23 dB has been obtained at 10 GHz with an aircraft real multiple-beam system at the Naval Research Laboratory. Figure 5.7 shows an example of these results. The unshifted output from two of the beams, one of which trails the other by two beamwidths appears at the top of the figure. The result of subtracting the signal from the first beam, appropriately delayed, from the signal from the trailing beam is shown in the middle of the figure. The clutter has been reduced by over an order of magnitude and the target signal is apparent. The horizontal "S" shaped response to the target results from subtracting the signals from the two beams. Aircraft pitch, roll, and yaw motions and slight differences in the shape of the two antenna beams produce the large spurious deflections. The signal after correcting for these effects appears at the bottom of Figure 5.7. The target signal is now clearly visible and the remaining noise is almost entirely due to instrument noise.

### 5.2.2 Atmospheric Temporal Variations

Atmospheric variations in temperature, pressure, and humidity cause fluctuations in the millimeter wave radiation received from the atmosphere and from background scenes. In addition to the limits imposed by instrumental noise and surface clutter described above, these fluctuations in the emission and absorption of the atmosphere, place limits on the ability of a passive millimeter wave radiometer to detect targets in a noisy environment. Figure 5.8 presents upward viewing measurements of the sky at 37 GHz for three groups of atmospheric conditions ranging from clear, group 1, to intermediate light clouds, group 2, to heavy clouds, group 3. Note that the power spectrum shown at the top of the figure, while relatively flat for clear sky, shows increasing energy at low frequencies up to about 0.1 Hz (10 second period) with increasing atmospheric congestion. The temporal structure function  $D(\tau)$  characterizes a non-stationary random process, such as atmospheric turbulence, by taking the rms difference between the time dependent function and itself at a later time. It is given by

$$D(\tau) = [f(t+\tau) - f(t)]^2$$

where  $\tau$  represents the time delay. The temporal structure function,  $R(\tau)$ , provides a means of removing the instrument noise to obtain the true contribution of the sky. It is given by

$$R(\tau) = \text{sqrt} \{ (D_s(\tau) - D_i(\tau)) / D_i(\tau) \}$$

where  $D_s$  and  $D_i$  are the temporal structure functions of the scene and instrument. When  $R$  is greater than unity, the temporal clutter of the sky exceeds that of the instrument. In particular, the value of  $\tau$  for which  $R = 1$  represents the approximate maximum useful integration or sample time for the scene. As can be seen in the lower half of Figure 5.8, this may be as short as a few seconds for heavy clouds. Figure 5.9 demonstrates this further by presenting the rms of the measured signal as a function of integration time. Note that for heavy atmospheric clutter, the rms signal actually increases for integration times greater than about a second or so. In conclusion, sky temporal clutter may dominate system noise for integration times greater than a few seconds. Longer integration times may not be effective in increasing signal-to-noise ratio since increasing the integration time will not necessarily reduce sky clutter noise. Therefore, there is a limit to the reduction of the minimum detectable signal obtained by increasing the integration time and additional improvements in sensitivity must be achieved by other means. The non-stationary nature of temporal variations of atmospheric emission does not preclude the possibility of clutter suppression, but a detailed knowledge of the spatial and temporal clutter of the atmosphere and of background scenes is needed so that matched filtering in both the spatial and temporal domains can be used to increase the signal-to-clutter ratio.

### 5.3 Military Targets

#### 5.3.1 Aircraft, Tanks and Vehicles

Military targets are generally made of metal, and metal, even when painted, appears as a mirror to millimeter and microwave wavelength radiation, reflecting radiation while radiating little due to its own physical temperature. The capability to detect these targets usually depends on the contrast between the reflectivity of the metal targets and the natural backgrounds, which generally have low reflectivities. The signal from a metal object depends on the orientation of the surface and radiation sources in the reflected field of view. In most cases for space surveillance systems, the surface viewed is parallel or nearly parallel with the Earth's surface and will reflect only radiation from the atmosphere and space. This configuration causes the metal surfaces to appear much colder than the surrounding surface. Figure 5.10 shows a calculated spectral response of a satellite-borne sensor looking through a cloud-free, standard atmosphere [Weiler et al., 1986]. The curves represent the brightness temperature difference between a reflecting target and backgrounds of land and water. The target contrast is the difference between the target brightness and the natural target. Note that the oxygen complex from 50-70 GHz completely obscures all three scenes. It should be noted that a non-reflective coating can be applied to the metal to give it a high emissivity so that the signal will represent the temperature of the target rather than the reflected scene. Table 5.1 lists the characteristics of some selected military targets. The following discussion of military target detectability assumes that environmental clutter has been suppressed and that only instrument noise is present.

Figures 5.11 through 5.16 demonstrate the high contrast signal of vehicles and aircraft obtainable with high spatial resolutions. Figure 5.11 shows infrared, visual, and 98 GHz images of the Mojave airport. The millimeter wave image was produced by a helicopter-mounted JPL sensor with a spatial resolution of about 7 m. Measurements of a P-3 aircraft at 90 GHz over both land and water backgrounds appear in Figure 5.12, where the resolution is 3 m in all flight strips except the fifth and sixth strips where it is 10 m. Figure 5.13 shows the signal contrast of the same P-3 at 140 GHz with 3 m resolution. Figure 5.14 presents an image of an aircraft on a pedestal, viewed near 90 GHz with 0.5 m resolution. Note that the bottom of the aircraft appears much warmer than the top because it reflects the relatively hot radiation from the Earth's surface rather than the cold sky reflected by the upper surface. Figures 5.15 and 5.16 show images of automobiles at 90 GHz and 0.5 m resolution. The vertical feature between the two autos in the top two and left images of Figure 5.15 is the signal from a man. The beam-fill contrast temperatures for the aircraft and vehicles in Figures 5.11 - 5.16 is very large; as much as 80 K over water and 120 K over land. The atmospheric loss is  $\alpha = 1/3$  for these images although it typically ranges from 1/3 to 2/3 under cloudy conditions depending upon season and latitude.

To estimate the signal-to-noise ratio, (S/N), for various military targets, a typical value of  $\alpha \approx 1/2$  will be used. This results in an atmospheric factor of  $(1 - \alpha)^2 = 0.25$ . The difference in physical temperature between the target and background,  $\delta T$ , is taken as zero and the temperature of the background as 290 K. The emissivity of the ocean background varies from about 0.55 to 0.68 for calm conditions, depending upon temperature. It is 0.6 at 290 K. Under high sea states the emissivity increases to 0.8 or more. The emissivity of the land background ranges from about 0.55 to 0.93, and an average value of 0.75 will be used for the emissivity of the background. The emissivity of the target is given in Table 5.1. The denominator of Equation (2.14) is the instrument sample noise. It is given as 0.10 and 0.05 K for the 100 and 400 m resolution systems respectively in Table 3.1. These values result in a S/N for a metal target with zero emissivity of 0.027 and 0.0034 times the area of the target in  $\text{m}^2$  for the 100 and 400 m resolution systems respectively. The 400 m baseline system with a 4 m antenna is 8 times less sensitive than the 100 m resolution system using a 17 m antenna.

Under these conditions, and with clutter suppressed, the 100-m resolution baseline system can detect aircraft. For example, the area of a Backfire bomber, a large aircraft, is about  $400 \text{ m}^2$  resulting in a  $\text{S/N} = 11$  for these unresolved targets. To put this in perspective, a probability of threshold detection of 0.5 with a false alarm rate of  $10^{-9}$  requires a S/N of 6. However, for the baseline system with a resolution of 400 m, the S/N is only a little more than one, making a single Backfire bomber practically undetectable. However flights of about 5 or more would be detectable if they were within the 400 m resolution cell. Single fighters with an area of only about  $100 \text{ m}^2$  would not be detectable with either system. Neither would tanks and vehicles with an area of  $\approx 15 \text{ m}^2$ . An area of about  $220 \text{ m}^2$  or greater is required to obtain a S/N of 6 at 100 m resolution. The 400 m resolution system requires a target with an area greater than  $1800 \text{ m}^2$ . Thus single tanks or vehicles are not detectable, but massed groups of 20 or more would be detectable if concentrated within the 100-m resolution cell. Eight times as many would be required for detection with the 400-m resolution system.

### 5.3.2 Ships and Ship Wakes

Metal ships will appear as a cold contrast against the sea. On the other hand, foam from the ship wake or breaking waves has a higher emissivity than the undisturbed sea and will present a warmer contrast. Figure 5.17 shows Micrad images of the aircraft carrier Constellation, through clouds at 34 GHz with a resolution of 10 m. Aircraft carriers as well as other ships are also seen at the docks in Figure 5.2. The area of an aircraft carrier exceeds  $8400 \text{ m}^2$ ; therefore the contrast temperature is more than twenty times larger than a Backfire bomber and can be easily detected even with the 400-m resolution system. The 100-m resolution system will resolve an aircraft carrier and provide contrast temperatures of tens of degrees. Ships as small as an attack boat, with an area of  $260 \text{ m}^2$ , will be detectable at 100-m resolution while something approaching the size of a missile cruiser is required at 400 m resolution for detection.

Figure 5.18 presents a 90 GHz image of a ship and its wake. The brightness temperature of the turbulent wake is as much as 60 K above the sea background of 199 K and temperature contrasts in excess of 10 to 20 K can generally be expected. This wake is 15 km long implying a persistence of at least one-half hour. Contrast temperatures of turbulent wakes longer than about 200 m will be several degrees for the 100-m resolution baseline system and those longer than about 800 m will be nearly a degree for the 400-m system. Thus, S/N ratios of 10 to 20 will result. Ship wakes with lengths of several kilometers will be many samples in extent, which will improve recognition and effective S/N ratio significantly.

The signal from the Kelvin wake of a ship is much weaker than the turbulent wake. Figure 5.19 shows the 90 GHz signal from a modelled Kelvin wake from a destroyer at 15 knots under both calm sea and 12 knot winds. Figure 5.20 also presents the calm sea case in profile. The model represents the wake and sea surfaces as a collection of plane facets with dimensions of five-by-five feet. Although a few individual facets may have brightness temperature contrasts in excess of 20 K, the integrated contrast over the entire wake is only 0.6 and 0.4 K for the calm and rough ocean, respectively. This suggests that, despite the crudity of the model, the Kelvin wake may be detectable with the baseline system. It should be noted that while the turbulent and Kelvin wakes will present positive contrasts above the background, the ship contrast will generally be negative. Therefore, the net contrast in a resolution cell may be reduced and possibly even zero.

### 5.3.3 Infrastructure

Masonry structures, industrial and other buildings, road networks, runways, residential areas, and other cultural features will often have a high emissivity above that of pasture lands or forests and will thus appear hotter than surrounding area. On the other hand, metal roofed buildings, oil tanks, bridges, rail networks, terminals, and other predominantly metal structures will have low emissivities causing them to appear cooler than the surrounding area. Figures 5.1 and 5.2 show the effect of high emissivity targets on land such as buildings and roadways. With the structure of roads, railways and runways extending over many resolution elements, pattern recognition techniques can greatly enhance identification and minimize noise levels. Because

these infrastructure targets are stationary, it is possible to combine a several passes to eliminate weather effects and enhance the interpretation of these structures.

#### 5.3.4 Battlefield Damage Assessment

Smoke appears essentially transparent at millimeter wavelengths, allowing millimeter imaging radiometers, especially the 100 m resolution baseline system, to effectively assess battlefield damage. The location and extent of fires are readily distinguishable through the smoke. Figure 5.21 shows a 34 GHz Micrad image that clearly delineates the hot burning region of forest fire which is totally obscured in the visible photo shown below it. Because of the much higher temperatures, smaller burning regions can be detected. For example, an intense fire will have a temperature of as much as 1200 K above the background and, for an atmospheric loss of  $\alpha \approx 0.2$ , a burning region of only  $16 \text{ m}^2$  would produce a S/N of 6 with the 100 m resolution system. The 400 m resolution system would require an area of  $128 \text{ m}^2$ , about 11 m on a side.

**TABLE 5.1**  
**Characteristics of Military Targets at Millimeter Wavelengths**

Target	Area (M <sup>2</sup> )	Emissivity	Temperature (K)
Aircraft Carrier	8400-13700	0	290
Battleship	9000	0	290
Missile Cruiser	3400	0	290
Destroyer	1300	0	290
Attack Boat	260	0	290
PT Boat	185	0	290
Patrol Boat	300	0	290
Ship Wake	Up to 3000 +	0.9	290
Ship Atmos. Wake	Beam fill	0.7 - 0.9	283
B-52	800	0	290
Backfire	400	0	290
F-117A Fighter	108	0	290
F-15E Fighter	83	0	290
Tank	15	0	290
Car	12	0	290
Missile	10	0	290
Mines	1	0	290
Troop Concentration	100/company	1.0	290
Building	2500	0.87	290
Airport/runways	50000	0.9	290
Fires/Battlefield Damage Assessment	10000	> 0.9	700

## PORtSMOUTH, VA

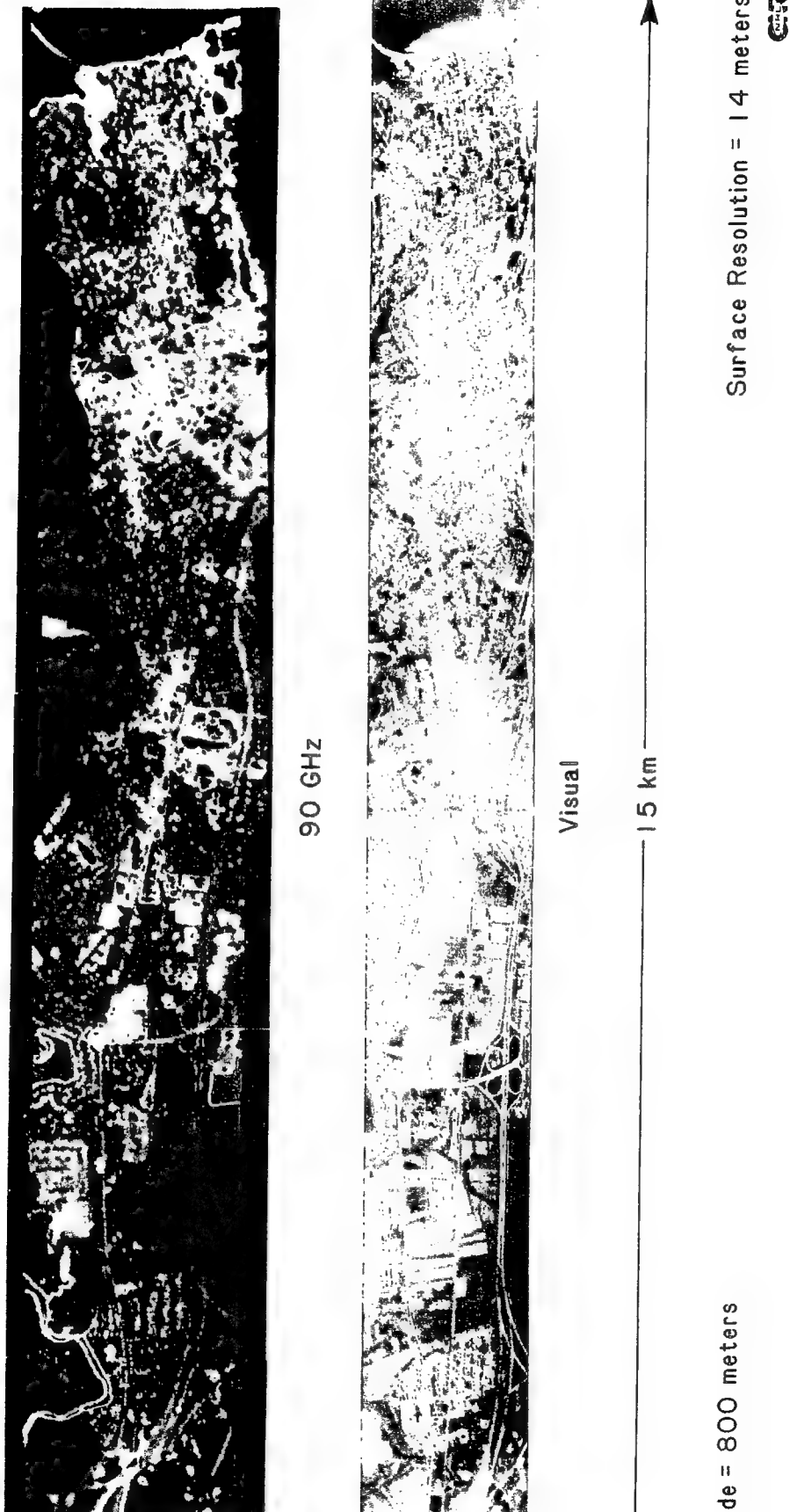


Figure 5.1 90 GH : Imagery of Portsmouth, Virginia.

NORFOLK, VA



90 GHz



Visual

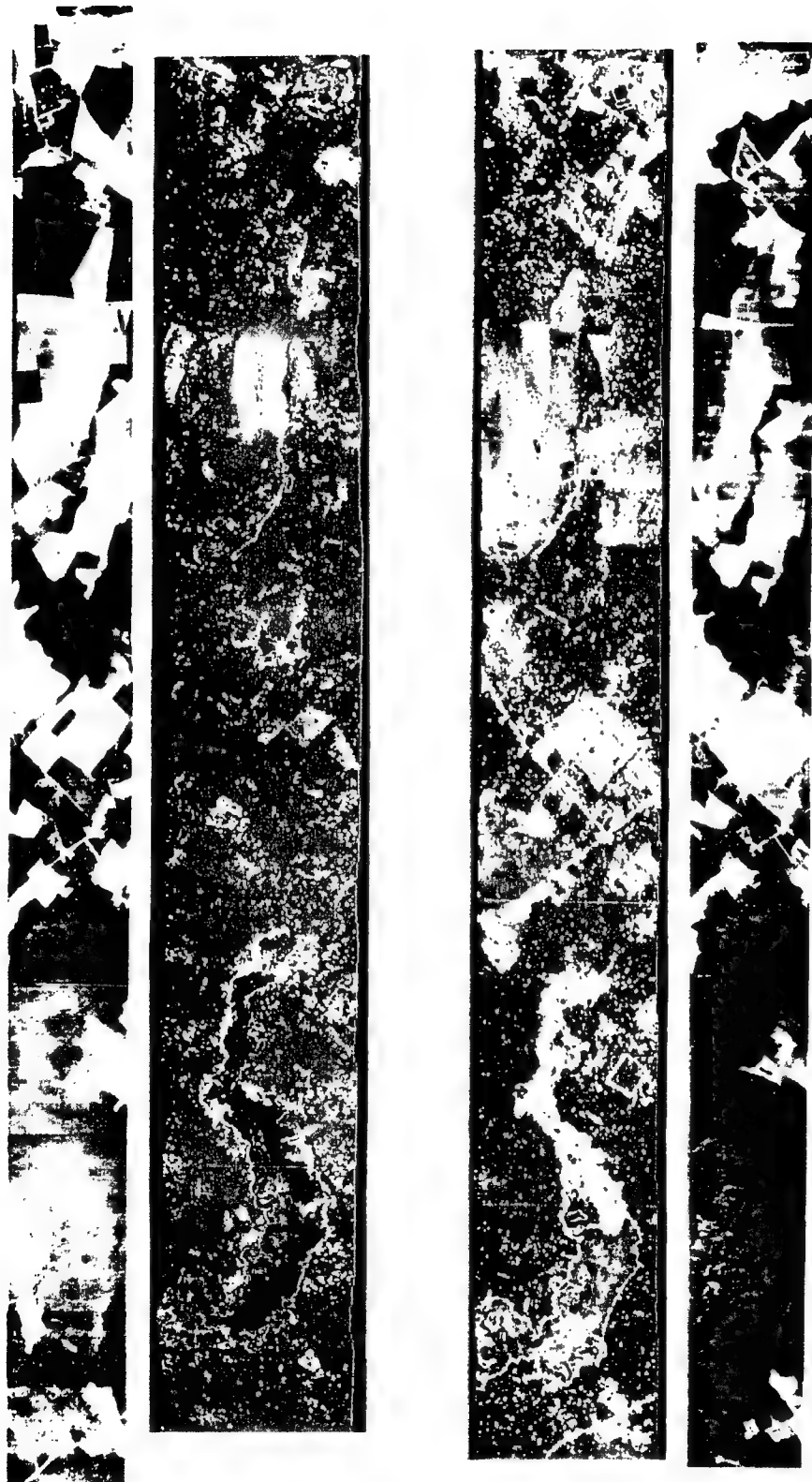
Altitude = 800 meters

6.7 km

Surface Resolution = 14 meters

Figure 5.2 90 GHz Imagery of the Docks at Norfolk, Virginia.

APRIL 1980



JANUARY 1981

3 km

Altitude = 870 meters

Surface Resolution = 15 Meters

Figure 5.3 90 GHz Imagery of Virginia Farmland in January and April.

FARMLAND EASTERN VIRGINIA

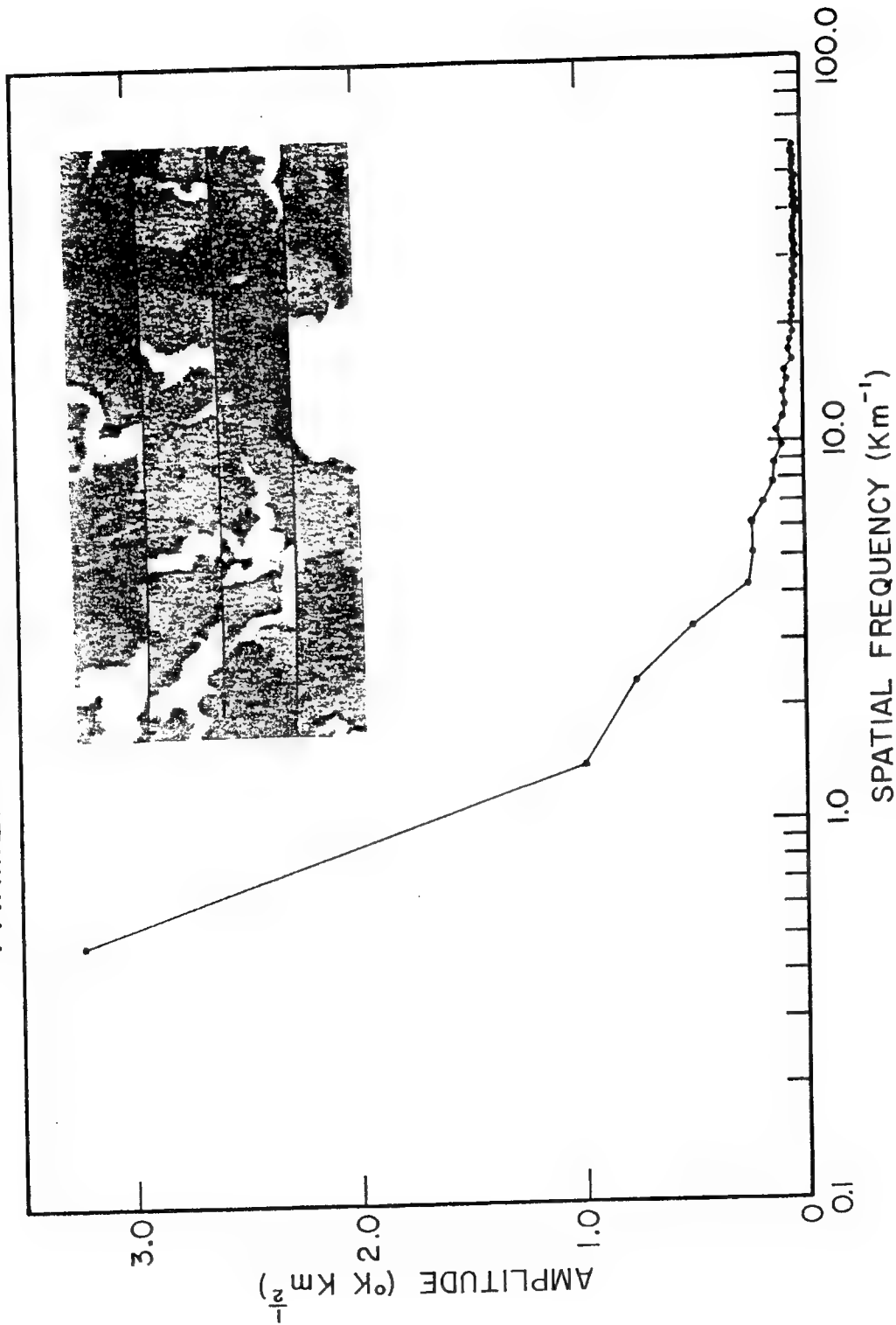


Figure 5.4 Spatial Clutter Spectrum of Farmland at 90 GHz.

SEA ICE GREENLAND SEA

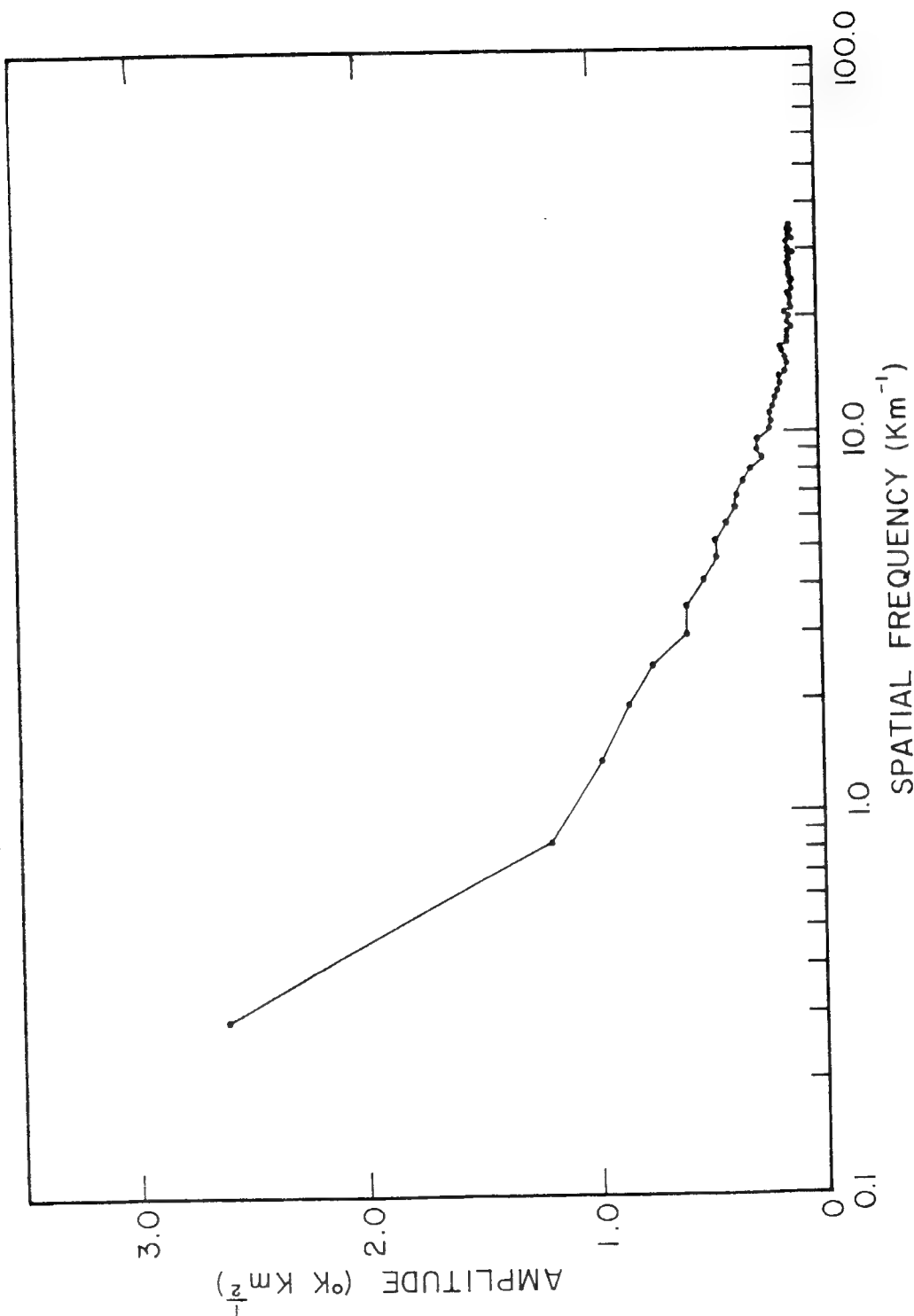


Figure 5.5 Spatial Clutter Spectrum of Sea Ice at 90 GHz.

DOCKS NORFOLK, VIRGINIA

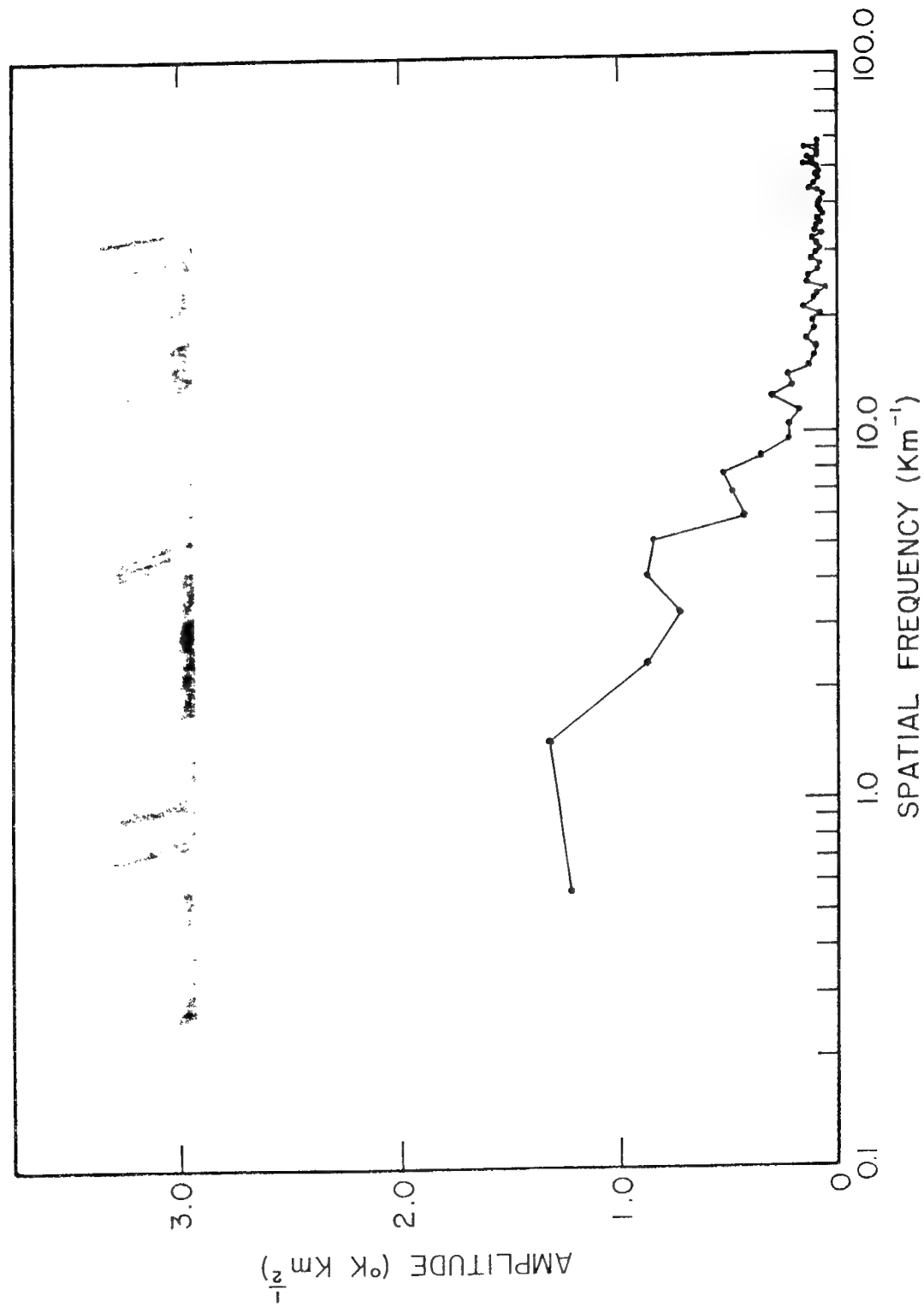


Figure 5.6 Spatial Clutter Spectrum of Dock Area at 90 GHz.

HIGH RESOLUTION RADIOMETRY  
DATA SERIES

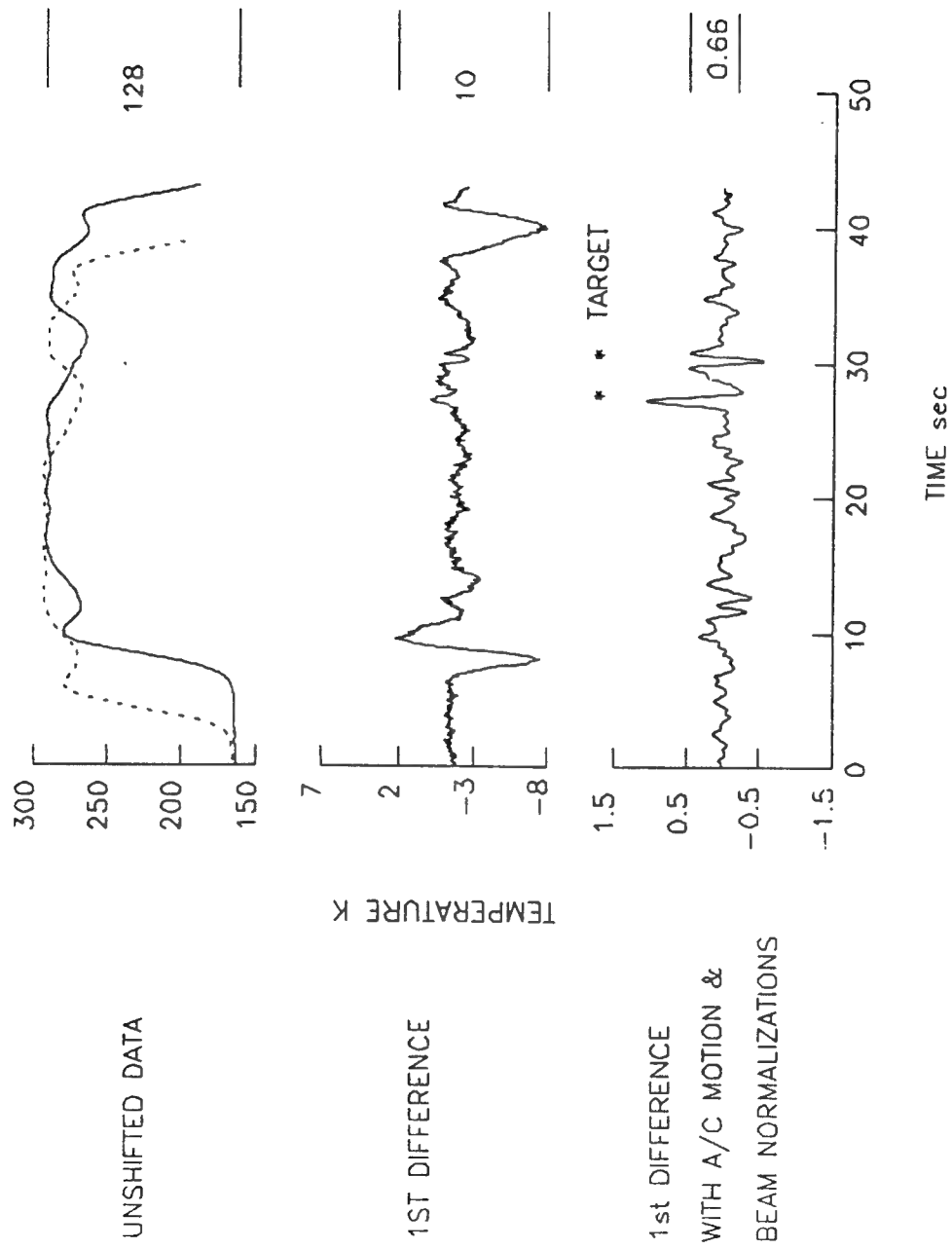


Figure 5.7 Clutter Suppression Using Beam Differencing.

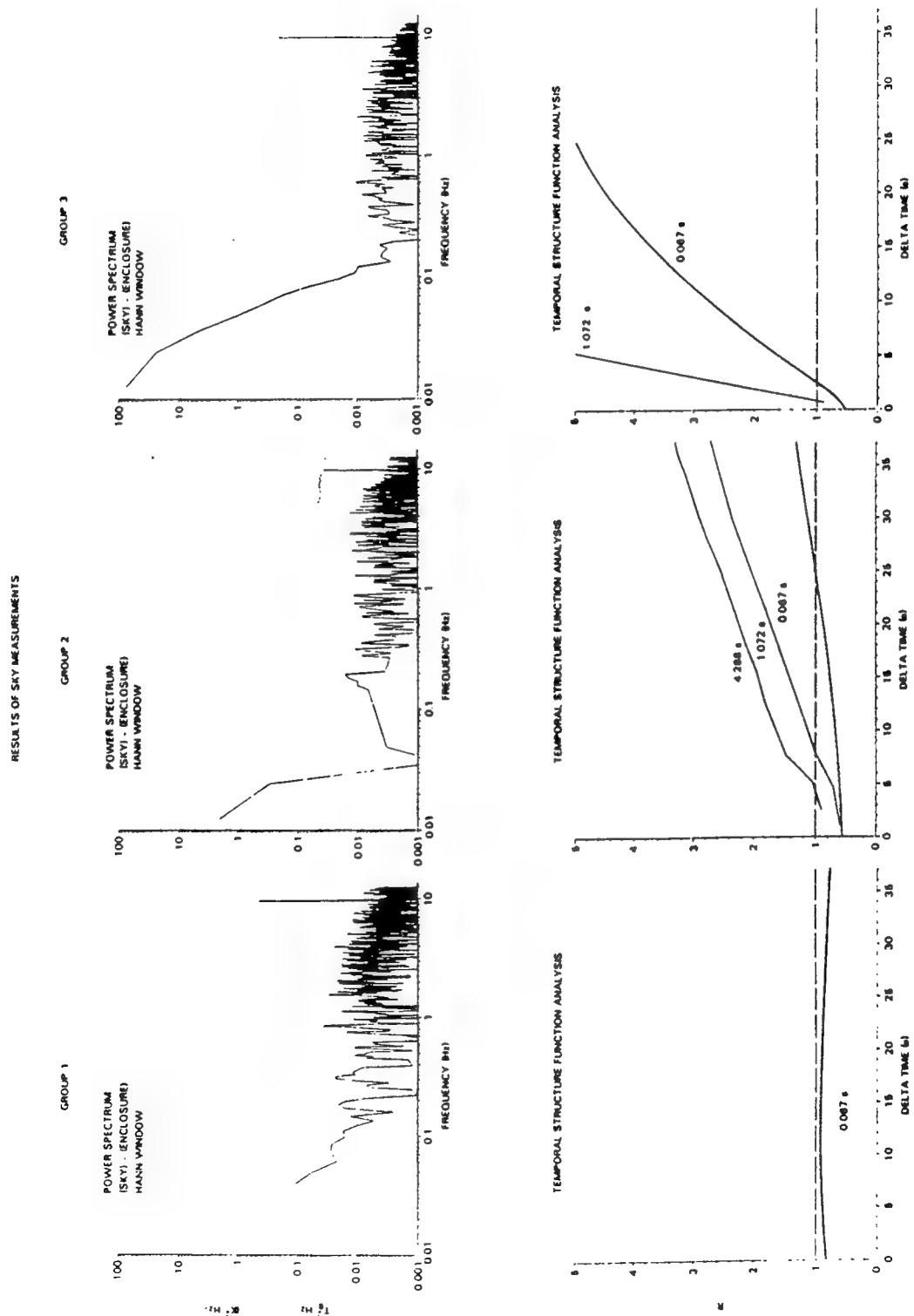


Figure 5.8 Atmospheric Clutter Analysis for Three Sets of Atmospheric Conditions.

STANDARD DEVIATION OF TEMPERATURE DIFFERENCES

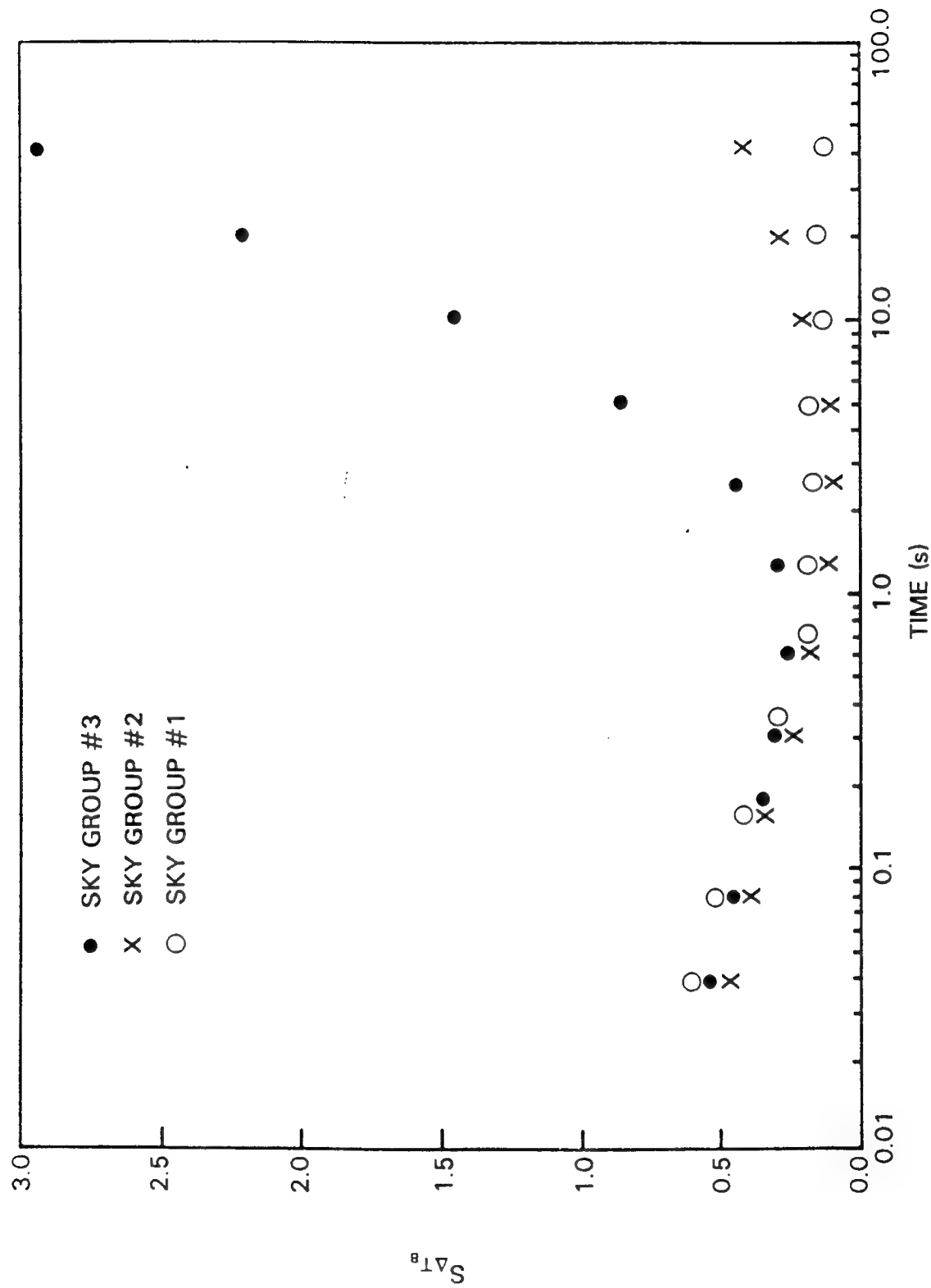


Figure 5.9 Atmospheric Clutter Noise Increase With Increased Integration Time.

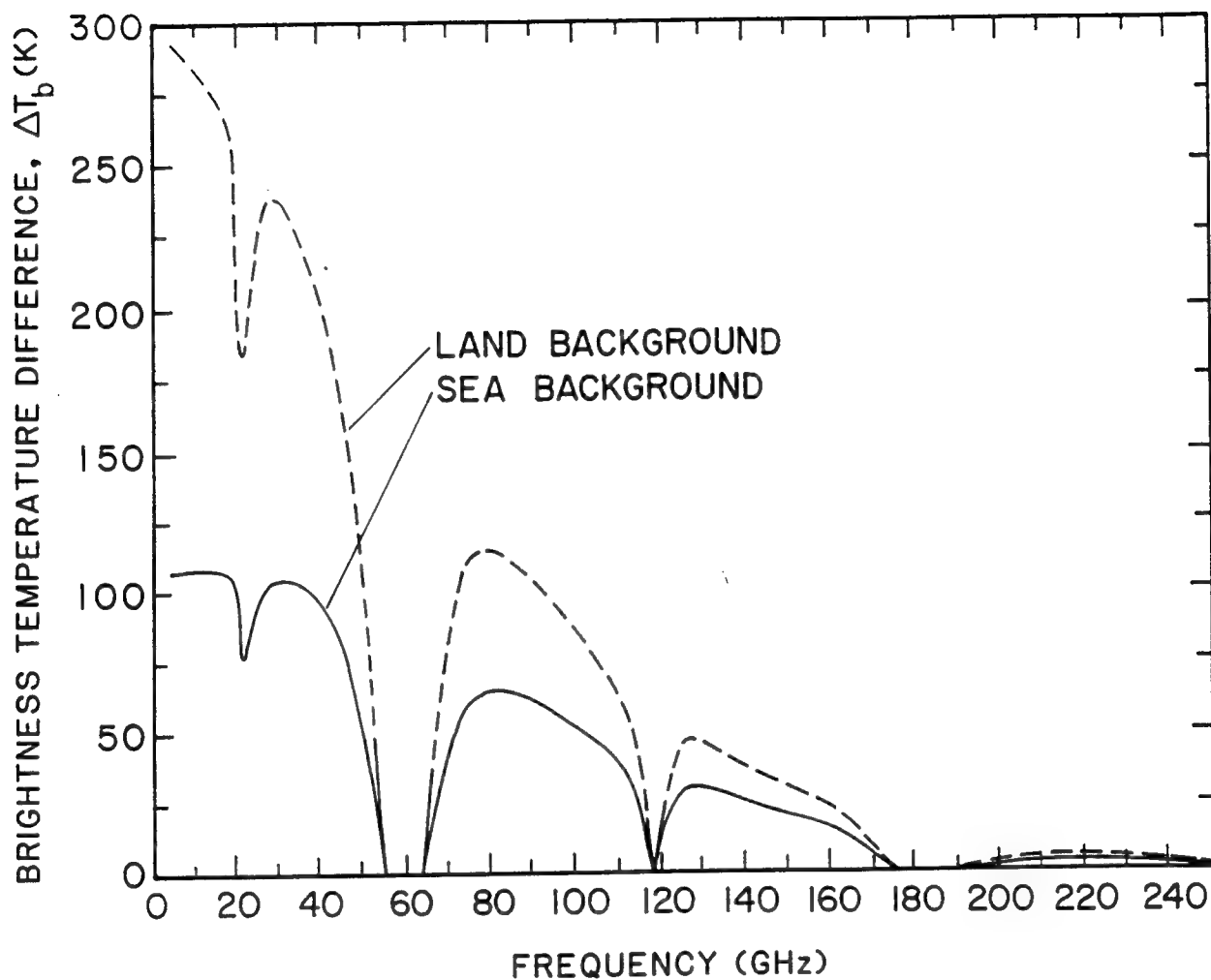


Figure 5.10 Apparent brightness temperature differences under good weather conditions between a reflecting target and a land (dashed line) or a sea (solid line) background at normal incidence [Weiler et al., 1986].

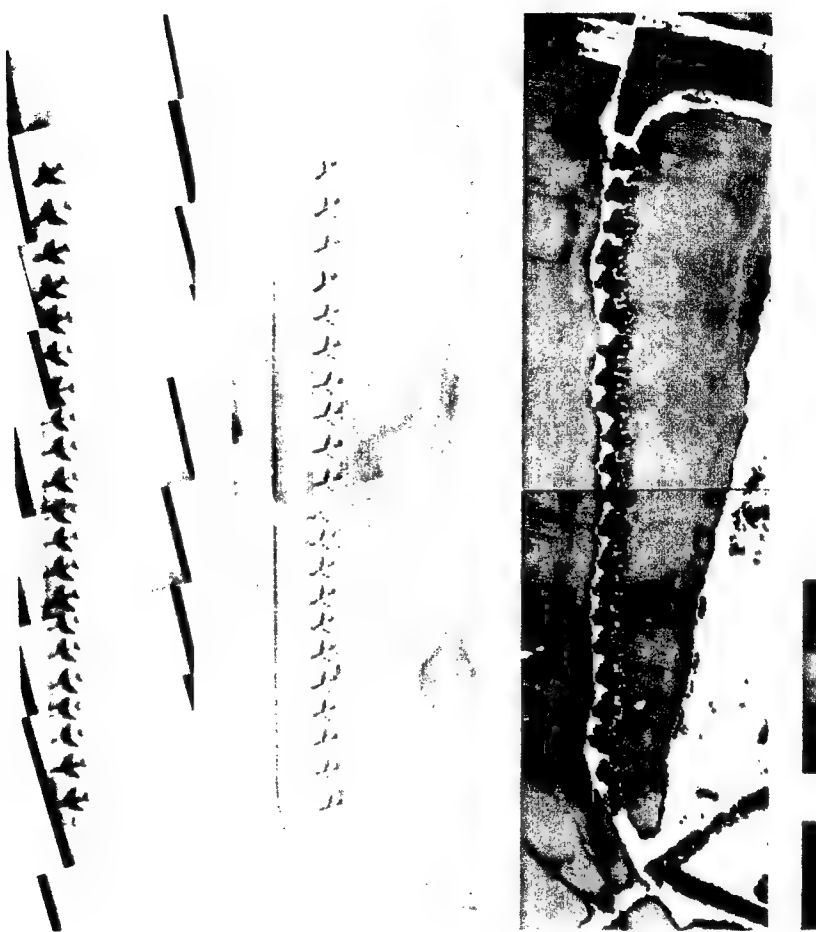


Figure 5.11 Visual (left), infrared (center) and millimeter-wave images of the Mojave Airport [Wilson and Ibbott, 1987].



Figure 5.12 90 GHz Imagery of an NRL P3-A Aircraft Over Land and Sea Backgrounds.

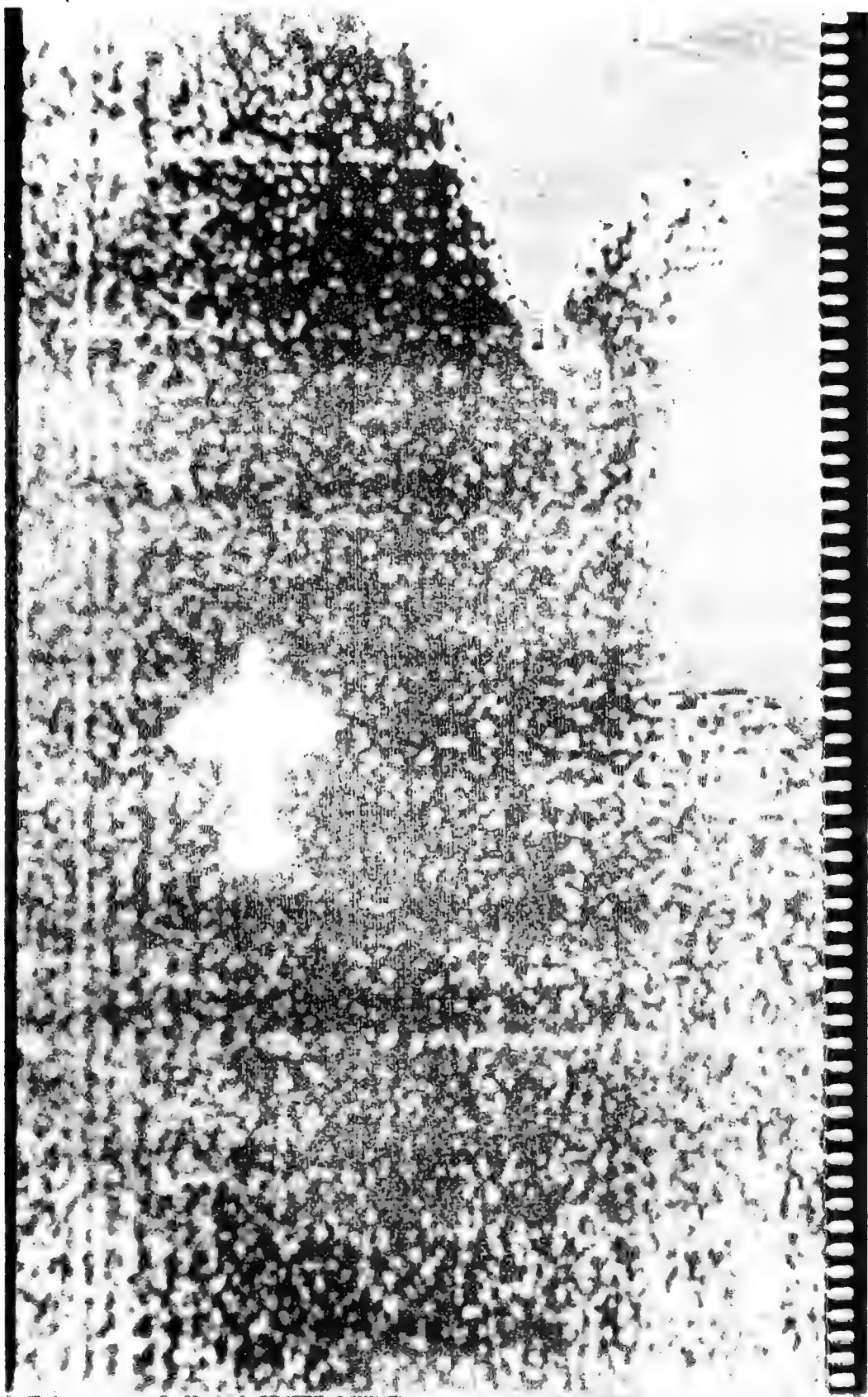
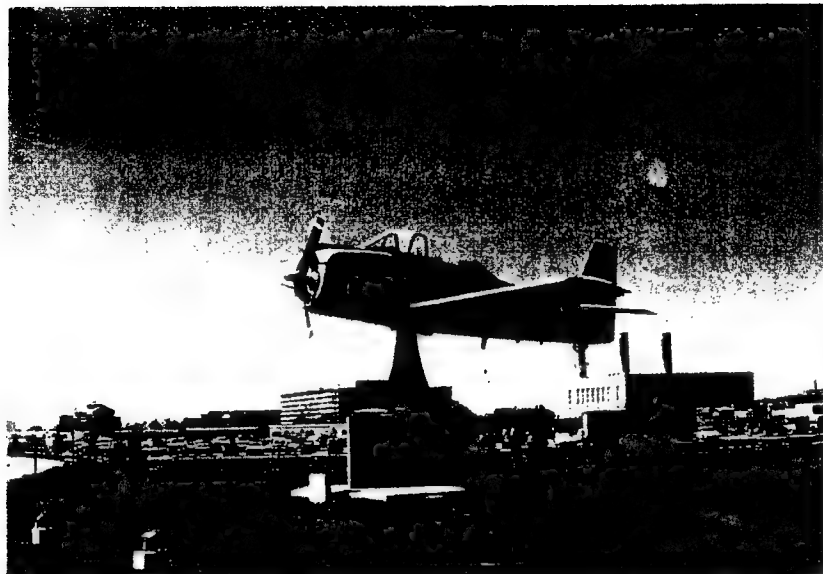


Figure 5.13 140 GHz Imagery of an NRL P3-A Aircraft Over Water



## 90 GHz RADIOMETRIC IMAGE



Figure 5.14 Very High Resolution 90 GHz Imagery of a Pedestal Mounted Aircraft.

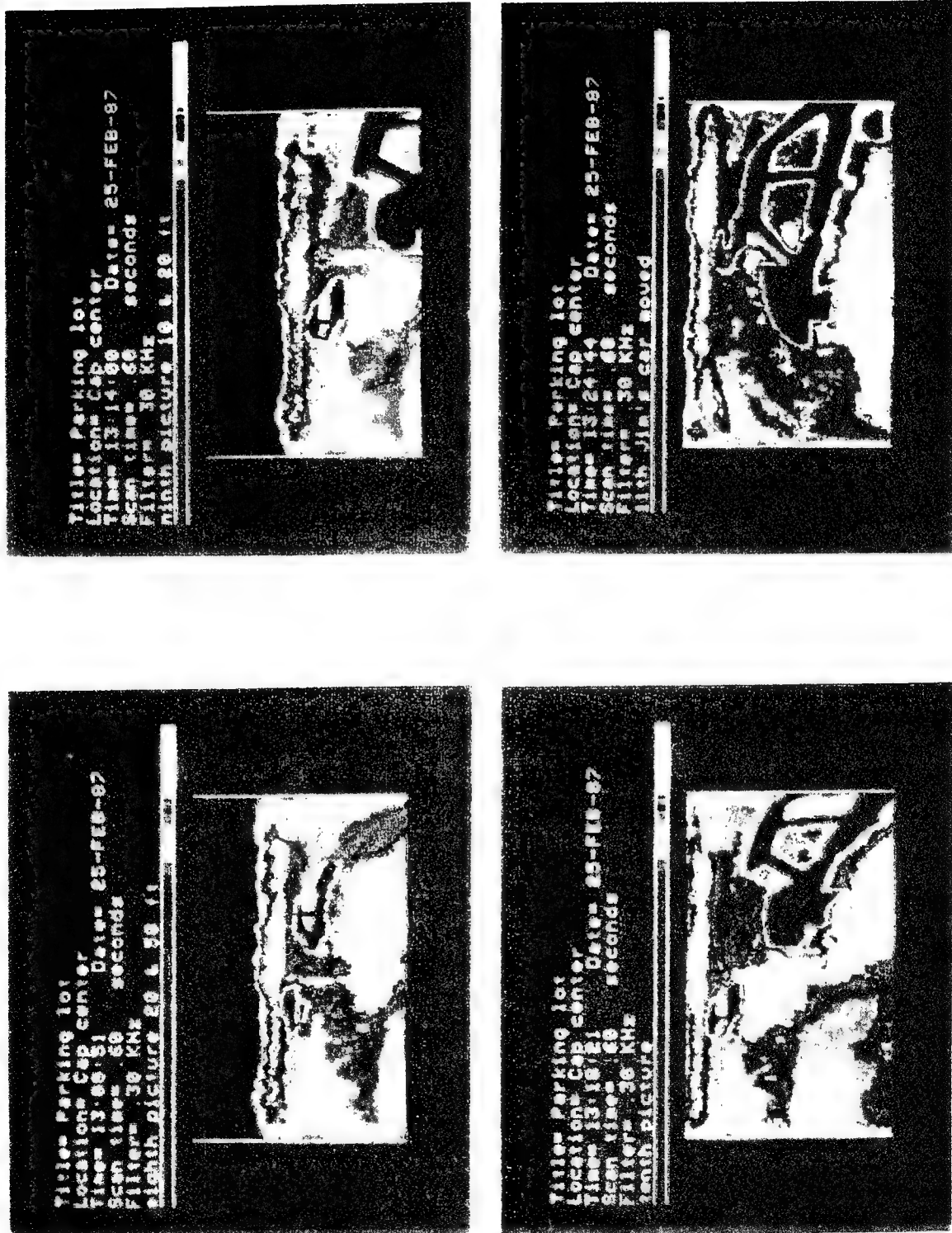
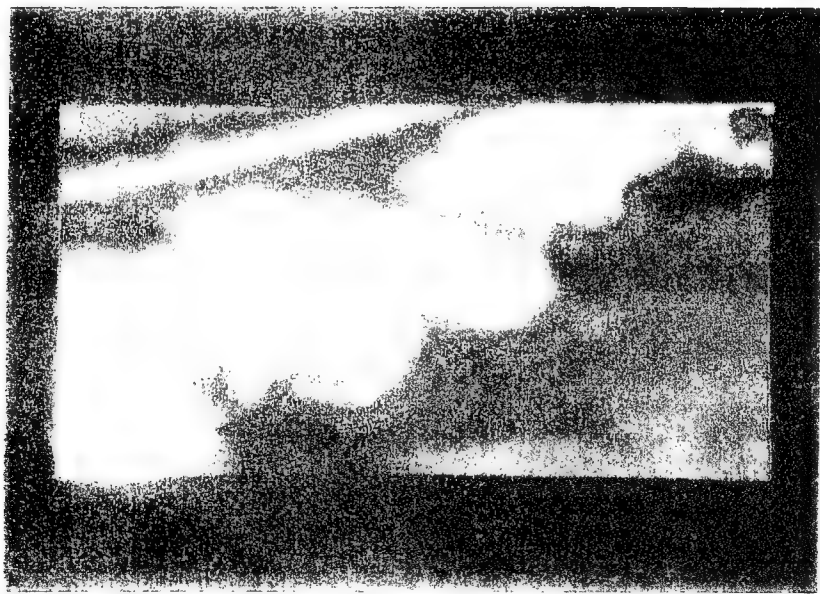
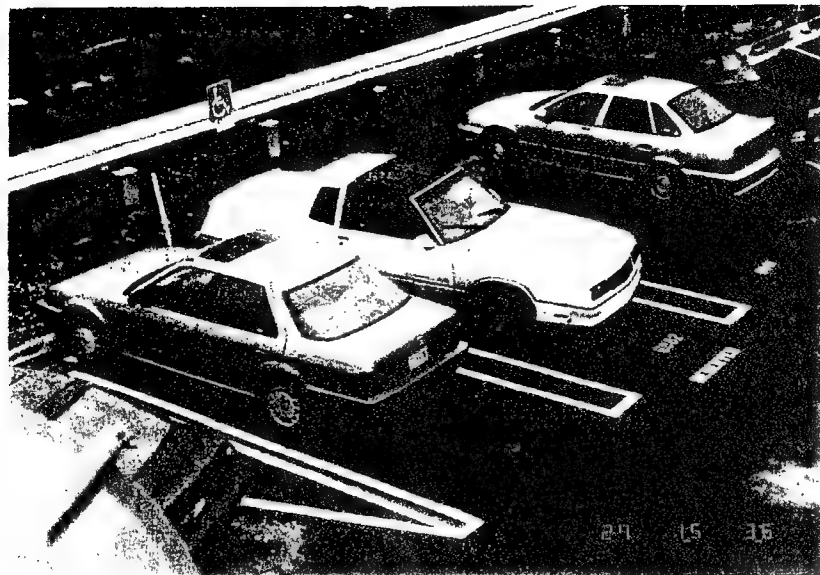


Figure 5.15 Very High Resolution 90 GHz of Automobiles and Man.

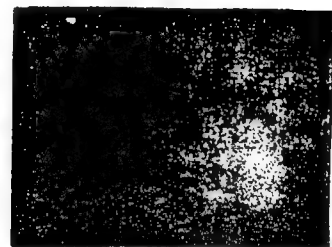


90 GHz RADIOMETRIC IMAGE

 CR

Figure 5.16 Very High Resolution Imagery of a Parking L t.

CARRIER CONSTELLATION THRU CLOUDS



AERIAL PHOTO

Figure 5.17 34 GHz Imagery of the Aircraft Carrier CONSTELLATION.

**WAKES**



90 GHz



Visual

15 Km

Altitude = 340 meters

Surface Resolution = 16 meters

CCR

Figure 5.18 90 GHz Imagery of the Turbulent Wake From a Ship.

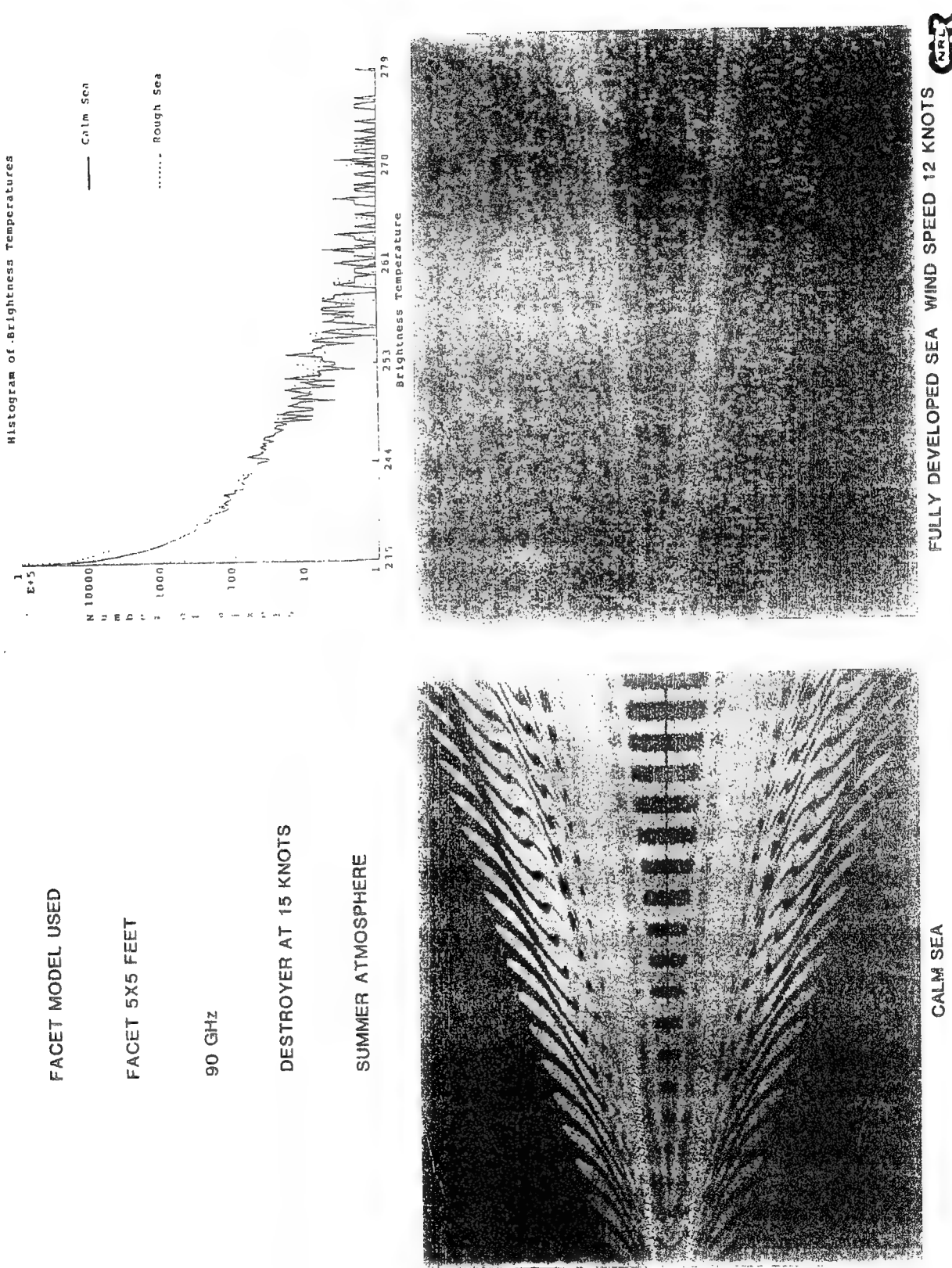
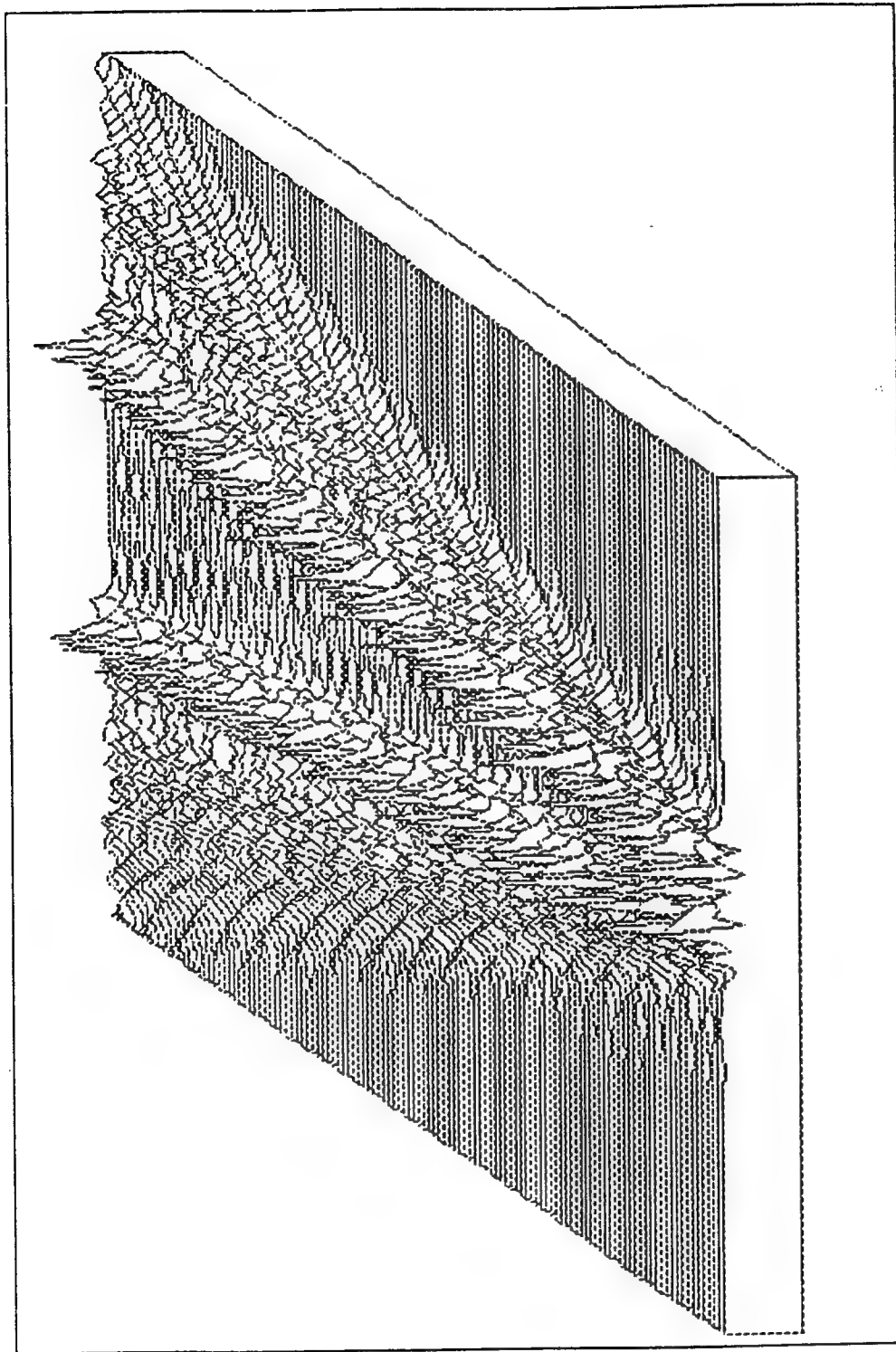


Figure 5.19 Modeled 90 GHz Imagery of Kelvin Wake From a Destroyer.



Simulation of Ship Kelvin Wake at 90 Ghz

Figure 5.20 Silhouette Representation of Modeled 90 GHz Kelvin Wake From a Destroyer.

SANTA YNEZ MOUNTAINS FOREST FIRE  
MICROWAVE RADIOMETER MAP

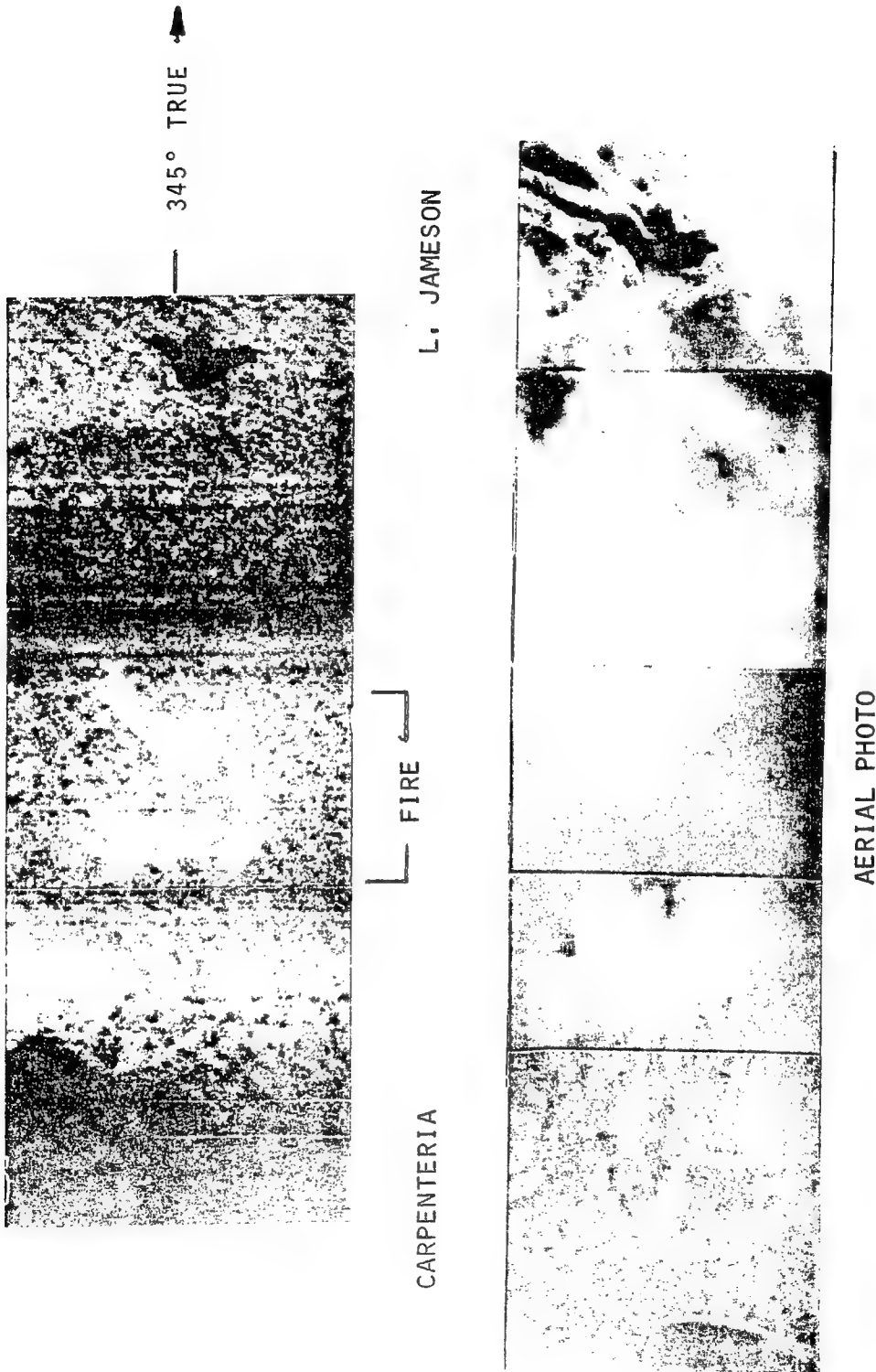


Figure 5.21 34 GHz Imagery of a Forest Fire.

## 6.0 SUMMARY

A series of SSM/I multichannel microwave radiometric systems aboard the Defense Meteorological Satellite Program (DMSP) have demonstrated the value of millimeter wave radiometry from space for environmental measurements. The SSM/I operates at frequencies between 19 and 85 GHz, with surface resolutions ranging from 70 to 13 km. It obtains synoptic maps of critical atmospheric, oceanographic, and land parameters on a global scale. In particular it quantifies the presence of water vapor, cloud water, and precipitation as well as locating and defining the structure of squall lines, hurricanes, weather fronts, clouds, and convective regions. It measures marine wind speed, locates the sea ice edge and determines sea ice concentration and age. It is able to identify fourteen different land surface types including snow cover, vegetation cover, arable soil, desert, and various stages of soil moisture.

The baseline system, described in this report, operating over 1.4 to 140 GHz with a surface resolution of 100 - 400 m, would define similar environmental structure but with a hundredfold increase in resolution. It could provide detailed information on water/land boundaries, wetlands, drainage patterns, cultivation, vegetation, volcanoes, storm damage and snow cover. It would allow location of polynas, leads, and sea ice concentration for greatly improved navigability through sea ice. It would be able to accurately locate the eye and structure of hurricanes, convective regions, and storms. It would be able to quantify oil spills, track their motion, and allow more efficient and effective containment and clean up. It would be able to locate the burning regions and extent of forest fires through the smoke to assist fire fighting efforts.

## 7.0 REFERENCES

Alishouse, J.C., Snyder, S.A., Vongsathorn, J., and Ferraro, R.R. (1990), Determination of oceanic total precipitable water from the SSM/I, *IEEE Transaction on Geoscience and Remote Sensing*, GE-28(5):811-816.

Bauer, D.G., McGee, R.A., Know, J.E. and Wallace, H.B. (1977), Ballistic Research Laboratories, Memo #538.

Bjerknes, J. (1969), Atmospheric teleconnections from the equatorial Pacific, *Mon. Wea. Rev.*, 97, 163-172.

Blume, H-J.C., Kendall, B.M., and Fedors, J.C. (1978), Measurement of ocean temperature and salinity via microwave radiometry. *Boundary Layer Meteorology*, 13:295-308.

Blume, H-J.C. and Kendall, B.M. (1982), Passive microwave remote measurements of temperature and salinity of coastal zones. *IEEE Transactions on Geoscience and Remote Sensing*, GE-20(3):394-404.

Brunfeldt, D.R. and Ulaby, F.W. (1984), Measured microwave emission and scattering in vegetation canopies, *IEEE Transactions on Geoscience and Remote Sensing*, GE-22(6):520-524.

Cavalieri, D.J., Gloersen, P. and Campbell, W.J. (1984), Determination of sea ice parameters with the Nimbus-7 SMMR, *J. Geophysical Research*, 89, 5355-5369.

Chahine, M.T. (1983), *Manual of Remote Sensing*, vol. 1, Chap. 5, American Society of Photogrammetry, Falls Church, VA.

Cogdell, J.R. and Davis, J.H. (1973), Astigmatism in reflector antennas. *IEE Transactions on Antennas and Propagation*, AP21, pp 565-567.

Falcone, V.J. et al. (1993), *SSM/T-2 Calibration and Validation*, PL-TR-92-2293, Environmental Research Papers, no. 1111.

Gaddis, L.R., Mouginis-Mark, P.J., Singer, R.B., and Kaupp, V. (1989), Geologic analyses of the Shuttle Imaging Radar (SIR-B) data of Kiluea Volcano, Hawaii. *Geologic Society of America Bulletin*, 101, 317.

Gaiser, P.W. (1993), The Development of a Second Generation Electrically Scanned Thinned Array Radiometer. Ph.D. dissertation, University of Massachusetts.

Goodberlet, M.A., Swift, C.T. and Wilkerson, J.C., (1989), Remote sensing of ocean surface winds with the Special Sensor Microwave/Imager. *J. Geophysical Research*, 94:14,547-14,555.

Griffis, A.J. (1993), Earth Remote Sensing with an Electrically Scanned Thinned Array Radiometer. Ph.D. dissertation, University of Massachusetts.

Hannan, P.W. (1961), Microwave antennas Driver from the Cassegrain telescope, *IRE Transactions on Antennas and Propagation*, AP9, pp 140-153.

Hofer, R., and Matzler, C. (1980), Investigations on snow parameters by radiometry in the 3-to-60 mm wavelength region, *J. Geophysical Research*, 85, pp.453-460.

Hollinger, J.P., Troy, B.E., and Hartman, M.F. (1984), All-weather millimeter wave imagery in the marginal ice zone, *Radio Science*, 19, 862-870.

Horel, J.D., and Wallace, J.M. (1981), Planetary scale atmospheric phenomena associated with the southern oscillation, *Mon. Wea. Rev.*, 109, 813-829.

Houze, R. A., Jr. (1982), Cloud clusters and large-scale vertical motions in the tropics, *J. Meteor. Soc. Japan*, 60, 396-410.

Jorgensen, D. P. (1984), Mesoscale and convective scale characteristics of mature hurricanes. Part I. General observations of research aircraft, *J. Atmos. Sci.*, 41, 1268-1285.

Klein, L.A. and Swift, C.T. (1977), An improved model for the dielectric constant of sea water at microwave frequencies. *IEEE Transactions on Antennas and Propagation*, AP-25(1):104-111.

Kraus, J.D., (1966), *Radio Astronomy*, McGraw-Hill, Inc.

Lagerloef, G.S., Swift, C.T., LeVine, D.M. and Griffis, A.J. (1992), Remote sensing of sea surface salinity: Airborne and satellite concepts. AGU-Oceans Poster 21A-19 (New Orleans).

Lau, K. M., and Chan, P. H. (1985), Aspects of the 40-50 day oscillations during the northern winter as inferred from outgoing longwave radiation, *Mon. Wea. Rev.*, 113, 1889-1909.

Lau, K. M., and Chan, P. H. (1986), The 40-50 day oscillation and the El Nino-Southern Oscillation: A new perspective, *Bull. Amer. Meteor. Soc.*, 67, 533-534.

Lau, K. M., and Chan, P.H. (1987), Intraseasonal and interannual variations of tropical convection: A possible link between the 40-day mode and ENSO?, *J. Atmos. Sci.*

LeVine, D.M. (1990), The sensitivity of synthetic aperture radiometers for remote sensing applications from space, *Radio Science*, 25(4), pp 441-453.

LeVine, D.M., Kao, M., Tanner, A.B., Swift, C.T., and Griffis, A.J. (1990), Initial results in the development of a synthetic aperture radiometer. *IEEE Transactions on Geoscience and Remote Sensing*, GE-28(4):614-619.

Lorenc, A. C. (1984), The evolution of planetary scale 200 mb divergent flow during the FGGE year, *Quart. J. Roy. Meteor. Soc.*, 110, 427-441.

Love, A.W. (1978), *Reflector Antennas*, IEEE Press.

Milman, A. and Wilheit, T. (1983), Sea surface temperatures from the Nimbus-7 Scanning Multichannel Microwave Radiometer, in *Satellite Derived Sea Surface Temperature: Workshop I*, JPL Pub. No. 83-84, NASA Jet Propulsion Lab., Pasadena, CA.

Murphy, R. (1987), Report of High-Resolution Multifrequency Microwave Radiometer Instrument (HMMR) Panel, vol. IIe: Earth Observing System Report. NASA Tech. Rep., NASA, Washington, D.C.

Neale, C.M.U., McFarland, M.J., and Chang, K.J. (1990), Land-surface-type classification using brightness temperatures from the Special Sensor Microwave/Imager. *IEEE Transactions on Geoscience and Remote Sensing*, GE-28(5):906-914.

Olson, W.S. (1987), Estimation of rainfall rates in tropical cyclones by passive microwave radiometry. Ph.D. dissertation. University of Wisconsin.

Rasmusson, E. M. (1985), El Nino and Variations in Climate, *Amer. Scientist*, 73, 168-178.

Riehl, H., and Simpson, J. (1979), The heat balance of the equatorial trough zone revisited, *Contributions to Atmos. Phys.*, 52, 287-304.

Rosenkranz, P.Q. (1975), Shape of the 5 mm Oxygen band in the atmosphere, *IEEE Trans. Ant. Prop.*, AP-23, pp 498-506.

Schanda, E., Maetzler, C., and Koenzi, K. (1983), Microwave remote sensing of snow cover, *Int. J. Remote Sensing*, vol. 4, 149-158.

Schmugge, T.J. (1983), Remote sensing of soil moisture: recent advances. *IEEE Transactions on Geoscience and Remote Sensing*, GE-21(3):336-344.

Schroeder, D.J. (1987), *Astronomical Optics*, Academic Press, Inc.

Simpson, R. H., and Riehl, H. (1981), *The Hurricane and Its Impact*, Louisiana State University Press. Baton Rouge and London, 398 pp.

Simpson, J., ed. (1988), TRMM - A Satellite Mission to Measure Tropical Rainfall: Report of the Science Steering Group. NASA Goddard Space Flight Center.

Smith, P.M. (1988), The emission of sea foam at 19 and 37 GHz. *IEEE Transactions on Geoscience and Remote Sensing*, GE-26(5):541-547.

Swift, C.T. and McIntosh, R.E. (1983), Considerations for microwave remote sensing of ocean-surface salinity. *IEEE Transactions on Geoscience and Remote Sensing*, GE-21(4):480-491.

Tanner, A . (1992), Preliminary ESTAR design concept, JPL.

Thomann, G.C. (1976), Experimental results of the remote sensing of the sea-surface salinity at 21 cm wavelength. *IEEE Transactions on Geoscience Electronics*, GE-14(3):198-214.

Troy, B.E., Hollinger, J.P., Lerner, R.M. and Wisler, M.M. (1981), Measurement of the microwave properties of sea ice at 90 GHz and lower frequencies, *J. Geophysical Research*, 86, 4283-4289.

Tsang, L., Kong, J.A., Njoku, E., Staelin, D.H. and Waters. J.W. (1977), Theory of microwave thermal emission from a layer of cloud or rain, *IEEE Transactions on Antennas and Propagation*, AP-25:650-657.

Ulaby, F.W., Razani, M., and Dobson, M.C., (1983), Effects of vegetation cover on the microwave radiometric sensitivity to soil moisture, *IEEE Transactions on Geoscience and Remote Sensing*, GE-21, pp. 51-61.

Ulaby, F.W., Moore, R.K., and Fung, A.K. (1986), *Microwave Remote Sensing, Active and Passive, Volume III: From Theory to Applications*, Norwood, MA: Artech House, Inc.

Ulaby, F.W. and Stiles, W.H. (1980), The active and passive microwave response to snow parameters, part II: Water equivalent of dry snow, *J. Geophysical Research*, 85, pp.1045-1049.

Water, J.W. (1976), Absorption and emission of mi crowave radiation by atmospheric gases, in *Methods of Experimental Physics*, M. L. Meeks, Ed., 12, Part B, Radio Astronomy, Academic Press, Section 2.3.

Wang, J.R., O'Neill, P.E., Jackson, T.J., and Engman, E.T. (1983), Multifrequency measurements of the effects of soil moisture, soil texture, and surface roughness, *IEEE Transactions on Geoscience and Remote Sensing*, GE-21, pp. 44-51.

Wang, J.R., Shiue, J.C., Schmugge, T.J., and Engman, E.T. (1990), The L-band PBMR measurements of soil moisture in FIFE, *IEEE Transactions on Geoscience and Remote Sensing*, GE-28(5):906-914.

Webster, P. J. (1981), Mechanisms determining the atmospheric response to large scale sea surface temperature anomalies, *J. Atmos. Sci.*, 38, 554-571.

Webster, P. J. (1982), Seasonality of atmospheric response to sea surface temperature anomalies, *J. Atmos. Sci.*, 39, 29-40.

Weickmann, K. M., Lussky, G. R., and Kutzbach, J.E. (1985), Intraseasonal (30-60 Day) fluctuations of outgoing longwave radiation and 250 mb streamfunction during northern winter, *Mon. Wea. Rev.* 113, 941-961.

Weiler, K.W., Dennison, B.K., Bevilaqua, R.M., Spencer, J.H., Johnston, K.J., and Andrews, G.A. (1986), The Space Station Microwave Facility, NRL Memorandum 5821, Washington, DC.

Weinmann, J.A. and Guetter, P.J. (1977), Determination of rainfall distribution from microwave radiation measured by the Nimbus-6 ESMR, *J. Appl. Meteorology*, 16, 437-442.

Wentz, F.J. (1992), Measurement of oceanic wind vector using satellite microwave radiometers, *IEEE Transactions on Geoscience and Remote Sensing*, GE-30(5): 960-972.

Wilheit, T.T., Nordberg, W., Blinn, J., Campbell, W.J. and Edgerton, A. (1972), Aircraft measurements of microwave emission for Arctic sea ice, *Remote Sensing of the Environment*, 2, 129-139.

Wilheit, T.T. et al. (1982), Microwave radiometric observations near 19.35, 35, 92, 183 GHz of precipitation in tropical storm Cora. *J. Appl. Meteorology*, 21, 1137-1145.

Wilheit, T.T., Chang, A.T.C., Gloersen, P., and Milman, A.S. (1980), Tests of retrievals of ocean surface parameters from the Scanning Multichannel Microwave Radiometer (SMMR), COSPAR-SCOR-IUCRM Symposium on Oceanography from Space, Venice, Italy, May.

Wilheit, T.T., Greaves, J., Gatlin, J., Han, D., Krupp, B.M., Milman, A.S., and Chang, E. (1984), Retrieval of ocean surface parameters from the Scanning Multichannel Microwave Radiometer (SMMR) on the Nimbus-7 Satellite, *IEEE Transactions on Geoscience and Remote Sensing*, GE-22:133-142.

Wilson, W.J. and Ibbot, A.C. (1987), Millimeter-Wave Imaging Sensor Data Evaluation, JPL Publication 87-16, Jet Propulsion Laboratory, Pasadena, CA.